The Dissertation Committee for Shaoqing Zhang Certifies that this is the approved version of the following Dissertation:

NANOSCALE INVESTIGATION OF SILK PROTEINS USING NEAR-FIELD OPTICS

Committee:

Hu Tao, Supervisor

Wei Li

Donglei Fan

Keji Lai

Chong Xie

NANOSCALE INVESTIGATION OF SILK PROTEINS USING NEAR-FIELD OPTICS

by

Shaoqing Zhang

Dissertation

Presented to the Faculty of the Graduate School of

The University of Texas at Austin

in Partial Fulfillment

of the Requirements

for the Degree of

Doctor of Philosophy

The University of Texas at Austin

May 2018

Dedication

I dedicate this dissertation to my parents, Qiufang and Fengyi, who has been constant support and inspiration to me throughout my entire life and the years of my graduate study in particular. I am truly thankful for their unconditional love that help me get through the toughest moments of my academic career. Their open-mindedness really grants me freedom and courage to pursue what I aspire to achieve.

Acknowledgements

I would like to express my gratitude to my advisor, Dr. Tiger. H. Tao, who encouraged and guided me onto this project. As his first student, I got the chance to learn the establishment of a laboratory from ground up and work closely with collaborators to build collaborations. I truly enjoy working in a creative and multidisciplinary research environment that stems from Dr. Tao's vision of the research and focus on the scientific innovations.

I would like to acknowledge the valuable input and help of Dr. Mengkun Liu, whose expertise on the near-field characterization and the material properties inspires me many times on the project.

I would also like to acknowledge the helpful suggestions and insightful discussions from my committee members: Dr. Wei Li, Dr. Donglei Fan, Dr. Keji Lai, Dr. Chong Xie.

Abstract

NANOSCALE INVESTIGATION OF SILK PROTEINS USING NEAR-FIELD OPTICS

Shaoqing Zhang, Ph.D.

The University of Texas at Austin, 2018

Supervisor: Hu Tao

Recent developments in nanotechnology have led to renewed interest and breakthroughs in structural biopolymers, specifically silk protein, as functional materials. The exceptional mechanical properties and the bio-compatibility of silk has enabled wide range of applications from biomedical devices, optics, electronics, to transient implants. Understanding the mechanisms that underpin the β-sheet formation and deformation as well as the formulation of strategies to control inter- and intramolecular bonds within silk protein matrices is paramount for the control of protein structures and the improvement of material properties. However, conventional imaging techniques that are used to characterize and recapitulate silk structure–function relationships present challenges at the nanoscale given their limitations in chemical sensitivity (for example, electron microscopy and atomic force microscopy (AFM)) or limited spatial resolution (for example, 'far-field' infrared (IR) spectroscopy). In this context, my research focuses on the understanding of the conformational transitions of silk fibroin and recombinant spider silk, and the interaction between the protein and energy or other biomolecules at nanoscale using near-field optics. In particular, the complete conformational transition of the silk protein under the electron bombardment have been visualized, guiding the

creation of novel 3D nanostructures using Electron Beam Lithography (EBL). Meanwhile, the dual-tone structural formation of silk structures under ion beam irradiation have been thoroughly investigated, resulting in the "Protein Lego" manufacturing paradigm. The UV enabled silk protein cross-linking has also been utilized for scalable manufacturing of bio-structures. The interaction between the silk protein and other types of biological materials (such as cells, bacteria, and virus) has been studied to explore the stabilization capability of the silk matrix. The comprehensive investigation of the interplay between the protein material, energy input, as well as other chemical/biological species will pave the way for the bio-compatible, bio-degradable, and multi-functional platforms, serving as the building blocks of the green bio-manufacturing paradigm.

Table of Contents

List of Tables

List of Figures

Figure 13: The nanoscale analysis of conformational transition of spider silk proteins under increasing ion irradiation dosages. (A) The etching depth (black squares) and pattern height (red dots) of nano protein structures with changing ion beam dosages show three distinct stages, indicating conformational and property changes at the three stages. (B) The postulated mechanism of conformational transitions of the three different stages. For Stage Ⅰ, the low ion beam dosage can crosslink the amorphous spider silk to crystalline state, but the formed structure cannot reach the bottom of the film and firmly anchor the substrate. Therefore, the patterns can shift, rotate, and deviate from the original patterning position after water developing. For Stage Ⅱ, the ions can reach the bottom of the spider silk film, etch the crosslinked patterns, and break crosslinked structures to small peptide on the top surfaces of the fabricated patterns. For Stage Ⅲ, when the dosage is large enough, the structure can be totally carbonized. (C) Schematics of nanoscale IR spectroscopic spectrum using AFM-IR. The thermal expansion due to absorption of IR light is used to map absorption spectrum of the spider silk. (D) The IR near filed spectra of patterns before and after development upon different ion beam irradiation of 90, 180, and 360 $\mu C/cm^2$. The characteristic peaks are 1631 cm^{-1} (β-sheet, green dash), 1650 cm^{-1} (random-coil, blue dash), and 1662 cm^{-1} (α-helix, red dash), respectively. The curves show that with low ion beam dosage, the amorphous spider silk is crosslinked into more ordered state (α-helix and β-sheet). As the dosage increases, the crosslinked spider silk is broken down into short peptides marked by the decrease in the

Figure 20: Etching rate measurements and schematic structures of various UV-Silk and UV-LC. (a) Etching rate measurement of the UV-Silk30 and UV-LC with increasing exposure time. The etching rate of UV-LC decreases faster than the UV-Silk30 with increasing exposure time but reaches a constant rate that is higher than UV-Silk30; (b) Etching rate comparison between various UV-Silk (including both UV-Silk and methanol treated UV-Silk) and UV-LC at two exposure times (20s and 120s). All the samples with 20 s exposure times have larger etching rate than the samples with 120 s exposure times. UV-Silk has an increasing etching rate with increasing degumming time because the mechanical strength is better with longer chain length. UV-LC has slightly less etching rate because its highly defined molecular structure help form better crystalline structure; (c) Young's modulus of UV-Silk and UV-LC and ratio of Young's modulus before and after methanol treatment. It shows the similar trend with the data of etching speed, where the largest Young's modulus value corresponds to slower etching rate. It also shows no obvious change by treating with methanol, which indicates little amount of beta sheet structure present in UV-Silk and UV-LC; (d) Schematic structure and the corresponding etching rate of the photocrosslinked UV-Silk and UV-LC with 20 s exposure time and UV-Silk30 exposed for 120 s. For UV-Silk30, the etching rate decreases with longer exposure time because of the increased crosslinking degree. With the same exposure time, the etching rate increases with increasing degumming time because of the shorter chain length, and thus less mechanical strength. With 20 s exposure (partially crosslinking) UV-LC

INTRODUCTION AND BACKGROUND

Biopolymers, especially proteins, serve as the building blocks of life since they are produced by living matter to provide the most fundamental functions to creatures. There are thousands of types of proteins that possess different features in terms of their composition, conformation, and bio-activity. One of the most important types is the structural proteins, which provide intra- and extra-cellular structural support and an interface with the abiotic world (*1, 2*). The structural protein is one of the most abundant and physiologically diverse biopolymers with unique, repetitive amino acid sequences (e.g. GAGAGS for B. mori silk fibroin) that promote the formation of large, stable, and 'crystalline' domains through self-assembly (*3*). The hierarchically organized crystalline structures, which often possess the form of fibers, are evident in many structural proteins including collagens, keratins and silks, and represents their distinct feature. The word "structural proteins" is commonly used to describe family of proteins with similar amino acid composition and characteristics. Their classification is sometimes debated because of the deviation from their common use in plain language. For example, the word 'collagen' covers a large family of proteins ubiquitous in animals and some fungi. Collagens are secreted from cells to form extracellular matrix and connective tissues both in fibrillar and non-fibrillar form (*4*). Similarly, 'silk' is a term used to describe a family of protein fibers spun (i.e. extracellularly made insoluble in filament form from an aqueous protein solution) by a number of arthropod lineages. Many insect species produce silk for a wide variety of purposes (*5*). It has then been proposed that the silk production capability has evolved multiple times among insects and that each origin has led to a novel silk 'lineage', which can be identified by grouping silks according to their gland of production, molecular structure, and phylogenetic distribution. In recent years,

considerable research efforts have centered on the silk extracted from B. mori caterpillars and on dragline silk of spiders due to their outstanding mechanical properties.

Chapter 1: Introduction to the silk protein

THE STRUCTURES OF SILK

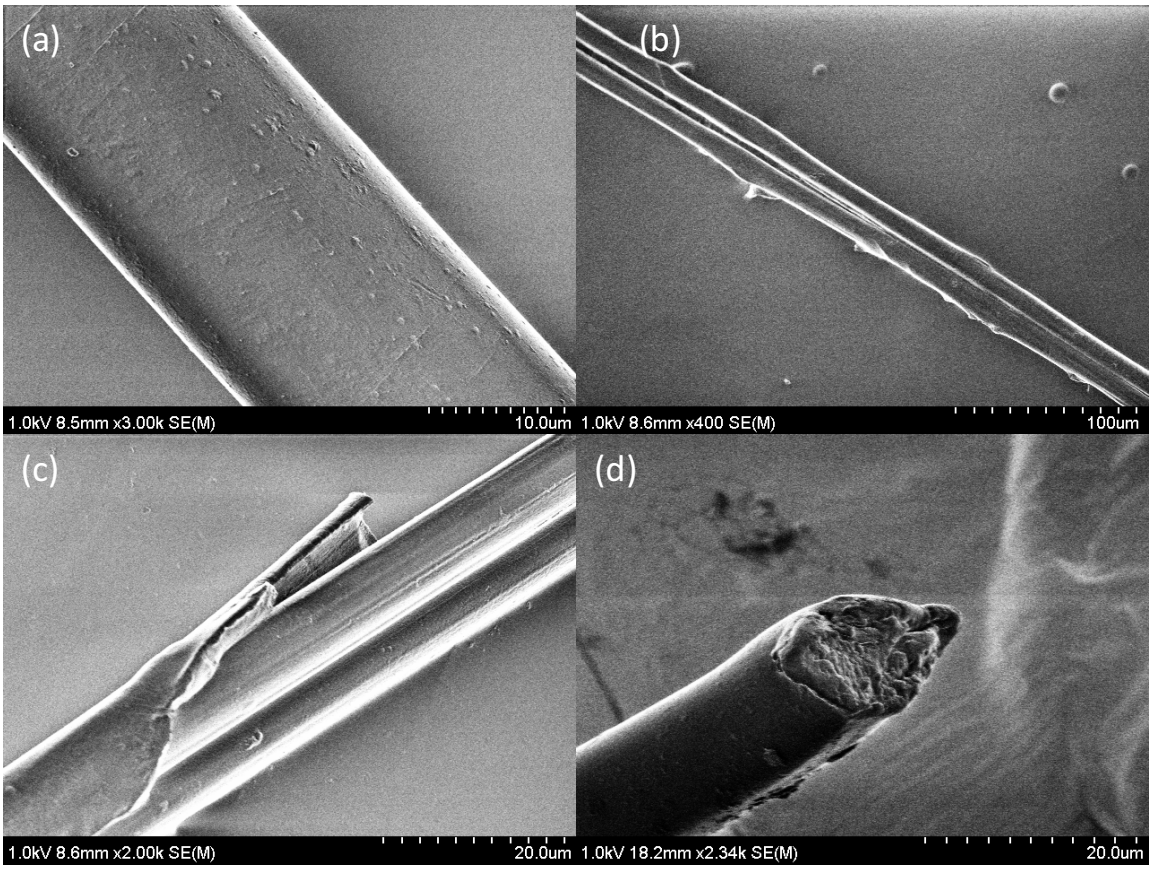

Figure 1: SEM images of the B. mori silk fiber. (a) The raw silk fiber (b) the double fibroin cores that compose a single raw fiber. (c) the double fibroin cores exposed by peeling off the sericin (d) the cross-sectional view of a single fibroin core.

The domesticated silkworms, or also known as the B. mori silkworms, produces fibers with a diameter of about 10μm (*6*). Each fiber is usually consisting of two strands of fibrous cores, covered and glued together by another protein (As shown in Figure 1). The protein that assembles into the fibrous cores, which often have a triangular cross-section, are called fibroin (which account for ~75% of the weight of silk fibers) while the glue protein is called sericin (which account for ~25% of the weight of silk fibers). The

highly crystallized fibroin is the component that provides the mechanical robustness to the silk fibers and is used for a wide range of applications. Therefore, this dissertation will be devoted to the discussion of the fibroin.

The fibroin protein consists of two major components with a ratio of 1:1 – a light chain segment (~26 kDa) and a heavy chain segment (~390 kDa) linked together by a disulfide bond between the Cys-c20 of the heavy chain and Cys-172 of the light chain (*7, 8*). In terms of the amino acid composition, the silk fibroin is mainly composed of glycine (Gly) (43%), alanine (Ala) (30%) and serine (Ser) (12%)(*9*). The heavy chain consists of 12 domains that form the crystalline regions (β-sheets) of the fiber, interspersed with short and less organized domains (helices and coils). The primary composition of the crystalline region is Gly-X repeats, with X being Ala, Ser, Threonine (Thr) and Valine (Val). The most common repeating units in these regions are GAGAGS, GAGAGY, or GAGAGA (*10, 11*). These sequences result in hydrophobic components with a natural co-block polymer design. Therefore, the hydrogen bonding between the repeating units assemble into the β-sheets and provides the mechanical strength to the fiber. The non-repeating units, on the other hand, forms random coils, β-spirals, and α-helices that account for the elasticity of the fibers.

THE MECHANICAL PROPERTIES OF SILK

The silk fibers are renowned for the exceptional mechanical properties and has been used for the textile industry for centuries (*12-14*). Here in table 1, the mechanical properties of the silk protein and other commonly seen biodegradable materials are summarized.

Source of Biomaterial	Modulus (Gpa)	UTS (Mpa)	Strain at break (%)	Reference
B. Mori silk (with Sericin)	5 – 12	500	19	(15)
B. Mori silk (without Sericin)	15 – 17	610 – 690	4 – 16	(15)
B. Mori silk	10	740	20	(16)
N. Clavipes silk	11 – 13	875 – 972	17– 18	(16)
Collagen	0.0018 – 0.046	0.9 – 7.4	24 – 68	(17)
Crosslinked Collagen	0.4 – 0.8	47 – 72	12 – 16	(17)
Polylactic acid	1.2 – 3.0	28 – 50	2 – 6	(18)

Table 1: The mechanical properties of the silk protein and other common types of bio-degradable materials. (*15-18*)

As evident from the Table 1, both the Modulus and the ultimate tensile strength (UTS) of the silk protein is superior than other common biomaterials such as collagen and polylactic acid (PLA). This is again mainly attributed to the high content of crystalline β-sheets domains of the heavy chain. However, the elasticity of the silk fiber in general is lower than the softer bio-polymers since the β-sheets tends to be rigid.

THE RE-ENGINEERING OF SILK

Silk has a rich history as a material for manufacturing. Before the 'micro' and 'nano' technological revolutions that have spanned for the last two centuries, structural proteins have been used mostly in their natural forms, i.e. fibers and tissues produced by animals, for millennia. In the last a few decades – given the advances in science and technology and the increasing demand to find suitable materials to harmlessly interface with cells and different tissues in the human bodies – silks have also found extensive

application in biomedical fields, including wound healing (*19*), tissue engineering (*20*), regenerative medicine (*21*) and drug delivery (*22*). Silk and other types of structural bio-polymers possess the merits of non-toxicity, biodegradation, support of cells growth and differentiation, and mechanical strength (*23-25*) that are difficult to find in synthetic materials and that have enable the use of silks in many 'biocompatible systems'(*26-29*). Biomedical devices made of structural proteins have been fabricated using materials both in their natural form (e.g. silk fiber-made ligament grafts) or through the regeneration of 'raw' natural materials in suspensions of protein nanoaggregates that have then been processed in several materials formats, including hydrogels, films and nanofibers (*28, 30-33*).

Since the regenerated silk solutions is a convenient precursor to a wide range of material formats, the research on the regeneration process have been thoroughly studied. A well-established protocol has been reported in the literature for extracting the silk fibroin from the raw silk fiber and then dissolve it into a water based salt solution.

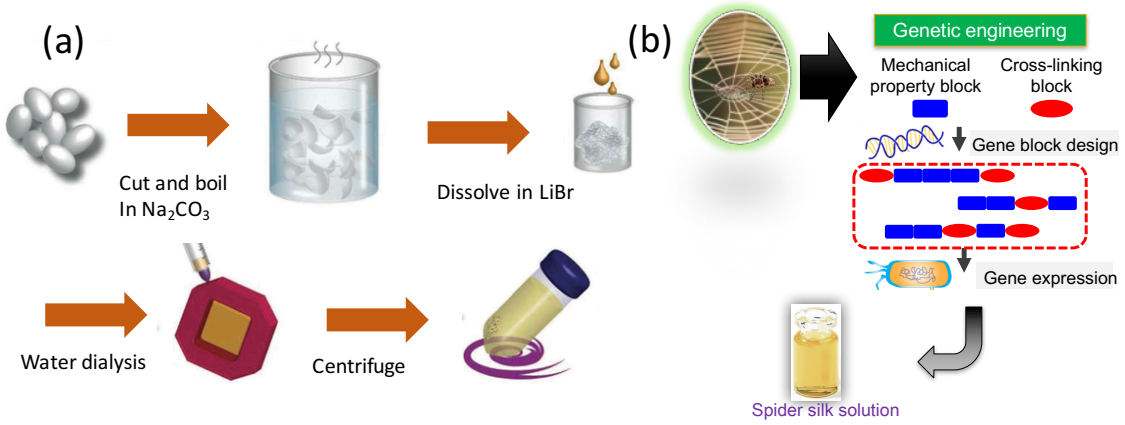

Figure 2: The process of obtaining regenerated silk solution and the recombinant spider silk. (a) the silk fibroin protein can be separated from the raw silk cocoons by boiling the raw fibers in the Na_2CO_3 solution. The resulting fibroin is dissolved in the LiBr solution and then purified through dialysis against DI water and the centrifugation. (b) the recombinant spider silk can be obtained by grafting the DNA segment from spiders that express the Spideroin protein into the e. coli.

The protocol of extracting the silk fibroin from the raw fibers involves several water-based processes (*30*). Firstly, the silk cocoon is cut up into small pieces and boiled in the Na_2CO_3 solution. During this step, the sericin is dissolved into the solution and therefore separated from the fibroin. This is called the degumming step, where the temperature and duration of the degumming determines the partial degradation of the fibroin protein chain (*34*). The fibroin is then dissolved into the aqueous LiBr solution. During this step, the crystalline domains of the fibroin is de-folded into amorphous states, yielding a suspension (or solution) of silk fibroin nano-aggregates dispersed uniformly in the LiBr solution. The pure silk/water solution can be purified from the mixture through dialysis against deionized water (DI water) and the particular contaminants is removed by centrifugation. The resulting aqueous silk solution is a uniform, light-yellow-colored and transparent liquid as shown in Figure 2A.

On the other hand, a very similar type of natural fibrous protein – the spider silk (spideroin) – possess even better mechanical properties than the silk fibroin, which is also ideal for a wide range of applications. However, the territoriality and the cannibalism of the spiders make them difficult to farm and therefore the mass production of spider silk has been impractical. Therefore, genetic engineering is resorted to produce the recombinant spideroin (*5, 35-39*). The DNA segments in the spider that is used to express the spideroin is grafted to e. coli, which will then produce the spideroin in a controlled environment. Although the yield of this method is fairly low, the genetic engineering method of producing spideroin has a few advantages. First of all, the purity of the product can be well controlled and since the protein is directly express into a water based solution, there is no need for dissolution steps that could degrade the protein. In addition, since the DNA of the e.coli can be further modified, genetically modified spideroin with desired properties (such as high elasticity, cell adhesion, and fluorescence) can be produced by grafting the appropriate DNA segment.

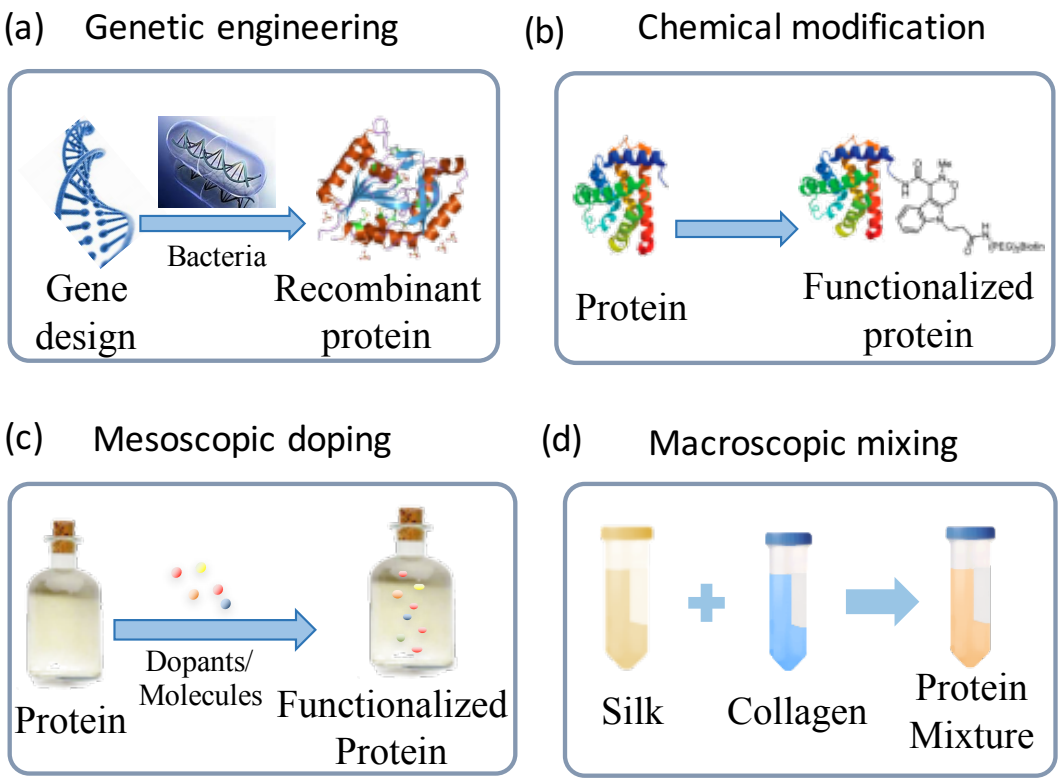

Figure 3: The multi-level modification of the natural/regenerated silk proteins. (a) The silk protein can be modified directly by altering the genes of the silkworms through genetic engineering. (b) chemically conjugated silk protein have also been successfully demonstrated. Even simpler methods such as (c) mesoscopic doping and (d) macroscopic mixing can be utilized to produce customized silk.

Besides obtaining the regenerated proteins, which possess the original properties (mechanical, chemical, and biological) of the natural silk fibroin, sometimes additional functionalities needs to be imposed on the material for the target applications. This is where the versatility of the silk based platform is well manifested in the diverse ways of modifying the silk material (Figure 3). For example, the silk protein can be directly modified by inserting the transgene into the silkworm genome to acquire the desired properties such as fluorescence (*40*). The raw silk fiber and regenerated silk protein can

also be functionalized by conjugating a wide variety of chemical compounds to the amino acid side groups. Using this method, enhanced cell adhesion, direct protein assembly, as well as UV sensitization have been realized (*41-44*). Moreover, thanks to the aqueous nature of the regenerated silk solution, much simpler methods such as mesoscopic doping and macroscopic mixing can be used to grant desired functionality to the silk material.

	Resolution	**Mode**	**Dimension**	**Structural transformation**	**Ref.**
EBL	~ 10 nm	Serial	2D & 2.5D	Yes	[1-2]
IBL	~ 10 nm	Serial	2D & 2.5D	Yes	[3]
SL	~ 40 nm	Parallel	2D & 2.5D	No	[4-5]
Nanomprinting	~ 50 nm	Parallel	2D & 2.5D	Yes	[6-7]
Self Assembly	~ 200 nm	Parallel	3D	No	[8-9]
MPL	~ 350 nm	Serial	3D	Yes	[10]
UVL	~ 1.5 μm	Parallel	2D & 2.5D	Yes	[11-13]
Inkjet Printing	~ 10 μm	Serial	2D & 2.5D	No	[14]
3D Printing	~ 50 μm	Serial	3D	No	[15]
Engraving	~ 100 μm	Parallel	3D	No	[16]

Table 2: The feature characteristics of the nanofabrication using silk as the resist material. The minimum feature size, fabrication mode, achievable feature dimension and the fabrication induced silk structural transformation is summarized (*45-58*).

The multi-level modification equips silk with a variety of additional excellent properties, and, to further expand the applications of silk, the manufacturing of silk-based architectures is necessary. Over the last few decades, manufacturing has undergone tremendous development, and numerous manufacturing techniques are emerging. The combination of manufacturing technology and biomaterials offers new opportunities in the engineering design space. In this context, biomanufacturing, a highly interdisciplinary field, seeks to create novel bioarchitectures as functional devices and interfaces, and

attempts to integrate inorganic and organic components for new properties and functions, which have the potential for a wide variety of biological research topics and medical applications. Numerous research efforts have been invested in the biomanufacturing, inspired by the existing integrated circuit (IC) manufacturing and microelectromechanical system (MEMS) fabrication. Multi-scale manufacturing for silk based materials has been developed, including electron-beam lithography (EBL)(*45, 46*), ion-beam lithography (IBL), soft lithography (SL)(*48, 59*), nano-imprinting lithography (NIL)(*49, 60-62*), self-assembly (*51, 52*), scanning probe lithography (SPL)(*63*), multi-photon lithography (MPL)(*53, 64*), direct pattern transfer (*65*), bio-inspired spinning (*33, 66*), covering from nanoscale to macroscale. The fabrication characteristics of the silk based biomanufacturing are summarized in Table 2.

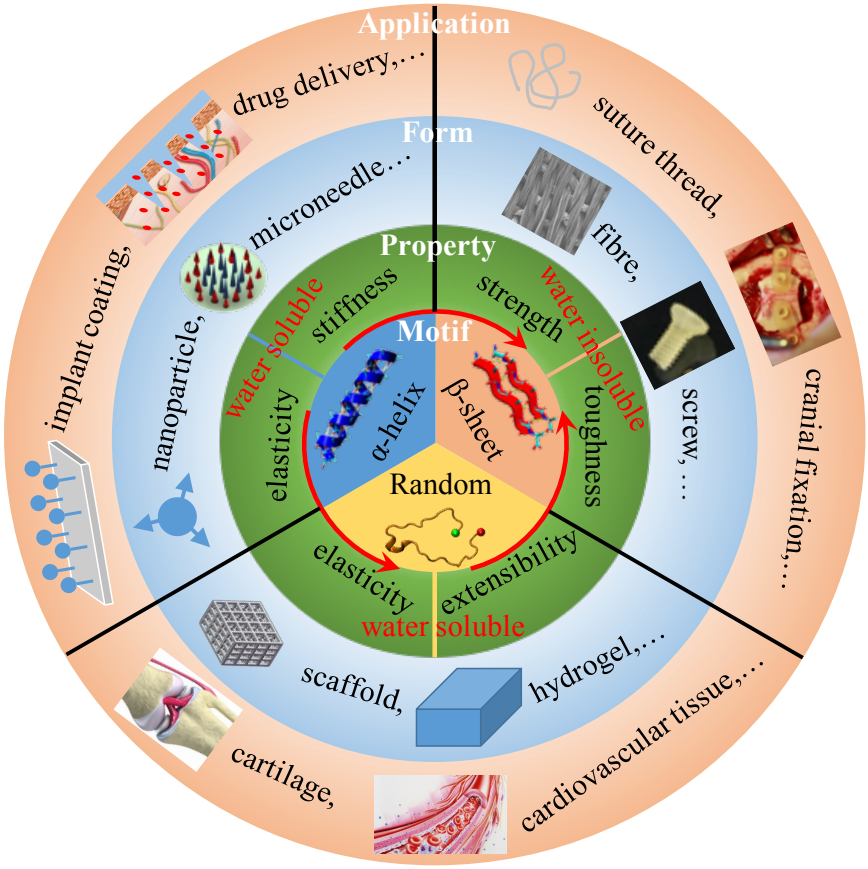

Figure 4: The interplay between the structure, form, and material properties with the targeted application using the silk protein

With the advancement of manufacturing technology, the silk material has gained considerable momentum as a material for applications beyond the structural components, such as optoelectronics, implantable photonics, drug delivery (Figure 4). The main reason beyond the reinvention of silks as a technical material for optoelectronics originates from its polymorphism, which is defined as the possibility to obtain stable conformation in several secondary and tertiary structures, ranging from random coils, to β-sheets and helices (e.g. 310 helices, α-helix and β-turn type II). Silk fibroin polymorphism facilitates the processing of silk fibroin with controlled crystallinity, which have different degrees of solubility in water. Modulation of water solubility enabled the processing of

the structural protein in multiple material formats using advanced fabrication techniques, ranging from electron-beam lithography to ink-jet printing. Water-based processing conditions has also allowed for the incorporation and stabilization of inorganic and organic molecules in silk fibroin materials, which have imparted unusual functions to silk materials as sensing, diagnostics and therapeutics platform. Thus, understanding the interplay between folding and assembly phenomena of silk is the key to develop new manufacturing techniques that can shape structural proteins in unprecedented, technical, materials formats not found in nature.

Chapter 2: Introduction to near-field optics

THE CURRENTLY USED TOOLS FOR CHARACTERIZING SILK

Understanding the structure-function relationship in silk materials requires a deep and wide investigation of protein domains as secondary and tertiary structures impart structural morphology and modulate material performance. At the molecular level, silk domains can be postulated by studying the protein IR spectrum.

Wavenumber range, cm^{-1}	**Assignment**
1605 – 16165	(Tyr) side chains/aggregated strands
1616 – 1621	Aggregate beta-strand/beta-sheets (weak)
1622 – 1627	Beta-sheets (strong)
1628 – 1637	Beta-sheets (strong)
1638 – 1646	Random coils/extended chains
1647 – 1655	Random coils
1656 – 1662	Alpha-helices
1663 – 1670	turns
1671 – 1685	turns
1686 – 1696	turns
1697 – 1703	Beta-sheets (weak)

Table 3: The characteristic absorption band of protein based materials in the Amide I region. The strong absorption in the 1622 – 1637cm^{-1} is an indicator of the crystallinity of the material and therefore frequently used to characterize the conformation of silk. Other significant absorption bands such as α-helix and random coils are also useful in the identification of silk structural transition.

Amide bonds in silk protein possess characteristic absorption bands in the infrared spectrum, namely the amide vibrations (or bands). Among the nine amide band, Amide I (mostly due to the C=O stretching) and Amide II (due to the in plane NH bending and CN stretching vibration) bands are the most significant vibrational modes and are widely

used to investigate secondary and tertiary structures of proteins (*67-70*). Measurement of the IR spectrum can be carried out using FTIR (Fourier transform infrared spectroscopy), which obtains the infrared absorption of a material using interferometric method. The most commonly referred characteristic IR absorption band of the protein based material is summarized in Table 3. FTIR is a well-established and reliable characterization tool to study formation of protein domains in a bulk material.

THE SCANNING NEAR-FIELD OPTICAL MICROSCOPY

Advancements in the silk nano-engineering pose significant challenges to the characterization of material properties at the nanoscale. The nano-engineering of the silk protein dictates that the minimum feature sizes created by the fabrication technologies are sub-micron scale. In addition, the inherent heterogeneity of the biomaterials require that the study of the material properties can distinguish the nanoscale variation of material structure with high resolution (e.g. silk materials performances are modulated by the amount of β-sheet domains in the material) (*3, 71, 72*). Thus, investigating protein conformation at the nanoscale is fundamental to understanding material behavior. Conventional methods such as FTIR, scanning electron microscopy (SEM), and atomic force microscopy (AFM) are either limited by their spatial resolution (i.e. FTIR) or chemical sensitivity (i.e. SEM and AFM).

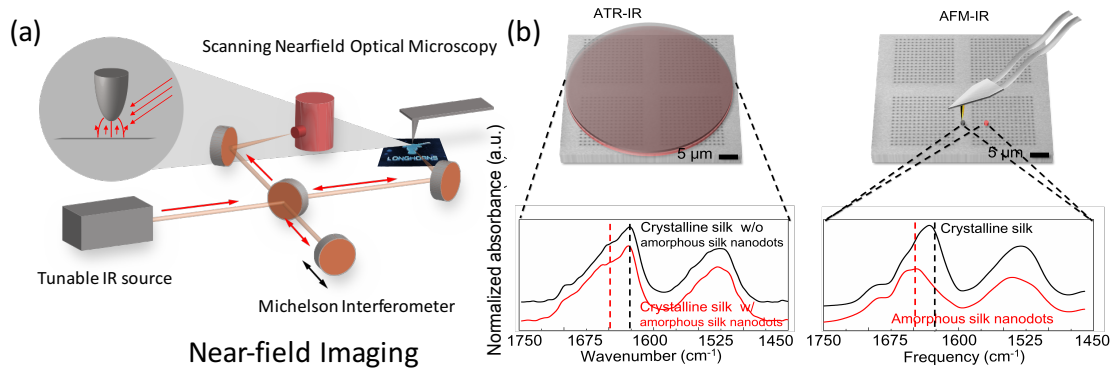

Figure 5: The schematic of the scanning near-field optical microscopy (s-SNOM). (a) An IR laser is focused on a sharp, metallic AFM tip, which induces the scattering of the underlying sample within a distance of a few tens of nanometer. (b) the advantage of using the s-SNOM is that the lateral resolution is not constrained by the diffraction limit, and only dependent on the radius of the tip apex.

In particular, the IR imaging/spectroscopic techniques that are used for material characterization usually involves the usage of IR light, which is a wave in nature. All propagating waves are subject to a focusing limit dictated by the Rayleigh Criterion:

$$d = \frac{\lambda}{2nsin\theta}$$

The d means the closest distance between two points at which they are still discernable by the light of wavelength λ. The Rayleigh Criterion says that the smallest point a light wave can be focused into is roughly half of its wavelength. In the IR light case, the resolution is limited in the micron size. Even with conventional visible light microscopy, the best resolution is only ~200nm. The demand for a higher resolution than 200nm have spawned many inventions that overcome the diffraction limit. Some of the methods involve using particles with smaller effective wavelength. For example, the SEM uses a beam of electrons to shine on the sample surface, which is scattered/reflected back and then collected by the electron detector. Since the electron can be treated as a DeBroglie wave with an effective wavelength in the nanometer range (depends on the kinetic energy

of the electrons as well), the diffraction limit and therefore the resolution of the SEM can be achieved in the ~10nm range. Other methods take advantage of the usage of a sharp solid state probe that is not subject to the light diffraction. Methods developed based on this principle are Atomic Force Microscopy (AFM), Scanning Tunneling Microscopy (STM). The STM can even surpass atomic resolution and has successfully been used to visualize crystal structures of materials.

In this context, IR scanning near-field optical microscopy (IR-SNOM) was successfully used to study the nanoscale details of silk conformation (Figure 5). The IR-SNOM is derived from the usage of AFM and the coupling between light and a sharp tip. Currently, SNOM has been widely applied in the characterization of a variety of solid state and polymer samples, including grapheme plasmonics (*73*), phase transitions in correlated electron materials (*74*), mineral polymorphs (*75*) and secondary structure analysis of single-protein complexes (*76-80*). The earliest idea of the SNOM is from Synge, who proposed a method for high resolution optical imaging by using an opaque screen with a small aperture on it. The aperture is hold very close to the specimen to prevent the diffraction. This design is later implemented by Ash and Nicholls in 1972 using microwave of ~3cm wavelength. Later on, the design was optimized to operate on a metal coated single mode optical fiber with a small opening at the end. The resolution of this type of SNOM is improved with smaller aperture size. However, the transmission efficiency also decreases significantly as the aperture size decreases. This limit this SNOM to practically operate at $\lambda/10$.

An alternative method of SNOM that completely achieves higher resolution independent of the incident wavelength is proposed by Wessel in 1985. His work suggests to take advantage of the enhanced field in the vicinity of a small particle for illuminating the sample. This idea is implemented using a metallic AFM tip by

Zenhausern et al and Inouye and Kawata in 1994. The metallic AFM probe creates a "nano focus" of the incident light, which is an evanescent wave in nature, significantly improves the focus power to less than 10nm. The interaction between the tip and the specimen modifies the amplitude and/or phase of incident light, which is scattered by the probe and subsequently detected in the far-field. During this interaction, elastic scattering dominates the scattering channel where both the tip-sample interaction and the background scattering is both present. This actually presents as one of the big challenge of using the s-SNOM in practical settings.

To suppress the background, a demodulation method is proposed, which is conveniently facilitated by the tapping mode of the AFM. During the tapping mode operation, the AFM tip oscillates in the z-direction with its resonance frequency Ω. As the probe scans across the sample surface, the average tip-sample distance is maintained to be constant through a feedback controller. This operation mode offers a natural way of modulating the near-field signal. This is because the near-field interaction between the tip and the sample is evanescent in nature, and changes drastically with the distance. Fortunately, the background scattering only changes slightly as the tip moves away from the sample. Therefore, the collected IR signal contains an almost constant background with a periodically varying scattering due to the near-field interaction. Consequently, demodulating the detected signal with a frequency of Ω, or integer multiples of Ω, can effectively separate the background noise from the real signal. As the demodulating order increases, the signal is more free from the background, but with less amplitude, which is subject to other types of noise. In practice, the signal is usually demodulated at the 2nd or 3rd harmonics.

The multi-modal data acquisition of IR-SNOM allows simultaneous measurement of structural morphology, mechanical property and conformation of the sample,

significantly enhancing the capability to understand the structure-property correlation. This is particularly exciting for biological material studies because of the heterogeneity of the materials. Nanoscale resolved characterization enables detailed study of nano-domains of biological samples, whose property could be significantly different from the bulk material (*81-83*). When the IR laser is focused on the sharp, conductive AFM tip, the oscillating electrical field of the laser polarizes the tip, yielding an effective dipole moment of $p = \alpha_{eff}(1 + r_s)E_i$, where α_{eff} is the effective polarizability of the tip that takes into account of the tip-sample interaction (in the near-field) (*84*). There are a few modeling methods to describe the tip by either regarding it as a dipole or simply a point charge. Both have been successfully demonstrated to predict the interaction between the sample and the tip. This interaction is confined within the radius of the tip apex, and therefore is not dependent on the wavelength of the incident laser (*75, 85, 86*). To use the measured IR data to construct a IR spectrum, a reference material that is spectrally featureless is usually required. The most commonly used materials are gold and silicon. By comparing the signal contrast between the sample of interest and the reference material, the spectrum can be mapped out.

THE THERMAL BASED NEAR-FIELD MEASUREMENT – AFM-IR

In fact, two types of IR-SNOM based on conductive AFM tips are available for the study of silk protein. As mentioned above, the scattering type SNOM (referred to as s-SNOM) offers direct near-field imaging of protein nanostructures. IR beam scattered by the sharp and conductive AFM tip is collected by the IR detector and demodulated at the harmonics of the AFM tip. Through a pseudo-heterodyne detection scheme, infrared absorption of the sample can be obtained (*81*).

On the other hand, thermal expansion based SNOM (referred to as AFM-IR) can be used to acquire the absorption spectrum of the sample at the nanoscale (*87*). In this case, a pulsed laser is coupled to the AFM tip where the IR absorption of the sample causes the rapid expansion of the sample surface, which is sensed by the contact mode AFM. By sweeping through the wavelength of the IR source, the local absorption spectrum of the sample can be obtained (*88, 89*). Upon optical absorption, the molecules changes into an excited vibrational state. In a very short amount of time (usually pico-seconds), the vibrational mode dissipates this energy to the vibrational and kinetic mode of the surrounding molecules. Because of the molecular vibrations, the effective molecular volume increases. On the macroscale, the sample thermally expands, and lead to a mechanical force acting on the AFM tip that is in direct touch with that area. In the first approximation, the thermal expansion is linearly proportional to the energy absorbed. Therefore, the degree of thermal expansion of the sample at different wavelength normalized by the incident power should correspond to the absorption of IR light. By sweeping through different wavelength in the laser source, the complete IR spectrum of the sample can be obtained. The early demonstration of the thermally excited IR detection can only be conducted on thick materials because of the limited expansion. However, with the usage of a metallic tip and a highly reflection substrate (such as gold), the signal can be greatly improved due to the enhancement at the AFM tip. Hence, the resolution of this technique is also in the nanoscale as the enhancement and the detection is only confined within the apex of the AFM tip. The expansion is further optimized by utilizing a pulse laser, where the peak power is significantly higher than the average power. In addition, by tuning the repetition frequency of the incident laser to be the same as the AFM tip oscillation resonance, the expansion is further enhanced.

The characteristic peaks of the IR spectrum can then be correlated to the secondary structures of proteins (*90-92*). Both tools are valuable to the study of the silk conformation and nanostructures, and have been used to investigate the electron irradiation regulated silk conformation transitions. For silk fibroin, the β-sheet structure corresponds to an IR absorption peak at ~1622cm^{-1} - 1637cm^{-1} whereas the amorphous state and the α-helix conformation correspond to an absorption peak at ~1656cm^{-1} - 1662cm^{-1} (*93*). The results provide significant insight into the engineering of silk protein using electrons and thus proves the applicability of the SNOM technique on the studying of silk material.

RESULTS AND ANALYSIS

With the advanced manufacturing tools (e.g. EBL, IBL, and Photolithography) and the nanoscale characterization platform (e.g. s-SNOM, AFM-IR), the structural transition of the silk protein under the energetic particle bombardment can be well controlled and visualized. In this chapter, the study of the silk conformation cycle under the irradiation of electrons, ion, and photons are presented. The results provide significant insight into the mechanism of silk polymorphism and serve as an important guide towards the re-engineering of silk for bio-photonics, sensing, transient electronics, and biomimetics. In addition, the interaction between the silk protein and other biological samples (such as enzyme, antibody, and virus and cells) is discussed, laying the foundation of using silk as the stabilizing agent for a variety of biological applications.

Chapter 3: The silk conformational transitions regulated by electrons

INTRODUCTION OF EBL FABRICATION ON THE SILK PROTEIN

Electron Beam Lithography (EBL) is a mature technology of making submicron patterns on a substrate covered with a thin material called "resist". Standard Electron Beam Lithography works by focusing a beam of electron on the resist material, locally causing the resist material to crosslink/decrosslink, and thus regulating its solubility in certain solvents (*94*). The resolution of EBL is related to the electron acceleration voltage, and 50nm is usually achievable in commercial EBL machines with 50 KeV. The resist material can be divided into two categories: positive and negative. Positive EBL resist starts as an insoluble material, and, upon exposure to electrons, becomes soluble. Therefore, during developing step, the area that was exposed by electrons will be washed away. The negative EBL resist is the opposite. The material starts out as soluble, but upon electron exposure, the material becomes insoluble. The area that is exposed will stay on the substrate in the subsequent development step. During these process, the standard resist experience crosslink/de-crosslink transition. Silk film can also be patterned with EBL technology, but the mechanism is slightly different. Instead of experiencing a chemical crosslinking/de-crosslinking process, the silk secondary structure changes from a random state to an ordered state (either α-helix or β-sheet), and the associated solubility in water determines the tone of silk as a resist (*45, 95*). For example, the amorphous state silk film is soluble in water. However, with the bombardment of the electrons, the protein molecules tend to assemble into a more stable β-sheet conformation,[1] and become insoluble in water. Therefore, the amorphous state

[1] This section is based on the following article. The author of this dissertation is the co-first author on this paper. Qin, N., Zhang, S., Jiang, J., Corder, S. G., Qian, Z., Zhou, Z., . . . Li, X. (2016). Nanoscale probing of electron-regulated structural transitions in silk proteins by near-field IR imaging and nano-spectroscopy. Nature communications, 7, 13079.

silk film[2] serves as the negative tone EBL resist. On the other hand, the crystalline silk film behaves in the opposite way, and can be used as a positive tone resist.

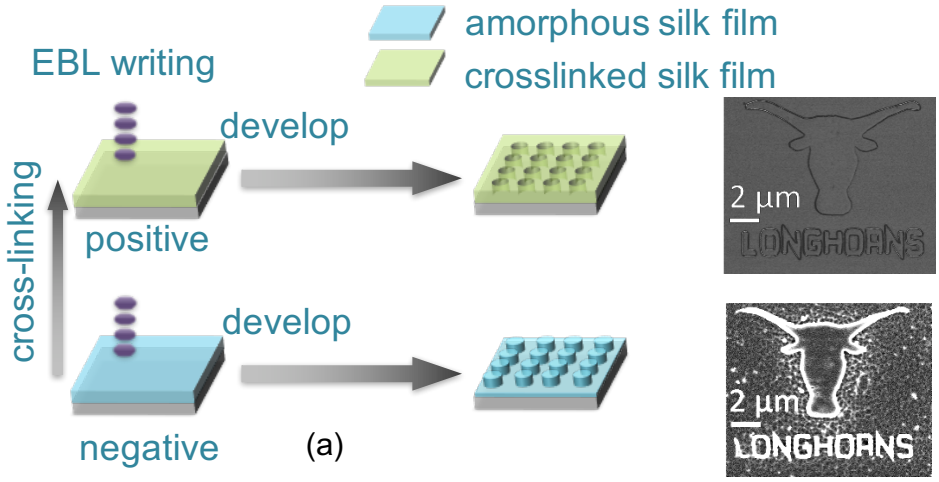

Figure 6: The schematic of the silk film as both positive and negative tone electron beam lithography resist. The amorphous silk film is originally soluble in water, and upon the exposure of the electron beams, the exposed area becomes insoluble in water. Therefore, the pattern remains on the substrate after development, featuring a negative tone resist characteristic. On the other hand, the crystalline silk film (with a high content of β-sheet crystals) is insoluble in water. However, with the electron irradiation, the hydrogen bonds are broken and the protein become partially amorphous. Therefore, the exposed area will be washed away during the development step, featuring a positive tone behavior.

THE NANOSCALE INVESTIGATION OF THE SILK TRANSITION USING SNOM

The material behavior of silk as an EBL resist is highly correlated to the molecular arrangement and organization. Therefore, understanding the hierarchical formation of protein structures at their fundamental length scales will help to recognize essential nanoscopic protein structures and critical conditions for conformational transitions, which in turn provides insight into refined protein nanostructuring - the major

2

objective of this work. Characterization of the mechanisms and electron-induced structural modifications were carried out using infrared scanning near-field optical microscopy (SNOM). SNOM has been previously applied in the identification of spectroscopic signatures in a variety of solid state and polymer samples, including direct imaging of Plasmon propagation on graphene, nanoscale-mapping of phase transitions in correlated electron materials, chemical identification of mineral polymorphs, and secondary structure analysis of single protein complexes.

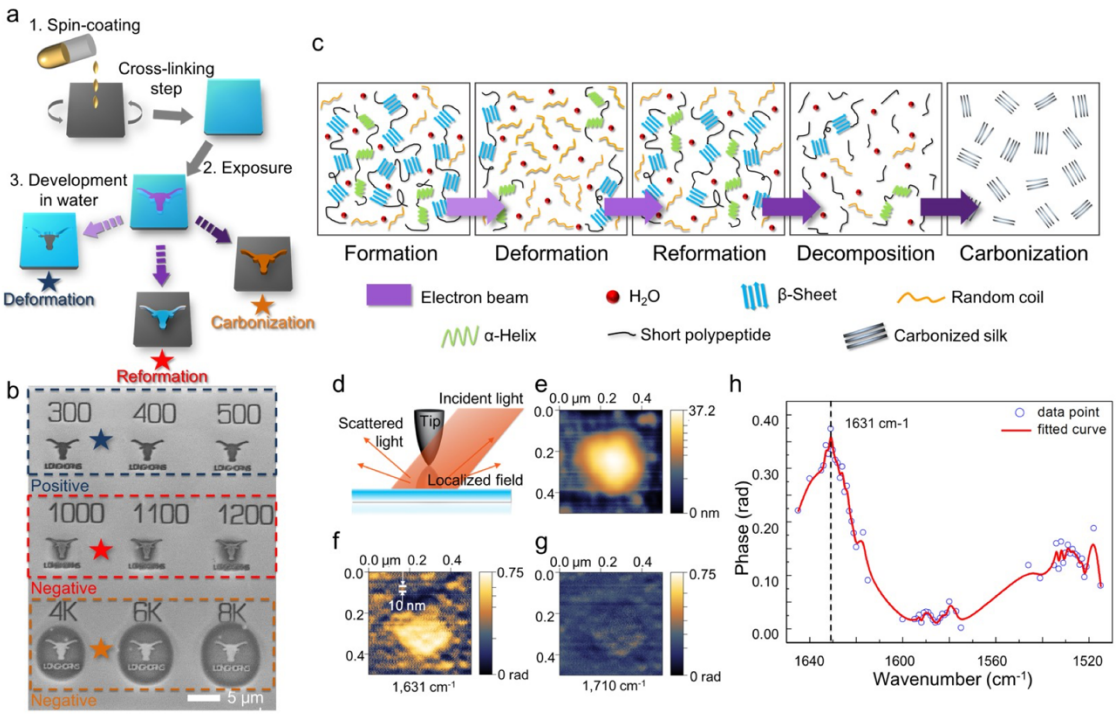

Figure 7: Electron-regulated nanoscale structural transitions in silk proteins. (a) Illustration of the "polarity/tone switching" (i.e., positive tone to negative tone due to structural transitions) of crystalline silk in EBL. (b) SEM images of nanopatterned crystalline silk as positive or negative resist on the same substrate (due to different structural transitions) depending on ebeam dosages. (c) Schematic illustration of β-sheet-oriented structural transitions regulated by electron energies. (d) Schematics of nanoscale IR spectroscopic imaging using s-SNOM. (e) Topography of silk nano-aggregates (β-sheet rich) on a silicon substrate. (f) & (g) Near-field IR phase images at 1,631 cm^{-1} and 1,710 cm^{-1}, respectively. (h) Local infrared

absorption spectra (symbols) depicting the normalized near-field phase signal of crystalline silk by sweeping the output wavenumber of the QCL and using nano-spectroscopic imaging. (*46*)

By studying the material behavior at the nanoscale, in this work, we found that either amorphous or crystalline silk (or intermediate conformational states) can be used in both positive and negative tones. The applied electron dosage is the primary tuning parameter and plays a more important role than the crystallinity of the starting materials. For example, positive (low dosage) and negative (high dosage) EBL were simultaneously achieved on the same crystalline silk protein substrate as the starting material. The EBL exposed silk film then undergoes the same water development process (Figure 7A – 7B). The control of polymorphic transitions in silk proteins allows us to explore a complete structural transition (i.e., formation, deformation, reformation, decomposition, and carbonization) of β-sheet nanocrystals regulated by precise delivery of electron energies with nanoscale resolution (Figure 7C).

In this work, SNOM has been utilized to characterize the silk nanostructures with resolution beyond the diffraction limits of conventional optics and register nanoscale spectroscopic signatures of silk in the IR frequencies. Two SNOM systems have been used and the results have been analyzed in direct comparison: one for near-field imaging (i.e., scattering-type SNOM, referred to thereafter as s-SNOM) and another for nano-spectroscopic studies (i.e., thermal-expansion-based SNOM, referred to as AFM-IR), respectively. Based on an atomic force microscope (AFM), s-SNOM provides direct imaging and chemical contrast of silk proteins relative to a reference material (e.g. Silicon and Gold) with spatial resolution of ~ 10 nm, significantly enhancing the ability to probe local chemical compositions. In comparison, with AFM-IR nano-spectroscopy, the IR spectrum can be directly mapped. The IR absorption of the silk specimen causes a rapid local thermal expansion. By tuning the repetition rate of the incident laser, the

expanded surface excites resonant oscillation of the AFM cantilever. Since the amplitude the expansion is directly related to the amount of IR light absorbed, frequency-dependent IR absorption spectra can be obtained. In our case, each absorption peak corresponds to a specific molecular resonance of the silk proteins (i.e. random coil and β-sheets), providing a unique chemical fingerprint at the nanoscale.

In order to obtain high-resolution optical images and spectroscopic information to map out the nano-chemical and nano-mechanical properties of silk proteins at the molecular level, an s-SNOM (NeaSNOM, Neaspec GmbH, Germany) is coupled to a tunable IR quantum cascade laser (QCL, Daylight Solutions Inc., USA) covering a broad infrared spectra of the amide I and II bands over the range from 1,495 to 1,790 cm^{-1} (Figure 7d). The near-field phase spectrum resembles the molecular absorbance band, while the near-field amplitude spectrum acquires a dispersive line shape similar to a far-field reflectivity spectrum. Figure 7E shows a topographic image of regenerated silk protein aggregates with high β-sheet contents, with sizes ranging from ~ 10 nm - 350 nm, spin-coated on a silicon substrate. Figure 7F – 7G show near-field IR phase images taken at 1,631 and 1,710 cm^{-1}, respectively. All IR nanoimaging was performed at a spatial resolution of ~ 10 nm approaching the molecular limit of silk proteins, e.g., a B. mori silk fibroin (~ 7.8 nm) - as a model protein investigated in this work - consists of one light chain (~ 2.4 nm) and one heavy chain (~ 4.2 nm) linked by a disulfide bridge. At 1,631 cm^{-1}, the phase image exhibits strong contrast between silk and silicon (silicon is used as the reference for IR imaging) owing to the amide I absorption corresponding to the secondary structure of β-sheets. This phase contrast vanishes when the illumination is tuned to 1,710 cm^{-1} where silk proteins show little absorption. Local infrared absorption spectrum (symbols) depicting the normalized near-field phase signal

of crystalline silk (i.e., β-sheet rich) was acquired using IR nano-imaging by sweeping the probing wavenumber/wavelength during nano-spectroscopic imaging (Figure 7H).

THE VISUALIZATION OF SILK CONFORMATION REGULATED BY THE ELECTRON IRRADIATION DOSAGE

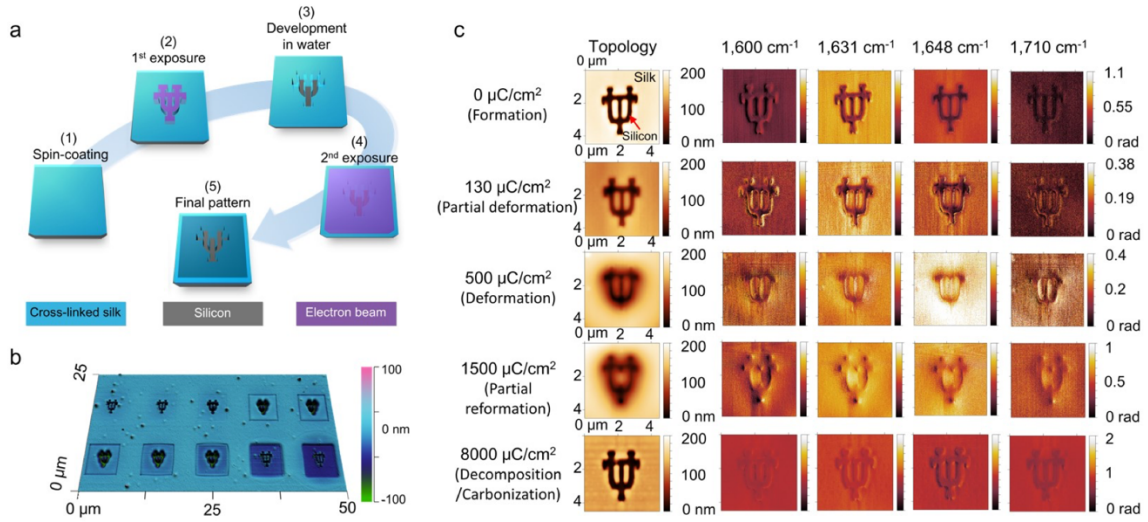

Figure 8: Direct visualization of electron-directed structural transitions of β-sheets using near-field IR nano-imaging. (a) Illustration of a two-step EBL process for sample preparation. First, an area of 3 μm × 3 μm (in the shape of a "UT" logo, line width: 200 nm) was patterned using EBL followed by a water development, which provided a clear contrast between silk and silicon and facilitated the following spectroscopic imaging/characterization. Then, a second step of electron irradiation was used to induce localized structural transitions in silk (5 μm × 5 μm squares) by delivering ebeams at various dosages. (b) AFM topographic images of silk nanopatterns fabricated using EBL at the dosages ranging from 0 to 8,000 μC/cm^2. (c) Infrared nano-imaging using s-SNOM: the phase contrast between silk and silicon (a flat spectral response in the mid-IR) in each IR image correlates to the absorption of silk proteins (i.e., the surrounding area of "UT" logos) of various structures at that wavenumber/wavelength, and the comparison of contrast differences between the IR images (for instance, those in column 3 and column 4) implies the dominant protein structure within the amide I vibration bands (e.g., 1,631 cm^{-1} for β-sheets and 1,648 cm^{-1} for random coils). (*46*)

To explore the nanoscale conformational transition of silk proteins (with emphasis on the secondary structure of β-sheets), we prepared a set of silk fibroin samples on silicon substrates fabricated by EBL, which offers the high lithographic resolution at the nanoscale. A set of thin silk films with a thickness of ~ 150 nm were spin-coated and crosslinked by methanol (i.e., the formation of β-sheets from random coils). A reference substrate (e.g., silicon or gold) with a flat IR response is typically needed in s-SNOM measurements. A two-step EBL was applied 1) to create a silicon pattern of "UT" in the first step EBL; and 2) to expose a square area with "UT" carved out, irradiated with different dosages of electrons in the second step EBL. The variation of dosage causes a gradual electron-induced conformational transition (Figure 8A). The "UT"-shaped silicon substrate served as an IR reference and facilitated both topographic characterization and more importantly IR nano-imaging. Multiple samples were prepared to elucidate the fundamental structural variations of silk samples by systematic exposures of silk samples to different dosages of electron beam radiation. Notable differences have been found in terms of the sharpness and thickness (Figure 8B) of as-fabricated silk nanostructures that underwent the radiolysis and pyrolysis processes - dominant at low and high dosages - respectively.

Figure 8C illustrates the IR nano-imaging of the formation (induced by chemical treatment using methanol (*96*)), deformation, reformation, decomposition, and carbonization (all induced by electron radiation) of β-sheet contents in silk nanostructures using s-SNOM. The first column shows the topographic images. Both sets of IR phase images - which were normalized to the silicon substrate - of silk nanostructures taken at 1,600 cm^{-1} (column 2) and 1,710 cm^{-1} (column 5) show weak contrast between silk and silicon, indicating an off-resonant response of the amide I bands. At the dosage of 0 $\mu C/cm^2$ (no electron irradiance), the phase image shows a

strong contrast at 1,631 cm^{-1} for β-sheets (column 3), which is much higher than the contrast in the image taken at 1,648 cm^{-1} for random coils (column 4, characteristic peak for amorphous silk), indicating a dominant β-sheet existence in crystalline silk. The difference in the phase contrast between images taken at 1,631 cm^{-1} and 1,648 cm^{-1} slightly decreases at the dosage of 130 μC/cm^2, indicating the partial deformation of the β-sheets (which transformed to unordered amorphous silk) in crystalline silk. When the dosage is increased to 500 μC/cm^2, the image taken at 1,648 cm^{-1} shows a noticeably higher contrast than the one taken at 1,631 cm^2, opposite to the case of 0 μC/cm^2 dosage, suggesting a typical organization of the unordered amorphous protein from a more complete deformation of β-sheets. With increasing electron beam dosage to 1,500 μC/cm^2 the phase images taken at 1,631 cm^{-1} show a marginally higher (but comparable) contrast to 1,648 cm^{-1}, which is believed to be due to a partial reformation of β-sheets from unordered silk polypeptides (i.e., re-crystallizing). Partial recrystallization has been observed in previously reported work using chemical (*97*) or thermal treatments (*98, 99*).

At the dosage of 8,000 μC/cm^2, no substantial contrast was found in the phase images at the four frequencies. This is attributed to the decomposition of β-sheets along with a partial formation of carbonaceous pyroprotein after excessive electron irradiance treatment of β-sheet nanostructures, as indicated by the increased infrared reflectivity of a more developed carbon structure at higher dosages. These results are similar to the previously reported macroscale carbonization of β-sheet-rich silk protein by heat (*100, 101*). This finding offers a potential method for direct formation of nanopatterned carbon structures using polymer based materials (*102*) by controlling the protein thickness and electron beam dosage, although this is not the main focus of this report.

QUANTITATIVE MEASUREMENT OF THE SILK CONFORMATION TRANSITION UNDER THE ELECTRON BOMBARDMENT USING SNOM

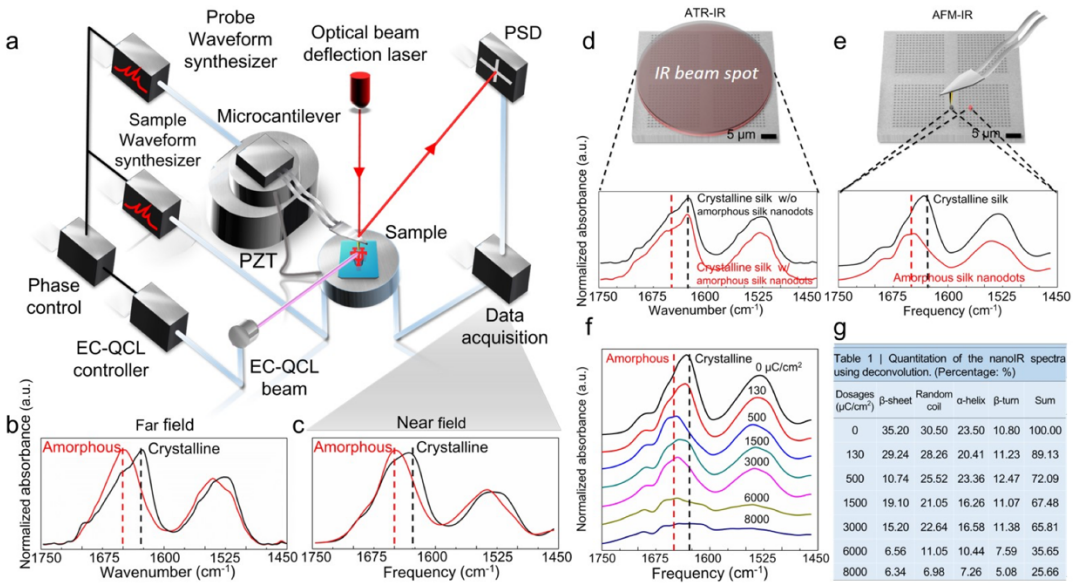

Table 1 | Quantitation of the nanoIR spectra using deconvolution. (Percentage: %)

Dosages (μC/cm²)	β-sheet	Random coil	α-helix	β-turn	Sum
0	35.20	30.50	23.50	10.80	100.00
130	29.24	28.26	20.41	11.23	89.13
500	10.74	25.52	23.36	12.47	72.09
1500	19.10	21.05	16.26	11.07	67.48
3000	15.20	22.64	16.58	11.38	65.81
6000	6.56	11.05	10.44	7.59	35.65
8000	6.34	6.98	7.26	5.08	25.66

Figure 9: Quantitative evaluation of conformational transitions in silk proteins using near-field IR nano-spectroscopy. (a) Schematics of IR nano-spectroscopy using AFM-IR: pulses of infrared radiation emitted by an IR QCL (output range: 1,460 cm^{-1} – 1,780 cm^{-1}, swept by a step size: 1 cm^{-1}) were used to illuminate the sample, causing a rapid thermal expansion of silk nanostructures due to local absorption enhancement at various stages picked by the AFM tip, corresponding to the absorption spectroscopic signatures. (b) & (c) The AFM-IR spectra on amorphous and crystalline silk thin films are consistent with the conventional bulk FTIR spectra. (d) & (e) Spectra of a crystalline silk thin film with embedded amorphous silk nanopatterns of ~ 30 nm fabricated using EBL, characterized by ATR-IR and AFM-IR, respectively. AFM-IR offers a considerable advancement (~ 1000 × improvement spatially) in distinguishing nanoscale structural heterogeneity. (f) AFM-IR spectra of electron-induced structural transitions in silk proteins. (g) Quantitation of the nanoIR spectra using deconvolution. The mass sum continuously decreases mainly due to bombarding effects and thermal degradation of proteins in high energy EBL. (*46*)

To quantitatively confirm the conformational transition and acquire unambiguous structural identification of each stage, we performed an IR nano-spectroscopy study of the electron-induced structural transitions of silk proteins using AFM-IR with a spatial

resolution of ~ 20 nm (Anasys Instruments, USA). Infrared pulses emitted by an IR QCL (Daylight Solutions Inc., USA; output range: 1,460 – 1,780 cm^{-1}, swept by a step size of 1 cm^{-1}) were used as the near-field source to illuminate the sample, causing a rapid thermal expansion of silk nanostructures corresponding to the absorption fingerprints (Figure 9A). The AFM-IR spectra on amorphous and crystalline silk thin films are consistent with the conventional bulk FTIR spectra (Figure 9B – 9C). However, AFM-IR offers an important advancement (~ 1000 × improvement in the spatial resolution) as compared with previously reported work using conventional infrared techniques which average the structural information over relatively large areas (i.e., a few microns to a few dozen microns using FTIR-microscopy) on silk materials with high structural heterogeneity at the nanoscale (Figure 9D – 9E). Crystalline silk shows a maximum absorption at ~ 1,625 cm^{-1} (β-sheets) with two shoulder peaks at ~ 1,645 cm^{-1} (random coils) and ~ 1,660 cm^{-1} (α-helices), in good agreement with the frequency ranges corresponding to vibrational bands in β-sheet-rich B. mori silk within the amide I region of the spectrum (*93*). Note that the resonance peak may differ within 10 cm^{-1} in s-SNOM and AFM-IR, as has been previously observed in s-SNOM spectra when compared to far-field IR and thermal-expansion-based AFM-IR spectroscopies as a result of tip-sample coupling (*80*) and the spectral phase approximation (*82*).

As shown in Figure 9F, the characteristic peak intensity of the β-sheet formation at ~ 1,625 cm^{-1} decreased as the dosage increases from 0 to 500 $\mu C/cm^2$, indicating the continuing deformation of the β-sheet content and a slight increase of α-helix regions. After increasing the dosage to 1,500 $\mu C/cm^2$, a resurgence of the absorption intensity correlated to the β-sheet formation at ~ 1,625 cm^{-1} was present, which was noticeably lower than the original peak in crystalline silk, indicating partial reformation of β-sheets. The AFM-IR spectra of silk nanostructures under excessive electron dosage

reveal that the characteristic peaks for β-sheet crystal structure were gradually weakened and broadened as the dosage increased from 1,500 to 6,000 μC/cm^2 and disappeared following an electron irradiance at 8,000 μC/cm^2, indicating that the β-sheet crystals were progressively decomposed and carbonized at high dosages. The changes in the characteristic peaks of the silk proteins indicates a more significant decrease in the fraction of amorphous regions relative to the β-sheet regions. A detailed deconvolution of the amide I band was conducted and the secondary structure content of each stage was quantified (Figure 9G). Additionally, we observed a noticeable difference in the structural integrity of silk proteins after electron irradiation. The crystalline and decomposed (partially carbonized) silks show considerably better pattern fidelity (namely higher sharpness, column one in Figure 9C), which we hypothesize to be partially due to their highly ordered structures and applicable stray exposure (i.e., proximity effect) caused by the backscattered electrons through the exposed silicon substrate.

THE COMPARISON OF THE ELECTRON-SILK INTERACTION BETWEEN THE AMORPHOUS AND CRYSTALLINE FILMS

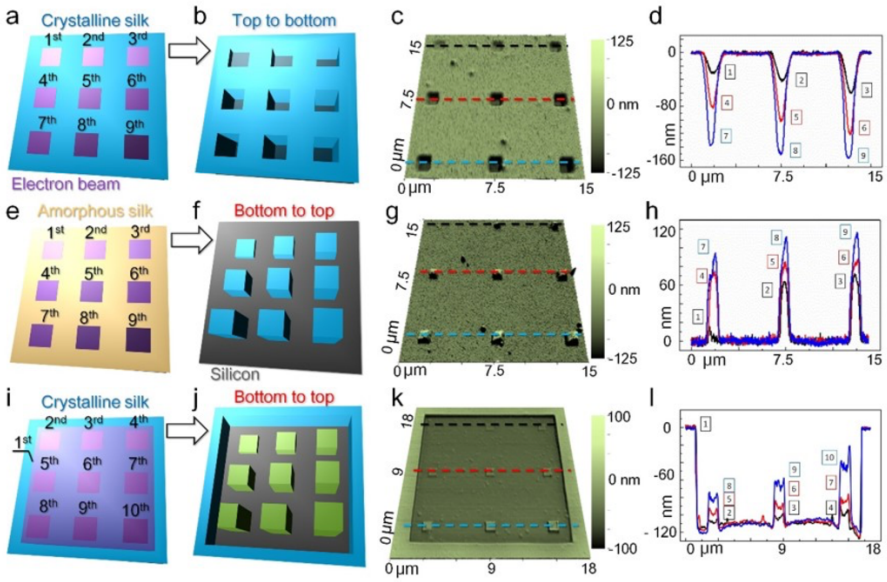

Figure 10: Comparison of electron-structure interactions in amorphous and crystalline silk proteins. (a) – (l) Three sets of silk nanostructures have been made in positive (row 1, nanosculpturing) and negative (row 2 and row 3, nanosintering) tones using EBL at various dosages. The lineouts (column 4) correspond to the dashed lines in AFM topographic images (column 3). A pre-exposure was applied to deform/de-crosslink β-sheets (to random coils) in crystalline silk (row 3), which can be further re-crosslinked to form negative nanostructures, similar to those generated by the process starting with the amorphous silk (row 2) (*46*).

The ability to structurally characterize the material allows us to conduct a comprehensive evaluation of silk proteins for 3D nanostructuring. We found that there is a significant difference in the kinetics of protein-electron interactions between amorphous silk (random coil dominated) and crystalline silk (β-sheet dominated) (Figure 10). In this report, we demonstrate making of 3D silk nanostructures by in situ altering conformational structures of proteins using EBL with two different but complementary methods, namely electron-nanosculpturing (a subtractive manufacturing process, Figure 10A – 10D) and electron-nanosintering (an additive manufacturing

process, Figure 10E – 10H). Note that crystalline silk can be also used in electron-nanosintering but an initial EBL exposure for β-sheet deformation is needed (Figure 10I – 10L).

As revealed by near-field IR imaging and nano-spectroscopy, the interaction between the electron beam and the silk structure critically depends on the structural conformation on the protein matrix and as-applied electron dosage. For crystalline silk exposed to the electron beam, scission of the crosslinked β-sheets tends to occur from top to bottom, resulting in the removal of materials after a water-based development, which is referred to as electron-nanosculpturing. In contrast, for the amorphous silk exposed to the electron beam, crosslinking of unordered random coils (either intrinsic or deformed from crystalline proteins upon electron irradiations) proceeds from bottom to top, which is referred to as electron-nanosintering. The ability to understand basic mechanisms of electron-induced structural transformations allows us to produce sophisticated nanotopographies and nanostructures, opening up numerous opportunities including biomimetic nanosurfaces and tissue engineering applications.

THE 3D STRUCTURES CREATED BY NANO-SINTERING AND NANO-SCULPTURING

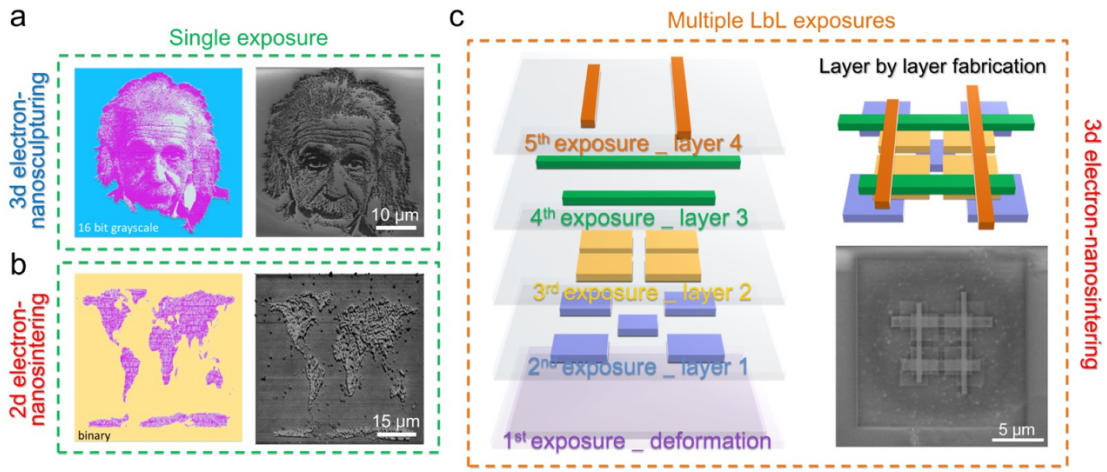

Figure 11: 2d and 3d nanostructuring of silk proteins. (a) 3d electron-nanosculpturing: 3d nanotopographies on crystalline silk can be created using a 16-bit grayscale positive EBL (left: design image; right: SEM image). One grayscale exposure was applied, followed by a water-only development to remove the exposed area. (b) 2d electron-nanosintering: 2d nanotopographies on amorpous silk proteins can be created using a binary negative EBL (left: design image; right: SEM image). One exposure was applied to crosslink the exposed area. Unexposed area is removed after water development. (c) 3d electron-nanosintering: 3d nanostructures on crystalline silk can be created using a layer-by-layer (LbL) multi-EBL. (Inset: left) Multiple exposures are applied in sequence to define each layer. (Inset: right) Schematic and SEM images of as-designed 3d silk nanostructures using LbL nanosintering process. The 1st exposure is to de-crosslink the crystalline silk proteins, resulting in amorphous proteins to be sintered/re-crosslinked by the following LbL EBL steps. For amorphous silk, this step (the 1st exposure) is unnecessary (*46*).

Several examples were fabricated as the first proof-of-principle demonstrations (Figure 11). While the results express some resemblance to those by multi-photon polymerization (MPP) technique, our methods differ in two important aspects. Firstly, our fabrication is not limited by the optical diffraction (~ 100 nm in advanced MPPs, estimated by Abbe's equation) but by the electron diffraction (< 10 nm in standard EBLs, estimated by the de Broglie equation), offering significant improvements in achievable

structuring resolutions. Secondly, photo initiators were required to enhance MPP in silk fibroin proteins while our techniques deal with pure regenerated silk in an all-water-based process, better preserving the biocompatibility of the material. Low throughput has been the fundamental limit of EBL despites of its unparalleled lithographic resolution. For example, it took ~ 5 minutes and 10 minutes to fabricate the grayscale Einstein image (~ 35um x 35um) and the LbL multilayer structure (~ 16um x 16um) shown in Figure 11, respectively. Nevertheless, nanoprobing of electron-beam induced protein structural transitions using near-field spectroscopic imaging techniques reported in this work can be readily extended to study conformational dynamics of a variety of proteins (e.g., keratins, collagens and spider silk proteins) using other conventional nanofabrication systems/sources (e.g., ion beams and photons).

This comprehensive investigation of the electron-beam induced conformal modification of silk at the nanoscale using infrared near-field optics allows the characterization and understanding the interaction between the silk protein and electron irradiations. A deep understanding of the structure-property relation in protein-based biomaterials unveils an exciting route for high-level protein-based 3D nanofabrication and engineering, opening up possibilities for a new set of biomaterials with performance and function unattainable with other materials. This work has been published in the Nature Communications.

Chapter 4: The silk conformational transitions regulated by ions

INTRODUCTION ON SILK BASED IBL MANUFACTURING

Besides EBL, another commonly used technique in the semiconductor manufacturing – ion beam lithography (IBL) is evaluated on its compatibility with silk based platform. Numerous research efforts have been invested in the precise placement of biological components and the controlled construction of functional bionanostructures, which opens up significant opportunities in applications from biointerfaces (*103*), biosensing (*104*), tissue engineering (*105*), to regenerative medicine (*106*). The difficulty is mainly exerted by the fundamental challenge of harmonizing the existing integrated circuits (IC)-oriented nanofabrication technologies with biological systems which requires alleviating the inherent mismatch between biological (soft-wet) and non-biological (hard-dry) components. However, since most biological molecules are fragile and only functional in aqueous environments, there are severe constraints on the integration of biomolecules into conventional fabrication technologies which are usually optimized for inorganic compounds. Meanwhile, biomedical applications dictate precise reconstructions of the complex biological microenvironment with demanding requirement of the 3D geometries and nanometer sized features. Innovations in both materials and manufacturing techniques have yet to be explored.

Here, we report precise 2D and 3D nanostructuring on genetically engineered spider silk using IBL to create well-defined nanostructures for: 1) enhanced fluorescence enabled by dye-embedded plasmonic protein nanostructures and 2) controlled cell seeding and inhibition guided by patterned protein substrates as proof-of-concept applications. The reduced scattering of ion beams in the resist material enables better pattern precision compared with that of EBL and the added control over protein

sequences and molecular weights of genetically engineered spider silk provides unprecedented lithographic resolution, sharpness and biological functions compared to the natural proteins. Moreover, we report a creative strategy of building arbitrary grayscale (2.5D) and 3D bionanoarchitectures (using IEBL) containing well-defined protein units serving as the building blocks with both shape and function on demand – termed "Protein Bricks". The fine control of nanostructuring – namely, protein brick manufacturing and assembly – is obtained by accurately directing ion and electron beam irradiations onto the protein matrix to vary its solubility in water. Structures with high aspect ratio can be easily created while no hazardous chemicals (e.g., photoinitiators, organic solvents) are used or generated. The assembly is realized by IEBL in a programmable sequence with precise alignment. This approach provides a facile method for patterning and immobilizing biomolecules within nanoscopic, hierarchical protein structures that could serve as the building blocks for functional nanocomponents and nanodevices.

NANOSTRUCTURING OF GENETICALLY ENGINEERED SPIDER SILK USING IBL

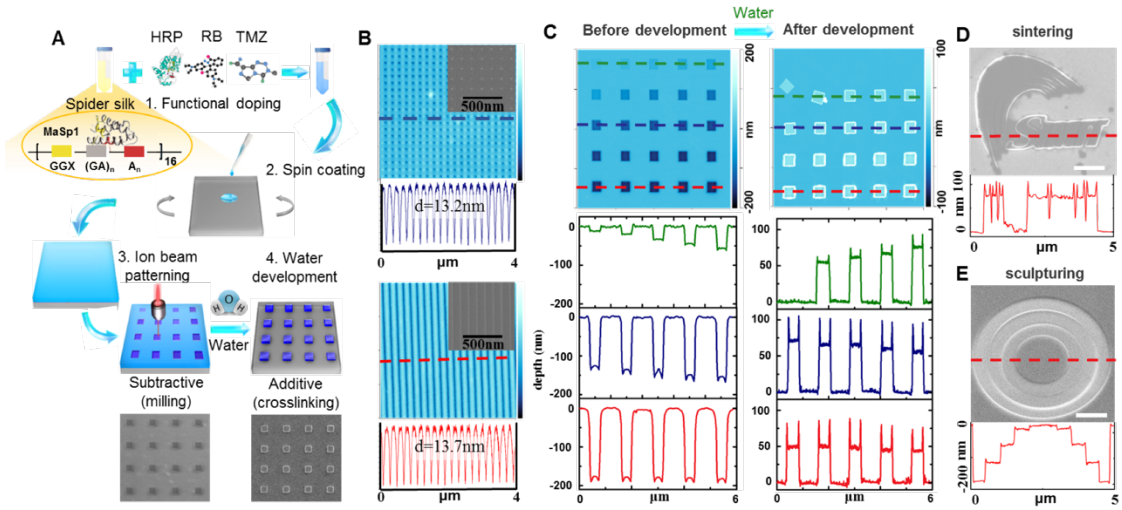

Figure 12: The functionalized 2D and grayscale structures fabricated with IBL using genetically engineered spider silk. (A) The schematic process of bionanomanufacturing using IBL and genetically engineered spider silk proteins. The spider silk can be functionalized via simple mixing and spin coated into thin films. The IBL writing can define two complementary types of nanostructures simultaneously, namely, nano-sculpturing (subtractive by etching), nano-sintering (additive by crosslinking). The SEM images of the nanoholes and nanopillars are shown below the schematics. (B) Dot and line arrays fabricated using IBL on 30 nm thick spider silk film with a minimum feature size of 13.2 nm and 13.7 nm respectively. (C) The AFM images (left) of nano patterns (before and after development in water) fabricated by nano-sculpturing and nano-sintering under different ion beam dosages ranging from 10 to 1500 $\mu C/cm^2$ and the topological profiles corresponding to the dotted line on the top. (D, E) The SEM images of 2D (D) and grayscale (E) patterns fabricated by IBL with the cross-section profiles on the bottom. The scale bar is 1 μm.

In this work, a new bionanomanufacturing paradigm is proposed for defining both 2D and 3D protein nanostructures with both geometries and functions on demand. The proposed process is schematically shown in Figure 12A. Synthetic spider silk protein is designed and expressed in Escherichia coli through genetic engineering (Please see Method Section). The purified recombinant silk solution can be functionalized with a

variety of chemical and biological dopants such as fluorescent dyes, enzymes, and antibodies through a simple mixing process. The pure/functionalized spider silk solution is then spin coated into thin films with thickness ranging from dozens of nanometers to several micrometers by adjusting the solution concentration and spinning speed. To define the nanoscale structures on the spider silk film, an IBL writing tool (strata FIB 201, FEI Co., USA) is used for nanometer-precision patterning. Dot and line arrays fabricated using IBL on 30 nm thick spider silk film with minimum feature sizes of 13.2 nm and 13.7 nm respectively are successfully demonstrated (Figure 12B), approaching the molecular limits of the as-used recombinant spider silk protein of ~10 nm. The ion irradiation has two effects on the spider silk. First, high energy ions can etch off the spider silk, similar to what has been commonly observed in other materials (*107*). Meanwhile, the ions that penetrate into the film can induce structural transitions (crosslinking) in the spider silk from an amorphous state (soluble in water) to a more ordered β-sheet state (insoluble in water). The etching effect requires more energy than that for crosslinking and happens only at the surface of the film; while the crosslinked structures can form underneath the areas that are etched off by ions. Therefore, two complementary types of structures can be fabricated by a single step of IBL writing as shown in Figure 12C. The ion irradiation can etch the film according to the pre-designed nanoscale patterns in a subtractive fashion (referred to as nano-sculpturing in this work) with increasing depth as the irradiation dosage increases from 10 $\mu C/cm^2$ to 1500 $\mu C/cm^2$. Simultaneously, the complementary nanoscale patterns are formed underneath the etched patterns and built additively with increasing height caused by more ion irradiation (referred to as nano-sintering in this work). As a result of the way that the nano-sintered patterns are formed, the structure can only survive the water development step and be left on the substrate when the ion irradiation dosage is above a threshold value (related to the

thickness of the film). This is experimentally confirmed as shown in Figure 12C where the top row of a nano-sintered pattern (with low irradiation dosage) is blank. As the ion irradiation dosage increases, the nano-sintered patterns will be formed further down and closer to the bottom, at which point the patterns remain after water development, but move away from the designed location due to the lack of strong anchorage on the substrate. When the irradiation dosage is sufficiently high, the patterns stay on the substrate as expected.

To further exploit the characteristics of this fabrication paradigm, a 2D "SIMIT" logo and a grayscale (in terms of the height of the structure, or 2.5D) concentric ring nanostructure are fabricated by nano-sculpturing and nano-sintering respectively as presented in Figure 12D & 12E. As a more explicit manifestation of the quality and the grayscale nature of the nanostructures, the topological profile of both structures are shown below the SEM image. The as-fabricated structures display a relatively smooth surface and vertical side walls. In addition, the minimum dosage to fabricate patterns on a 215 nm thick spider silk film at 30 keV is found to be 100 $\mu C/cm^2$ — approximately 1/20 of the dosage needed to fabricate comparable structures with EBL (25 keV), thus allowing high yield manufacturing.

NANOSCOPIC ANALYSIS OF SPIDER SILK UNDER ION BEAM IRRADIATION USING SNOM

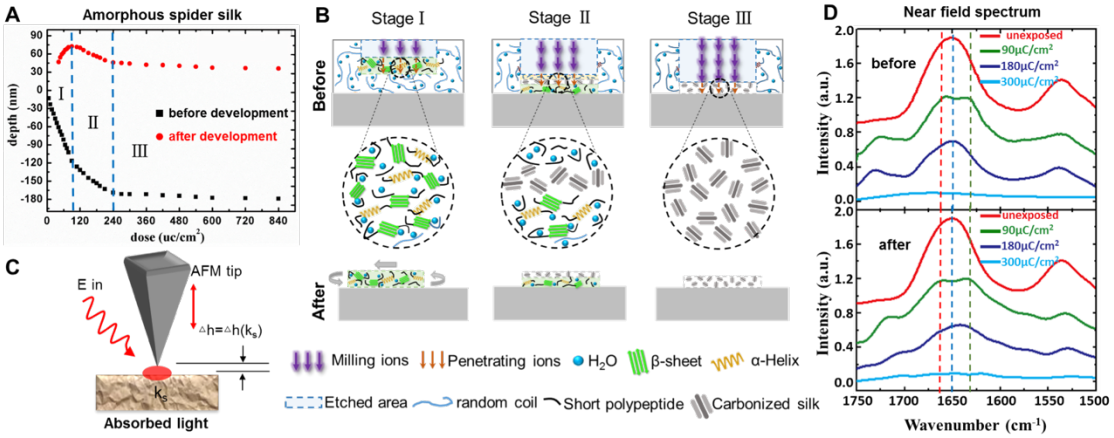

Figure 13: The nanoscale analysis of conformational transition of spider silk proteins under increasing ion irradiation dosages. (A) The etching depth (black squares) and pattern height (red dots) of nano protein structures with changing ion beam dosages show three distinct stages, indicating conformational and property changes at the three stages. (B) The postulated mechanism of conformational transitions of the three different stages. For Stage I, the low ion beam dosage can crosslink the amorphous spider silk to crystalline state, but the formed structure cannot reach the bottom of the film and firmly anchor the substrate. Therefore, the patterns can shift, rotate, and deviate from the original patterning position after water developing. For Stage II, the ions can reach the bottom of the spider silk film, etch the crosslinked patterns, and break crosslinked structures to small peptide on the top surfaces of the fabricated patterns. For Stage III, when the dosage is large enough, the structure can be totally carbonized. (C) Schematics of nanoscale IR spectroscopic spectrum using AFM-IR. The thermal expansion due to absorption of IR light is used to map absorption spectrum of the spider silk. (D) The IR near filed spectra of patterns before and after development upon different ion beam irradiation of 90, 180, and 360 μC/cm^2. The characteristic peaks are 1631 cm^{-1} (β-sheet, green dash), 1650 cm^{-1} (random-coil, blue dash), and 1662 cm^{-1} (α-helix, red dash), respectively. The curves show that with low ion beam dosage, the amorphous spider silk is crosslinked into more ordered state (α-helix and β-sheet). As the dosage increases, the crosslinked spider silk is broken down into short peptides marked by the decrease in the characteristic absorption of β-sheet structure. Higher dosages of ion beam irradiation will carbonize the protein.

To explore the nanoscale conformational transitions of spider silk proteins, we prepare a set of spider silk samples on silicon substrates using IBL, which offers nanoscale lithographic resolution. By exposing the spider silk film with dosages ranging from 10~840 $\mu C/cm^2$, three significantly different stages with different etching rate were observed before and after development (Figure 13A). With increasing dosages, the slope (plotted as etching depth against ion irradiation dosage, which is correlated with either the etching speed in the nano-sculpturing or the structure formation speed in the nano-sintering) of the three stages changes, indicating that the component as well as the properties of the material are changing. The pattern depth of the undeveloped film shows the ion etching effect, whose speed is inversely proportional to the density of the material. Therefore, as the ion irradiation dosage increases, the density of the exposed spider silk also increases at three different stages, indicating the existence of conformational transitions. On the other hand, the height of patterns after development (red curve) also shows three stages as the ion irradiation dosage increases. For Stage I, the height of the patterned structures increases with ion dosage as the structure starts to form. However, Stage II and III show the opposite behavior, where higher dosages result in lower structure height, which can be associated with the etching effect from higher ion irradiation dosage. The interaction between ions and spider silk with different film thickness was also investigated.

We postulate the molecular structures of the patterned spider silk as well as the etching/crystallization mechanism occurring in three different phases. Figure 13B is the schematic of the proposed spider silk fibroin conformational transitions induced by IBL with different ion irradiation dosages. The low dosages (Stage I) can crosslink the random coil to α-helix and β-sheet, making it water-insoluble. The subsequent 'water development' results in dissolution of the amorphous silk, leaving the exposed area on

the substrate, which forms nanoscale pillars. However, the beam dosage is not large enough to crosslink the patterns to the bottom, and thus, after water developing, the patterns can shift, rotate, and deviate from the original processing position. For a medium ion beam dosage (Stage II), with an increase of ion beam dosage, the etching depth increases as well, allowing the designed patterns to reach the bottom of the spider silk film. The crystalline silk can be partially decrosslinked further to short polypeptides or even etched off with extra ion beam exposure. The spider silk protein can be burned (carbonized) at higher ion beam dosage (Stage III) and completely loses its structure, resembling previously reported work (*100*).

The mechanism of the structural transitions of spider silk proteins upon ion beam irradiation is studied by a comprehensive investigation of the ion beam-induced modification of silk at the nanoscale using non-destructive AFM-IR optical microscope (Anasys Instruments, USA). The simplified schematics of nanoscale IR spectroscopy using AFM-IR are shown in Figure 13C. Localized thermal expansion due to the absorption of IR light is detected by a contact mode AFM tip, and the spectrum of the materials can be mapped by sweeping the wavelengths of the incident IR laser (Daylight Solutions, USA). The behavior of spider silk protein is verified by analyzing the transition between amorphous and ion-beam-modified spider silk fibroin with an ion beam dosage of 90 $\mu C/cm^2$, 180 $\mu C/cm^2$, or 300 $\mu C/cm^2$, corresponding to the three stages, respectively (shown in Figure 13D). The spectrum of amorphous spider silk (red line) shows an absorption peak centered at 1650 cm^{-1}, representing the typical random coil structures in the amorphous protein. The spectrum of spider silk exposed to IBL of 90 $\mu C/cm^2$ (Stage I, green line) shows two peaks at 1662 cm^{-1} and 1631 cm^{-1}, typical of the α-helix and β-sheet conformation of the spider silk protein, respectively. Compared to amorphous spider silk, the proportion of random-coil is decreased, and the

α-helix and β-sheet content is increased, indicating the random-coil component can be crosslinked to crystalline structures through the irradiation of ion beam. For 180 μC/cm^2 (Stage II, purple line), the proportion of random coil increases again, which means the crystalline structures can be de-crosslinked with extra ions interaction. For 360 μC/cm^2 (Stage III, blue line), the characteristic peaks of the proteins gradually vanish, indicating that most of the protein structures are carbonized with large dosage. Meanwhile, we collected near field images at 1631 cm^{-1} (the typical β-sheet absorption peak) for the three stages.

FABRICATION CHARACTERISTICS OF IBL ON SPIDER SILK

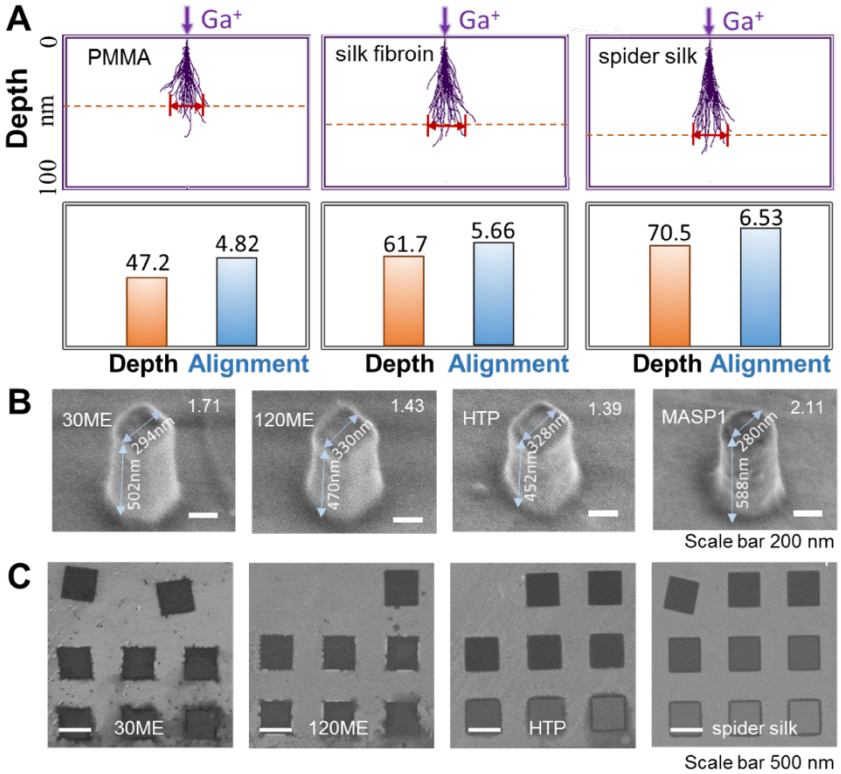

Figure 14: The comparisons between different materials (silk fibroin processed under different conditions and genetically engineered spider silk) as IBL resist in terms of ion scattering, structure aspect ratio, fabrication sensitivity and fabrication contrast. (A) The ion distribution in different materials (PMMA, silk, and spider silk). The top row shows the simulated trajectories of ions in different materials. The dashed line represents the penetration depth of ions. And the bottom row is the calculated depth and alignment of ion propagation in different materials. The alignment is defined as depth/straggle. (B) The comparison between different materials in terms of maximum structure aspect ratio. (C) The SEM images of different fibroin fabricated using IBL with change of dosage to compare the fabrication sensitivity and contrast. The patterns on the top row are drifted because the ion irradiation dosages are not high enough to crosslink the fibroin protein at the bottom. Therefore, those patterns are not anchored well on the substrate.

Compared with electrons, ions are much heavier, and can maintain better propagating direction due to the smaller scattering rate inside the materials. Therefore, in

order to understand the fabrication characteristics of IBL using genetically engineered spider silk, the ion scattering in three materials – namely polymethyl methacrylate (PMMA), silk fibroin, and genetically engineered spider silk - were simulated by The Stopping and Range of Ions in Matter (SRIM, SRIM Co. USA) software (Figure 14A). Trajectories of the Ga+ ions in the three materials are obtained by setting the density and the molecular formula of the materials, and the statistics of penetration depth as well as alignment (defined as depth/straggle) are then calculated from the simulation. The simulation and the statistics show that the genetically engineered spider silk (with a penetration depth of 70.5 nm and alignment of 6.53 nm/nm) has a longer penetration depth and better alignment than both the silk fibroin (with a penetration depth of 61.7 nm and alignment of 5.66 nm/nm) and the PMMA (with a penetration depth of 47.2 nm and alignment of 4.82 nm/nm). This can be attributed to the fact that genetically engineered spider silk protein has a smaller and more uniform molecular weight and density than PMMA and silk fibroin protein.

Another important benchmark in evaluating the nanofabrication technique is the maximum aspect ratio of the fabricated nanostructures - one of the factors that limit the complexity of the nanostructures. Benefitted from the high alignment, the structures fabricated using IBL generally have high aspect ratio. Therefore, we study the aspect ratios of the fabricated nanostructures using silk fibroin protein extracted for 30 min (30 ME silk) and 120 min (120 ME silk), silk fibroin extracted under 121°C temperature and 1.2 kPa pressure (HTP silk), and Major Ampullate Spideroins 1 (MaSp1) as shown in Figure 14B. The 30 ME silk fibroin displays an aspect ratio of 1.71, which is better than the 120 ME (1.43) and HTP (1.39) silk. This is due to the fact the 30 ME silk has the longest average protein chain length and therefore better mechanical properties to sustain structures with high aspect ratio. On the other hand, the MaSp1 spider silk exhibits

structures with a superior aspect ratio (2.11) to the 30 ME silk, indicating even better mechanical strength.

In addition, a series of nanostructures with increasing dosages from 30 $\mu C/cm^2$ to 1500 $\mu C/cm^2$ are fabricated according to the nano-sintering process using the same set of materials (i.e. 30 ME silk, 120 ME silk, HTP silk, and MaSp1 spider silk) to evaluate their IBL sensitivity and sharpness (Figure 14C). The smallest dosage at which the fabricated structure can stay on the substrate is correlated with the sensitivity of the material while pattern sharpness indicates the contrast. The patterns fabricated using spider silk show the best completeness, which suggests that the structures can reach the bottom of the substrate with smaller ion irradiation dosages compared with the silk fibroin based material and thus have higher IBL sensitivity. These properties can be mainly attributed to the lower density and shorter chain length of the spider silk since the ions can penetrate and crosslink the film easier. In addition, because of the well-defined and uniformly distributed molecular weight, the spider silk exhibits the best pattern sharpness as shown in Figure 14C.

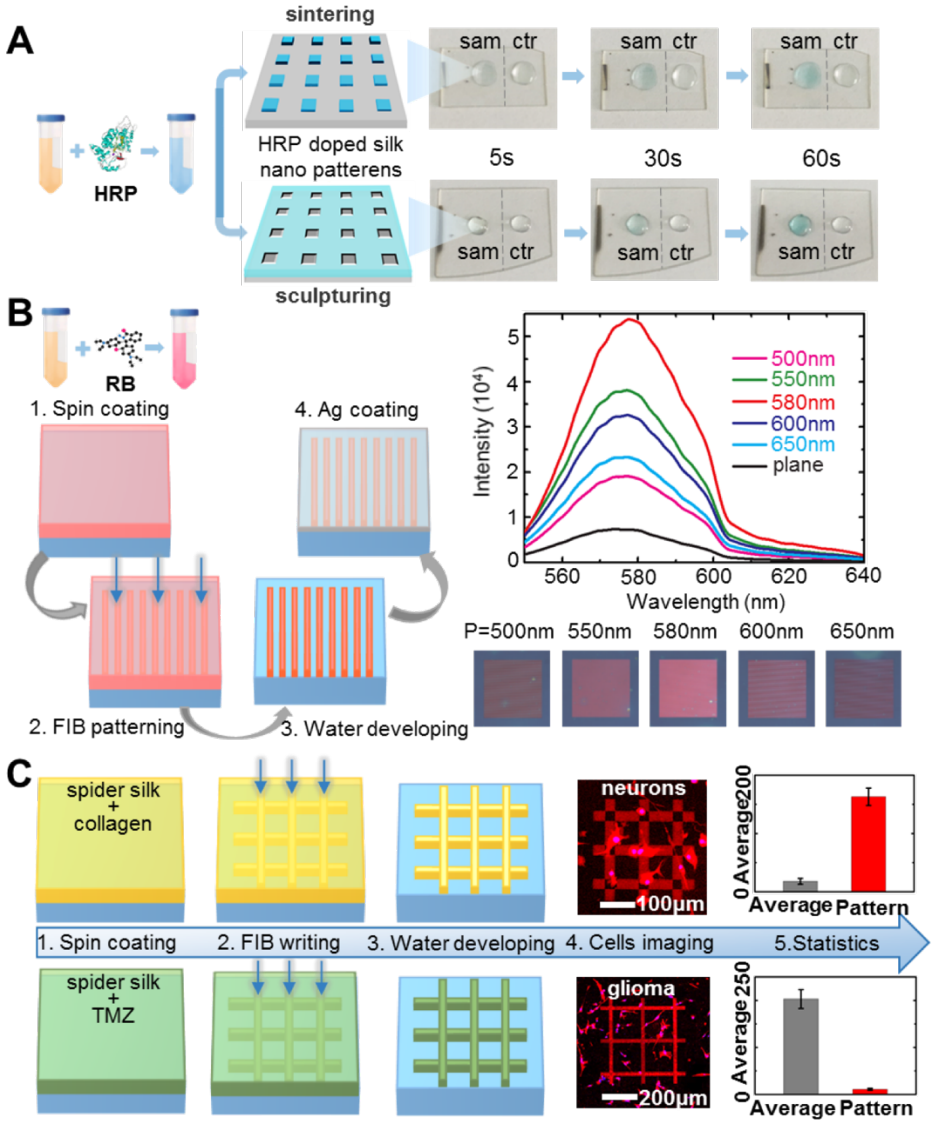

Figure 15: The application of genetically engineered spider silk fabricated by IBL with different dopants. (A) Assessment of enzyme activity of HRP doped spider silk after nanopatterning for both nano-sintered (the top row) and nano-sculptured (the bottom row) structures. The HRP doped spider silk is spin-coated on silica for IBL nanofabrication. The left part (SAM) is the spider silk patterned on silica, and the right part (CTR) is the control case of bare silica substrate. By adding tetramethylbenzidine (TMB) solution on both sides, a chromogenic reaction is observed on the left, indicating preservation of bio-activity of the enzyme in spider silk matrix even after ion irradiation. (B) The fluorescent molecules (e.g., RB) doped spider silk protein is

fabricated using IBL into optical grating structure. The deposited layer of Ag onto the optical grating can enhance the fluorescence significantly due to surface plasmon effects. The fluorescent spectra and microscope images of plane surface and nano structures with different periods are shown on the right. (C) The schematic of collagen/TMZ doped spider silk fabricated by IBL. The protein structure can guide the proliferation of neural cells as well as inhibit the growth of cancer cells. The cells imaging and statistics are presented on the right to show the quantitative data.

One of the main advantages of using spider silk is its ease of functionalization through simple mixing with organic and inorganic dopants in the water-based solution, bringing function to programmable nanoscale forms. In addition to being used as the hosting matrix, the spider silk can preserve the activities of the dopants such as enzymes and antibodies. As a proof-of-principle demonstration of the genetically engineered spider silk doped with biologically functional molecules, horseradish Peroxidase (HRP) is mixed into the spider silk matrix (Figure 15A). The doped spider silk is then spin coated on silica substrates for better color observation. Two sets of samples are prepared where half of each substrate is washed to remove the spider silk for use as control groups (marked "ctr"). The areas with spider silk left (marked "sam") are then patterned with a simple square matrix using nano-sintering and nano-sculpturing techniques respectively. With the addition of 3,3',5,5'-Tetramethylbenzidine (TMB) droplets, a color change can be observed if the TMB reacts with active HRP. The HRP doped spider silk samples can well maintain the activity of the dopant even after Ga+ ion irradiation (Figure 15A).

The doped spider silk can also be fabricated into structures that achieve shape-enabled functions. As a demonstration of this concept, the genetically engineered spider silk is doped with fluorescent dye that emits light at a center wavelength of 580 nm (Figure 15B). The doped spider silk is then fabricated into optical gratings. With an additional thin layer of silver (Ag) deposited on top, the fluorescent light can be enhanced due to surface plasmon effects. Spectra of samples prepared with different grating periods

ranging from 500 nm to 650 nm are collected using a microphotoluminescence (μ -PL) spectroscopy (Carl Zeiss A1, Germany) with an excitation wavelength of λ = 532 nm. As shown in Fig. 4B, the fluorescent intensity can be clearly enhanced (~9 fold) with the grating structure, where the best enhancement is achieved with a grating periodicity of 580 nm, matching the emission spectrum of the fluorescent dye. This proves the applicability of the structure assisted functional spider silk as a platform for enhancing the functions of its dopants.

Furthermore, the biocompatibility of the spider silk enables cellular level functions such as guided cell seeding and inhibition by doping with bio-active materials. Two examples are demonstrated in Fig. 14C. A mesh structure is fabricated using the nano-sintering protocol on a spider silk film mixed with collagen, which promotes cell adhesion, and neuronal cells/glioma cells are then cultured on the substrate by following the protocol described in the Material and Method section. As illustrated in Figure 15C, the neuronal cells grow closely according to the fabricated patterns. The cells that proliferate along the patterned area are counted against the pattern-void area respectively (with a ratio of 169:16), quantitatively justifying that the fabrication paradigm can be used for devices that achieve cellular level functions. Alternatively, a similar mesh structure is patterned using spider silk doped with Temozolomide (TMZ), which is an alkylating agent used as a treatment of brain cancers. The activity of the TMZ in the fabricated mesh structures is verified by culturing cancer cells on the substrate. The fluorescence image in Figure 15 C shows that few cancer cells can live on the pattern area, and therefore proves the inhibition function of the TMZ doped in the spider silk matrix. A ratio of 7:201 is also obtained by counting the cancer cells on and away from the patterned area to quantitatively show the effectiveness of the doped TMZ.

To take advantage of the fabrication and doping flexibility, we report on a strategy of constructing protein-based nanoarchitectures with both shape and function on demand using genetically engineered spider silk as the building material as well as the hosting matrix for labile biological molecules. Furthermore, a deep understanding of the effects of electron and ion irradiation in protein-based biomaterials unveils an exciting route for high-level protein-based 3D nanofabrication and engineering, opening up possibilities for a new set of biomaterials with performance and function unattainable with other materials. In this work, we used IEBL to manufacture a variety of complex 3D functional nanostructures which are difficult to make otherwise.

3D NANO-ARCHITECTURES USING PROTEIN LEGO AS THE BUILDING BLOCK

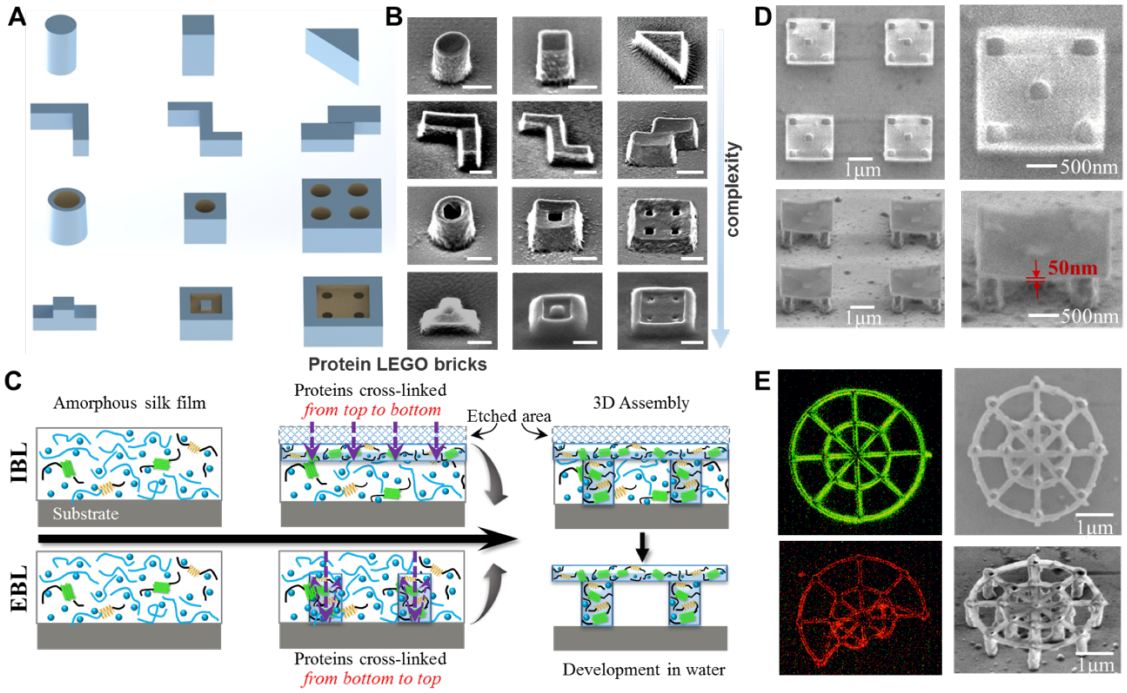

Figure 16: The 3D nanofabrication results of nanoscale Protein LEGO using IEBL. (A) The sketches of designed and (B) the SEM images of fabricated nano Protein LEGO blocks with increasing geometry complexity. The scale bar is 500 nm. (C) The fabrication strategy of fabricating 3D nanostructures (e.g., nano desks and nano webs) with IEBL. (D) The SEM images of 3D nano Protein LEGO (nano desk). (E) The fluorescent and SEM images of 3D nano functional Protein LEGO (nano net) via IEBL on fluorescein sodium (green) doped and RB (red) doped spider silk. For the RB doped spider web, two of the anchoring point was intentionally neglected such that the unsupported part can fold during the water development, showing the 3D nature of the fabricated structure.

Borrowing the concept from one of the most popular toys – "LEGO" (where large architectures can be constructed using basic blocks with different geometries), we designed a set of basic LEGO blocks with increasing geometric complexity, which can be assembled to make composite shapes. Simple geometries (first row), planar combinations of simple geometries (second row), geometries with both nano-sintered and nano-sculptured structures (third row), and geometries with two nano-sintering and nano-sculpturing levels are sketched (Figure 16A) and fabricated (Figure 16B) by IEBL. Figure 16C is the schematic of a two-step lithography process used to precisely fabricate a miniaturized spider silk nano-desk consisting of nanoscale Protein LEGO blocks. A layer of amorphous spider silk (containing mostly random coils structures) film with a thickness of 1.1 μm is spin-coated on silicon substrate, followed by an EBL writing step that constructs a series of nano pillars (diameter: 300 nm) from the bottom to the top of the film, providing stable support for subsequent processing. Next, a second step of IBL was used to induce localized structural transitions in only the top part of the spider silk film by precisely controlling ion irradiation dosage. At last, water development was performed to reveal the 3D nanostructures. The structural complexity achieved by the Protein LEGO is essential in applications such as microenvironment reconstruction, cell sorting, and biomimetic devices. The proposed Protein LEGO method compares

favorably to DNA origami and multi-photon lithography, which are the two major techniques for fabrication of 3D structures in biological applications, thanks to its capability of fabricating multi-scale structure with facile functionalization. DNA origami offers advantages of fine structural resolution and complexity with typical structure dimensions in the 1-100 nm range by designing the sequence of staple strands and controlling the subsequence self-assembly process with careful management of temperature, pH value, and time. However, self-assembly with longer DNA strands has suffered from extremely low yields even for simple geometries due to the complexity of folding a very large DNA strand into a compact shape. On the other hand, multi-photon based 3D lithography has been demonstrated to fabricate arbitrary micron-sized 3D structures with ease. By employing oil immersion and two-photon dye, sub-micron structures were also successfully demonstrated. However, both of these processes still suffer from low resolution in the z-direction and involve the usage of toxic substances that compromise the biological activity and restrict the functionalization of biomaterials. The "length scale gap" between 3D biostructures that can be readily fabricated by DNA origami via molecular assembly (comfort zone: 1-100 nm) and multi-photon lithography using biomaterials (comfort zone: > 500 nm) is fulfilled by the reported Protein LEGO method with reduced process complexity and enhanced flexibility of functionalization.

A couple of examples have been realized by following the procedure described above. Nano-desk (Figure 16D) shapes are produced by forming the legs with EBL and desktop with IBL. The desktop is able to maintain its shape with only one additional support at the center in addition to the four desk legs at the corner. Even more remarkably, nanoscale spider webs are also demonstrated in Figure 16E by fabricating the supporting pillar with EBL and the spider web lines (with an aspect ratio of 1000:70) with IBL. The fluorescent images of fluorescein sodium (green) doped and Rhodamine B

(RB, red) doped spider silk nanoweb demonstrate the 3D nature of the nanoweb where the RB doped nanoweb is folded due to the intentional removal of two of the anchor points of the nanoweb, whose 3D nature is otherwise difficult to reveal using our current confocal imaging set up due to the small geometries, especially in the z direction. Similar results have been successfully achieved with genetically engineered fluorescent spider silk. The fact that both the thin desktop and the delicate spider web lines can survive the water development step and sustain their designed shapes is a manifestation of the exceptional mechanical strength of the genetically engineered spider silk and the reliability of this fabrication paradigm. In addition, heterogeneous, hierarchical silk structures in the form of biomimetic spider webs can be realized either laterally or vertically using different types of genetically engineered spider dragline silk proteins MaSp1 and MaSp2 known for their outstanding mechanical strength and elasticity respectively, which are further modified with different functions (e.g., red and green fluorescent, respectively), underlining the flexibility and versatility of this platform.

The unique combination of genetically engineered spider silk and IBL fabrication technique – Protein LEGO, offers extensive versatility for a variety of applications that require devices to be produced in a "green" way with customizable bio-functions and accurate nanoscopic geometries and serves as a promising alternative to complement current 3D bionanofabrication techniques such as DNA origami and multi-photon lithography. Scanning based manufacturing techniques (e.g., IBL, EBL, and scanning probe based lithography) usually suffer from relatively low throughput. However, IBL is nonetheless notably faster than EBL because ions carry more energy than electrons, therefore requiring a lower irradiation dosage (~1/10 - 1/20 times less than the dosage required for EBL) to crosslink/decrosslink silk proteins. To extend the capability of our methods, more complex and multifunctional structures can be realized by stacking

multiple layers of spider silk protein together, where each layer can be individually fabricated with the desired geometries. What is more appealing is that for each layer, the genetically engineered spider silk can be customized to specific duties for part of a larger task. For instance, the spider silk itself can be modified through genetic engineering to have innate tunable properties such as elasticity, hydrophobicity and molecular weight, as well as through side group conjugation using chemical methods (e.g., UV-sensitization). In addition, by doping the spider silk solution with various types of inorganic and organic molecules, the recombinant spider silk can acquire many different functions. It can also be mixed together with other proteins to serve as hybrid materials (e.g., largely tunable mechanical properties and cell adhesion by mixing with collagen at different ratios). This multiplex of functionality in addition to on-demand nanoscale composite structures adds an entire new dimension to the versatility of this platform.

Concerns may arise regarding the possible ion contamination during IBL process because the Ga+ ions could disturb the bio-compatibility of the fabricated device, rendering it unsuitable for bio-applications. To meet this challenge, we demonstrate successful guided cell seeding and inhibition using pre-patterned functional spider silk substrate in this work, which suggests that the ions do not have a significant effect on the cytocompatibility of the fabricated device. This can be further improved by utilizing IBL system based on inert Helium (He) ion, which offers better fabrication resolution thanks to the lower divergence of He ions in the vicinity of sample surface. In summary, genetically engineered spider silk incorporated with IBL fabrication technique provides a versatile platform to perform multifunctional 3D nanostructuring for current and emerging biomedical applications. This work has been accepted by Advanced Materials.

Chapter 5: The patterning of chemically silk light chain by UV-light

INTRODUCTION TO UV-LITHOGRAPHY USING SILK AS THE RESIST

Precise patterning of micro- and nano-structures using polymer-based biomaterials has extensive applications including drug release, degradable implants, tissue engineering, and regenerative medicine (*29*). The silk based material provides an ideal platform for such applications and has been investigated as a manufacturable material using EBL, IBL, and Imprint Lithography, etc. Photolithography, in particular, remains one of the most appealing techniques for scalable biomanufacturing as it is CMOS-compatible and can rapidly fabricate high fidelity micro-/nano-patterns in parallel – in contrast, scanning-probe lithography and electron beam lithography for biomanufacturing use serial manufacturing techniques. Natural silk fibers from Bombyx mori cocoons exist in a self-assembled fibrous configuration, in which a mechanically robust protein - fibroin (~ 75%, w/w) comprises the core, surrounded by a glue protein - sericin (~ 25%, w/w) (*3*). The lack of photo-sensitive functional groups in the molecular structure of the silk protein dictates the incompatibility of the raw silk protein as a photoresist. However, by conjugating the appropriate photosensitive molecules, the modified silk could be used for UV patterning. In fact, patterning of silk microstructures using UV-photolithography has been successfully demonstrated where either silk fibroin or sericin was chemically modified to be photoreactive and then served as the photoresist (*55, 108*). Cell culture studies have been conducted to verify the biocompatibility of silk protein resists after the chemical modification and lithographic process. Though very promising, compared to their commercial counterparts based on synthetic polymers, current silk protein resists still suffer from issues such as relatively low resolution and pattern contrast in terms of lithographic patterns, mainly due to the inevitable wide

[3]molecular weight distribution (ranging from a few tens to a few hundreds of kDa for both silk fibroin and sericin proteins) during the degumming process for protein extraction. Such limits hinder their practical use in precision biopatterning and the semiconductor industry where reliability and repeatability are paramount. Proteins with more uniform molecular structures (such as well-defined chain lengths and molecular weights) and preferably more active group sites for further functionalization have yet to be explored for high-performance protein-based photolithography.

In this study, we report on a precise protein photolithography (P3) for high-performance biopatterning using the well-defined silk fibroin light chain as the basic resist material. Silk fibroin is mainly composed of two components, namely heavy chain (H-fibroin, ~ 85%, w/w) and light chain (L-fibroin, ~ 15%, w/w), which are linked by a single disulfide bond between Cys-c20 of H-fibroin and Cys-172 of L-fibroin (*109, 110*). Compared to silk fibroin and sericin proteins, L-fibroin has a well-defined molecular weight of ~ 26 kDa (*111*). It also has a higher proportion of undifferentiated and hydrophilic amino acid composition than H-fibroin, which facilitates facile chemical modification for the synthesis of a variety of biologically and chemically functional photoresists.

---

[3] This section is based on the following article. The author of this dissertation is the co-author on this paper. Liu, W., Zhou, Z., Zhang, S., Shi, Z., Tabarini, J., Lee, W., . . . Dong, F. (2017). Precise Protein Photolithography (P3): High Performance Biopatterning Using Silk Fibroin Light Chain as the Resist. Advanced Science, 4(9).

SYNTHESIS OF THE PHOTOSENSITIVE SILK LIGHT CHAIN

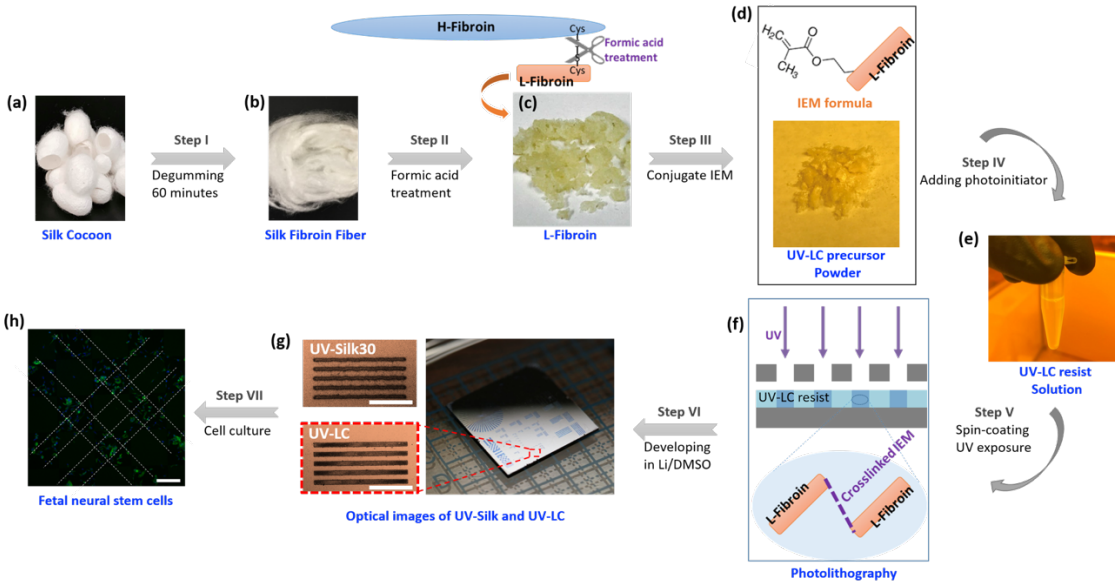

Figure 17: Synthesis of the UV-reactive silk L-fibroin (UV-LC) and the result of photolithography using UV-LC as a negative resist. B. mori cocoons (a) are degummed for 60 minutes to obtain silk fibroin (b), and the L-fibroin (c) is then separated from the silk fibroin using formic acid; (d) photoactive L-fibroin (UV-LC precursor) is obtained by conjugating IEM to the L-fibroin; (e) by adding the photoinitiator (Irgacure 2959), the UV-LC resist can be synthesized; (f) Photolithography using UV-LC resist; (g) Optical images of the fabricated patterns (Linewidth: 5 µm, zoom-in image) shows that UV-LC has better lithographic performance than UV-Silk30. Scale bar: 50 µm. (h) Dark-field stereomicroscopic photograph of double immunofluorescence staining with nestin (green fluorescence) and nuclear staining (blue DAPI staining) of fetal neural stems cells that were guided to be cultured on a micropatterned UV-LC resist (dash line) on a silicon substrate. Scale bar: 100 µm. (*54*)

Figure 17 illustrates the material synthesis, functionalization, and photolithographic results of UV-reactive silk L-fibroin (UV-LC) resists. The Bombyx mori silkworm cocoons were first cut into small pieces and degummed for 60 minutes to remove sericin using a previously reported process (Figure 17A & 17B). Formic acid was used to break the covalent disulfide bonds between H-fibroin and L-fibroin, and to

separate silk fragments based on their different solubility in formic acid without causing severe protein degradation (*112*). The soluble fractions (i.e., L-fibroin) were harvested and air-dried (Figure 17C). The L-fibroin was modified to be photoreactive by conjugating a photoreactive reagent of 2-isocyanatoethyl methacrylate (IEM) to L-fibroin's side groups, yielding a photocrosslinkable UV-LC precursor (Figure 17D). The UV-LC precursor was then dissolved in 1,1,1,3,3,3-hexafluoro-2-propanol (HFIP, Sigma Aldrich, St. Louis, MO). An organic photoinitiator of Irgacure 2959 (Sigma Aldrich, St. Louis, MO) was added 0.5% (w/v) into the UV-LC precursor solution to generate (and transfer) reactive species (free radicals in this case) when exposed to UV radiation (Figure 17E). The UV-LC resist solution (2%, w/v) was spin coated on a silicon or glass substrate to form a resist layer with a controllable thickness ranging from 50 nm to several μm which was then exposed through a photomask (Figure 17F). In this case, the UV-LC resist acted as a negative photoresist which can be crosslinked due to IEM in the presence of UV light (followed by the development step) to generate wafer-scale micropatterns on silicon and glass substrates via standard UV photolithography (Figure 17G). UV-LC microstructures were tested as cellular substrates and for the spatial guidance of fetal neural stems cells which were seeded on micropatterned surfaces and incubated for 3 days. Cells tended to preferentially attach to the UV-LC protein patterns in comparison to the surrounding surface (i.e., silicon in this case) (Figure 17H). Note that the sensitivity of UV-LC resists can be readily tuned by regulating the IEM molecules conjugated into L-fibroin. Additionally, the presence of unmodified amino acids can enable further functions (e.g., association with favorable cellular interactions and the production of multifunctional biomaterial architectures) via concurrent or subsequent modification strategies. In this study, the IEM molecules were intentionally designed to exceed the population of available amino acids conversion to fully occupy

nearly all active group sites on the protein chains to better investigate the underlying mechanism of photo-only-induced formation of crosslinked silk micro-/nano structures.

FABRICATION CHARACTERISTICS OF THE UV SENSITIZED SILK LIGHT-CHAIN

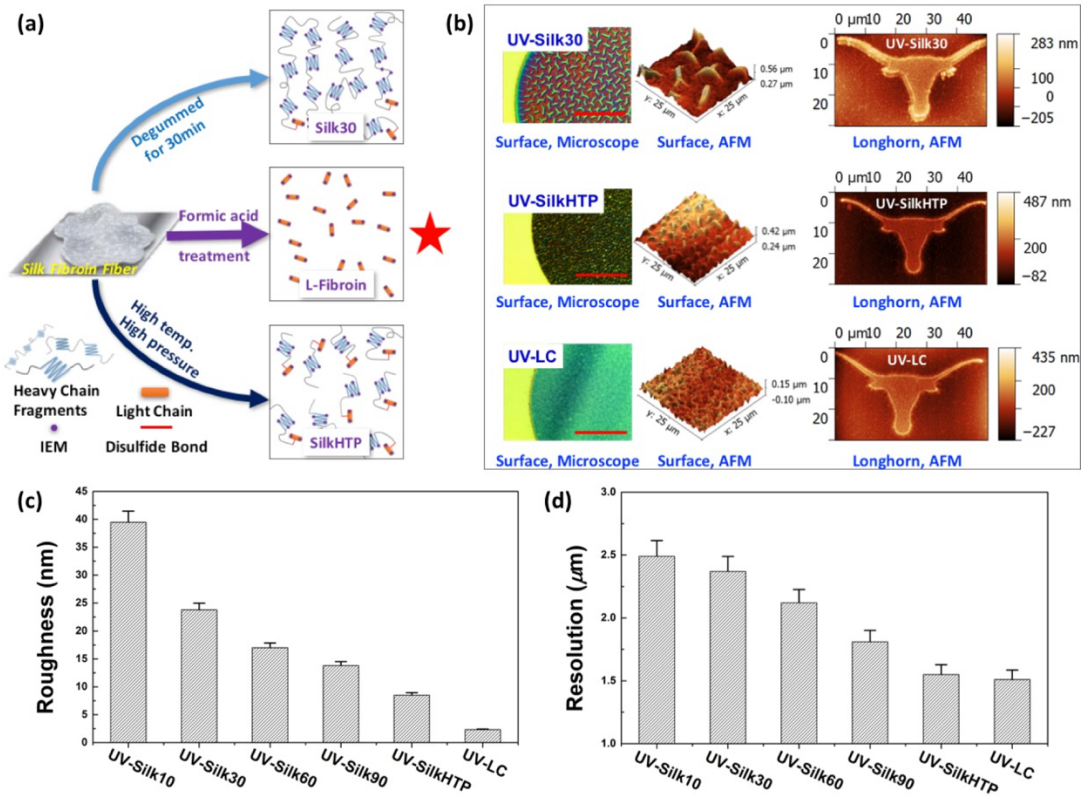

Figure 18: Characterization and analysis of patterns fabricated by protein photolithography using different types of silk-based materials (e.g. UV-Silk30, UV-SilkHTP, and UV-LC). (a) Schematic comparison between structures of UV-LC and UV-Silk (including both UV-Silk30 and UV-SilkHTP) precursor, where UV-Silk30 has longer protein chains than UV-HTP. UV-LC contains only L-fibroin; (b) Morphological characterization (using an optical microscope and AFM, scale bar: 200 μm) of micropatterns fabricated by protein photolithography using UV-Silk30, UV-SilkHTP, and UV-LC. It shows that the UV-LC can achieve better resolution and surface smoothness than UV-Silk30 and UV-SilkHTP; (c) and (d) Quantitative analysis of resolution and surface roughness of micropatterns fabricated using various UV-Silk and UV-LC. The result is consistent with the observations from optical and AFM images. (*54*)

A variety of photoreactive fibroin (UV-Silk) resists with varied degumming conditions (thus varied protein chain lengths and molecular weight distributions) have been prepared for comparison using a previously reported method. Note that UV-Silk

resists consist of both H-fibroin and L-fibroin fragments, while UV-LC only has L-fibroin. Figure 18A schematically shows the (simplified) molecular structures of some example UV-Silk and UV-LC precursors, including UV-Silk made of silk fibroin fibers degummed for 30 minutes (UV-Silk30), degummed at high temperature (121 ºC) and pressure (25 psi) for 4 hr (UV-SilkHTP), and L-fibroin protein, respectively. In general, longer degumming time results in shorter but more uniform silk fibroin fragments. Therefore, compared to UV-Silk30, the H-fibroin fragments in UV-SilkHTP are generally shorter but more uniform due to the high temperature and pressure treatment conditions during its extended degumming process. In comparison, UV-LC provides a promising route serving as the basic molecular blocks for precise protein photolithography thanks to its well-defined and evenly distributed protein chains.

The surface morphology and fidelity of as-fabricated micropatterns on isopropyl alcohol (IPA) cleaned silicon substrates using UV-LC and UV-Silk protein resists were characterized and compared using Atomic Force Microscopy (AFM) and an optical microscope, showing that lithographic performances including the spatial resolution, pattern sharpness, and surface morphology/roughness strongly depend on the molecular structures of as-used protein resists (Figure 18B). AFM results show that UV-LC has the best surface roughness with a root mean square (RMS) roughness of ~ 2.3 nm while UV-SilkHTP (~ 8.5 nm) is better than UV-Silk30 (~ 23.8 nm), over an area of 5 × 5 μm. We postulate that, during drying, silk fibroin proteins spontaneously form micro- and nano-scale wrinkled patterns guided by a diffusion-limited aggregation process (DLA) (*113*) which has been observed in the assembly of a range of materials including colloids, polymer thin films (*114*), peptides (*115, 116*), and proteins (*117*). This is partially due to the polarity mismatch between photoreactive silk resists consisting of strongly polar side groups, such as hydroxyl, carboxyl, and amino groups (thus strongly polar) and the IPA-

treated silicon (weakly polar) substrate, which can be improved by appropriate surface treatment of silicon substrates (Details in the Supplemental Information). The mismatch increases with the protein chain length and uneven distribution of the molecule weight where the internal molecular polarity difference within the protein chain becomes more predominant due to increased ratio between the hydrophobic H-Fibroin fragments and the hydrophilic L-Fibroin fragments (Figure 18C).

Figure 18D shows that, under the same lithographic conditions (i.e., exposure duration and development time), the resolution (which was determined by the minimum distinguishable feature size in our case, see the Supplemental Information) of UV-Silk resists improves with the increasing degumming time, due to the decreased (and more uniformly distributed) molecular weight. The UV-SilkHTP and UV-LC provide better lithographic performances in terms of resolution, yielding minimum feature sizes of 1.54 and 1.51 μm, respectively, close to the minimum designed feature size of the mask (1.5 μm), which was chosen based on the capabilities of our current photolithography setup.

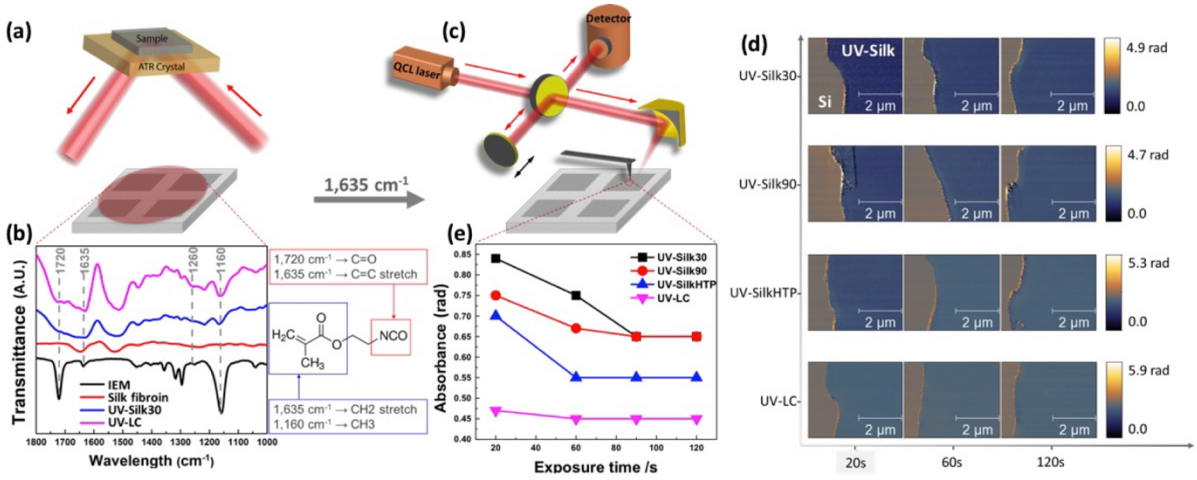

Figure 19: Structural characterization of the UV-Silk and UV-LC using FTIR and s-SNOM. (a) Schematic of ATR-FTIR setup, where the sample is illuminated from the back of the ATR crystal; (b) FTIR spectrum of IEM, silk fibroin protein, UV-silk, and UV-LC. The peaks vanish in the UV-Silk and UV-LC, indicating the binding of IEM on silk fibroin and L-fibroin; (c) Schematic of the s-SNOM system. An infrared laser is focused onto the AFM tip, and the scattered signal is collected by the detector; (d) & (e) IR nano-imaging and absorbance (acquired by s-SNOM measurement performed at 1,635 cm^{-1}) of UV-Silk30, UV-Silk90, UV-SilkHTP and UV-LC with various exposure time. The disappearance of the absorbance with increasing exposure time indicates the increasing crosslinking degree of IEM until about 90 s, after which time all the available IEM active conjugated acrylate group sites are crosslinked. (*54*)

The underlying crosslinking mechanism via the conjugation of the multifunctional acrylate moiety (i.e., IEM in this case) to silk fibroin proteins (including both H-fibroin and L-fibroin) and L-fibroin only - at macro and nano-scale - was investigated via both Fourier transform infrared spectroscopy (FTIR) and the scattering-type scanning near-field optical microscopy (s-SNOM), respectively. Three characteristic peaks (red curve, Figure 18b) were found in Amide I (1,600 ~ 1,700 cm^{-1}), Amide II (1,500 ~ 1,600 cm^{-1}), and Amide III (1,200 ~ 1,300 cm^{-1}) bands for bulk silk fibroin proteins measured by FTIR in the attenuated total reflection (ATR) mode with an aperture size of several tens of

microns (Figure 19A), which gradually decreased after the introduction of the photoactive component IEM (Figure 19B). Three prominent peaks (blue and pink curves for UV-Silk and UV-LC, respectively) surged at 1,720 cm^{-1} (C=O stretch), 1,635 cm^{-1} (terminal C=C stretch) and 1,160 cm^{-1} (C–O stretch), which overlapped with the characteristic peaks of pure IEM.

s-SNOM was employed to provide direct imaging and chemical identification of the thin protein layers at the nanoscale, to understand the variation of local chemical composites during crosslinking under UV exposure, and to overcome the special resolution and thickness limits of FTIR spectroscopic study. In this work, s-SNOM (NeaSNOM, Neaspec GmbH, Germany) has been utilized for high-resolution optical images and spectroscopic information to map out the chemical and mechanical properties of protein patterns at the nanoscale with a spatial resolution of ~ 20 nm. In our setup, s-SNOM is coupled to a tunable IR quantum cascade laser (QCL, Daylight Solutions Inc., USA) covering the broad IR spectra of the Amide I and II bands over the range from 1,450 to 1,750 cm^{-1} (Figure 19C). The near-field phase spectrum resembles the molecular absorbance band, while the near-field amplitude spectrum acquires a dispersive line shape similar to a far-field reflectivity spectrum.

The crosslinking degree was measured by using absorbance phase images, where the absorbance intensity at characteristic peak of crosslinking is inversely proportional to the degree of crosslink. Absorbance phase images of UV-Silk30, UV-Silk90, UV-SilkHTP, and UV-LC patterns on a silicon substrate were captured at 1,635 cm^{-1}, which corresponds to IEM-induced photocrosslinking from terminal C=C group sites. As shown in Figure 19D, at 1,635 cm^{-1}, the phase image exhibited a strong contrast between silk and silicon (silicon is used as the reference for IR imaging) in UV-Silk30 micropatterns that were exposed for 20 s. The contrast gradually weakened with the longer exposure time

indicating an increased crosslinking degree. IEM-induced crosslinking degrees within various protein micropatterns were obtained and evaluated quantitatively (Figure 19E). The absorbance intensity of UV-Silk30 samples decreased monotonically with increasing exposure time until 90 s, indicating an increase in crosslinking degree due to IEM. The crosslinking was found to be saturated after 90 s exposure which expended all available active conjugated acrylate group sites and remained nearly constant thereafter. It is found that UV-Silk resists with lower molecular weights are easier to crosslink partially due to their higher degrees of molecular mobility and more uniform protein chain lengths. Compared to UV-Silk resists, UV-LC resist shows considerably higher sensitivity thanks to its shorter protein chain length and more available IEM side groups.

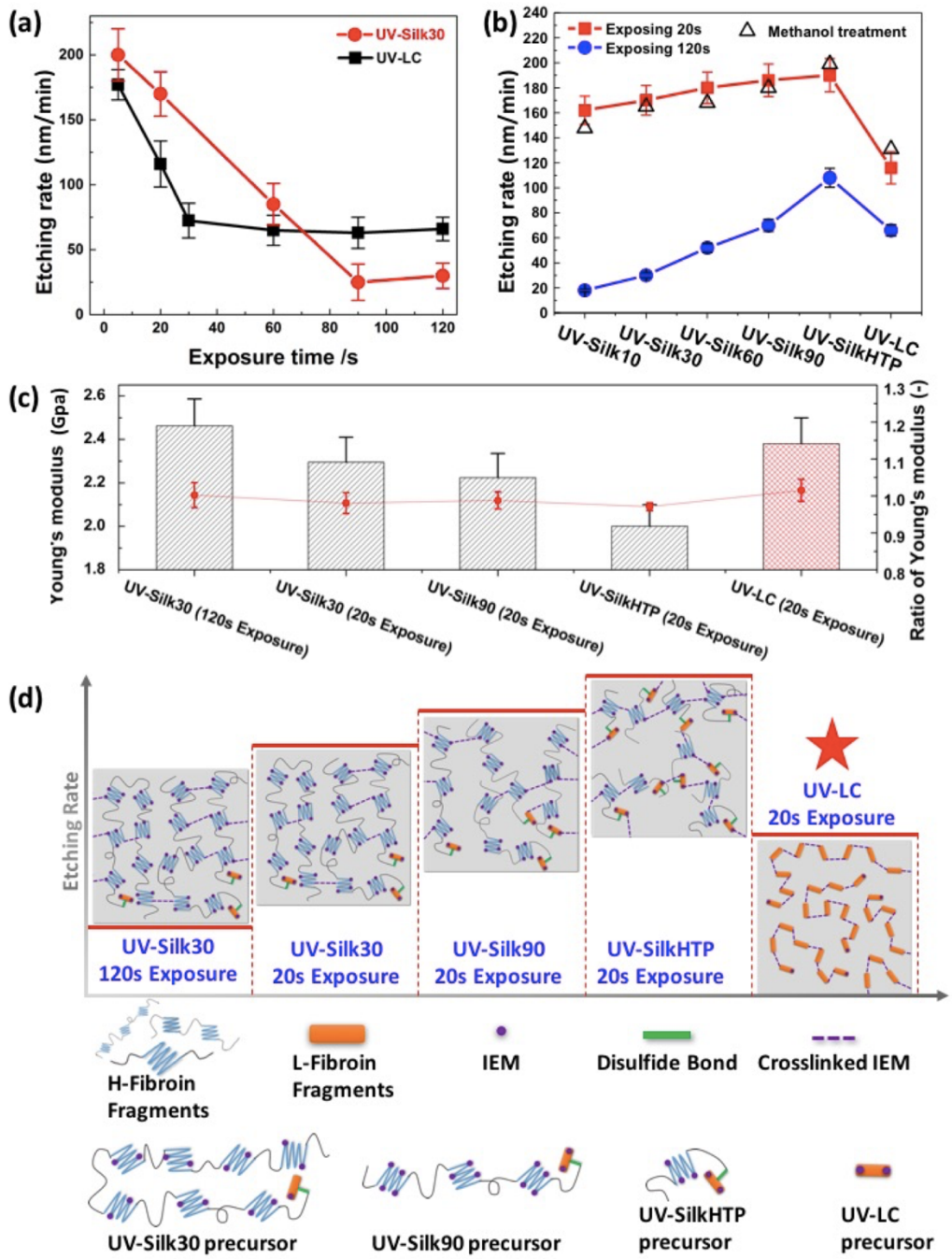

Figure 20: Etching rate measurements and schematic structures of various UV-Silk and UV-LC. (a) Etching rate measurement of the UV-Silk30 and UV-LC with increasing exposure time. The etching rate of UV-LC decreases faster than

the UV-Silk30 with increasing exposure time but reaches a constant rate that is higher than UV-Silk30; (b) Etching rate comparison between various UV-Silk (including both UV-Silk and methanol treated UV-Silk) and UV-LC at two exposure times (20s and 120s). All the samples with 20 s exposure times have larger etching rate than the samples with 120 s exposure times. UV-Silk has an increasing etching rate with increasing degumming time because the mechanical strength is better with longer chain length. UV-LC has slightly less etching rate because its highly defined molecular structure help form better crystalline structure; (c) Young's modulus of UV-Silk and UV-LC and ratio of Young's modulus before and after methanol treatment. It shows the similar trend with the data of etching speed, where the largest Young's modulus value corresponds to slower etching rate. It also shows no obvious change by treating with methanol, which indicates little amount of beta sheet structure present in UV-Silk and UV-LC; (d) Schematic structure and the corresponding etching rate of the photocrosslinked UV-Silk and UV-LC with 20 s exposure time and UV-Silk30 exposed for 120 s. For UV-Silk30, the etching rate decreases with longer exposure time because of the increased crosslinking degree. With the same exposure time, the etching rate increases with increasing degumming time because of the shorter chain length, and thus less mechanical strength. With 20 s exposure (partially crosslinking) UV-LC has less etching speed because its highly defined molecular structure helps it form better IEM-induced crystalline structure. (*54*)

One main use of photolithography is to pattern a resist layer which can serve as a temporary mask when etching an underlying layer. Therefore, a systematic study on the use of UV-Silk and UV-LC resists as the etching mask for pattern transfer was conducted. We've found that there are at least three factors that play an important and synergistic role in the etching performance (i.e., etching resistance) of the silk-based microstructures, namely, 1) the average molecular weight (i.e., average protein chain length, which is determined by the degumming process (for UV-Silk resists) and protein separation process (for UV-LC resist)); 2) the photoinduced crosslinking due to IEM; and 3) the crosslinking due to the formation of beta sheets. We first investigated the dependence of etching performance on the photoinduced crosslinking within the protein matrix and the protein chain lengths. As shown in Figure 20A, the etching rates of both

UV-Silk30 and UV-LC resists decreased monotonically with the increased exposure time (and thus the increased crosslinking degree before saturation) and reached plateaus at ~ 25.4 nm/min and ~ 72.4 nm/min after UV exposure of 90 s and 30 s, respectively. The etching resistance of UV-LC was initially better than UV-Silk30 since the crosslinking degree in UV-LC was considerably higher than UV-Silk30 under the same exposure conditions. With the increased exposure time, the molecular weight of silk protein chains became to play a more important role and UV-Silk30 showed a better etching resistance when both resists were fully crosslinked.

We designed two sets of experiments to systematically investigate the etching performance among a variety of silk resists (including both UV-Silk and UV-LC ones) that were 1) partially crosslinked (for 20 s exposure so that all resists were "under-exposed") and 2) fully crosslinked (for 120 s exposure so that all resists were "over-exposed") (Figure 20B). It has been found that, under same exposure conditions (for both partially and fully crosslinking cases), the etching rate of UV-Silk resists increased with the degumming time. This is mainly due to the reduced protein chain length during the prolonged degumming process which weakens the mechanical strength of the as-prepared protein resist and causes the increase in the etching rate (Figure 20C). A schematic illustration of the underlying mechanism is given in Figure 20D. We then compared the etching performances of UV-LC resist to UV-Silk ones. In the partially crosslinking case, the UV-LC resist showed the best etching performance due to its significantly higher crosslinking degree than all UV-Silk resists (also see Figure 20E). However, for the fully crosslinking case, a competing mechanism becomes more noticeable between the crosslinking degree and the molecular weight on the etching performance. Generally, UV-LC resist has much lower molecular weight but higher crosslinking degree than UV-Silk resists under same exposure conditions. Therefore, when fully crosslinked, UV-Silk

resists with relatively short degummed time showed better etching resistance than UV-LC, due to their much higher molecular weights and better mechanical strengths. UV-Silk90 shows a comparable etching resistance to UV-LC as it has higher molecular weight but less crosslinking degree. UV-SilkHTP shows the highest etching rate as it has much lower average molecular weight than other UV-Silk counterparts due to the excessive degumming time under high temperature and pressure.

Furthermore, we've found that the influence of the secondary structure of beta sheets within silk resists on their etching performances is considerably minor compared to the other two factors, namely, the average molecular weight and IEM-induced crosslink. It is well known that methanol treatment can promote the formation of beta sheets within the silk protein matrix. No noticeable variation was found in terms of the etching resistance and Young's modulus before and after the methanol treatment for all silk resist samples (Figure 20B and 20C). We attribute this to the fact that the degree of IEM substitution was designed to exceed the population of amino acids conversion so to occupy almost all the active group sites on the protein chains, which hindered the formation of β-sheet structures in the protein resist matrix.

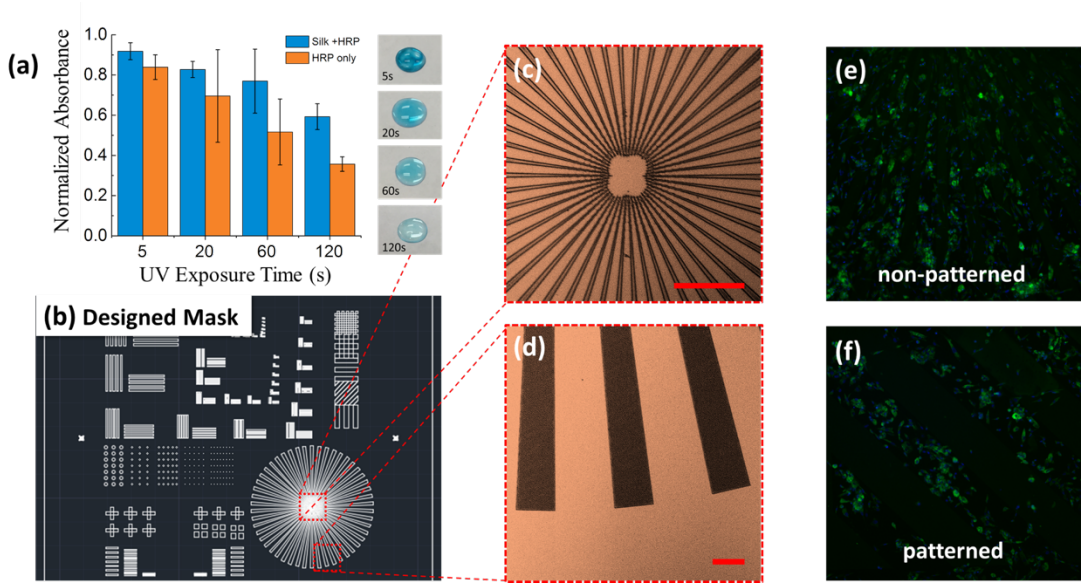

Figure 21: (a) Bioactivity evaluation of HRP-doped silk resist and HRP enzyme after UV exposure. The ELISA test shows that enzyme activities are negatively affected during UV exposure and silk resists can help to stabilize the bioactivities to some extent during UV exposure; (b) Patten design of as-used photomask. (c)-(f) Double immunofluorescence staining with nestin (green fluorescence) and nuclear staining (blue DAPI staining) of fetal neural stem cells cultured on UC-LC substrates showing the spatial guidance of cell seeding. Scale bar: 100 μm. (*54*)

One of the most compelling attributes of silk materials is their abilities to allow for the incorporation of functional elements such as labile biological components with retention of bioactivity to generate functional material formats. The effectiveness of UV-LC photolithography to large scale reproduce microscale geometries and topologies allows for functional components to be generated from silk. We therefore explore the doping and stabilization of UV-LC patterns with an enzyme of horseradish peroxidase (HRP) and the effects of the UV-LC photolithography process on its bioactivities as proof-of-principle demonstrations. As shown in Figure 21A & 21B, the enzymatic activity of the HRP-doped UV-LC resist was assessed by a colorimetric enzyme-linked

immunosorbent assay (ELISA) for HRP/ 3,3′,5,5′-tetramethylbenzidine (TMB) after UV exposure and pattern development. The bioactivity test shows that as-prepared patterns possess bioactivity of embedded biological molecules to some extent (i.e., HRP-dope UV patterns turn blue after exposure to TMB) during UV-LC photolithography. Finally, UV-LC microstructures were fabricated and examined using a standard immunofluorescence assay as biocompatible cellular substrates (Figure 21C – 21E). Fetal neural stem cells were seeded on non-patterned (i.e., a uniform coating of UV-LC resist w/o UV exposure) and patterned surfaces using UV-LC photolithography and incubated for 3 days. As shown in Figure 21F & 21G, cells were well anchored to the UV-LC substrates in both cases and tended to preferentially attach to UV-LC patterned compared to the surrounding surface (i.e., silicon in this case), showing that UV-LC micropatterns have good biocompatibility and can be used for precisely spatial cell guidance.

In conclusion, we report on a precise protein photolithography (P^3) for wafer-scale, high-performance biopatterning using chemically modified well-defined silk L-fibroins as the photoresist material. The lithographic and etching performance of UV-LC and UV-Silk resists have been evaluated systematically and the underlying mechanisms have been thoroughly discussed. A general guidance on the synthesis and the use of silk L-fibroin resist has been provided. The inherent biocompatibility and the enhanced patterning resolution along with the improved surface roughness and etching performance of such protein-based resists offer new opportunities in fabricating large-scale high-precision biocompatible functional micro-/nano structures. This work has been published by Advanced Science.

Chapter 6: The stabilization of bio-compounds in silk matrix

INTRODUCTION TO THE STABILITY OF LABILE BIOSPECIES

One of the versatility of the silk based platform is manifested in the multiple pathways that the base material – silk can be functionalized. Apart from genetic engineering and chemical modification, a simple doping process can impart a wide range of functionalities into the silk matrix by using the appropriate dopants such as quantum dots, nanoparticles, small molecule drug, etc. In particular, biocompounds can be used as the dopants to offer bioactivities to the silk material. During this process, the silk protein not only act as a carrier, it also stabilizes the fragile compounds which would otherwise lose their bioactivity within hours in the ambient conditions.

Biocompounds, including biomolecules and larger species such as virus and cells, become important tractions as therapeutics, diagnostics tools, and various other industrial applications. Despite the wide usage, the biocompounds are usually very fragile and can only maintain their activity for a limited amount of time in a controlled environment (which often involve refrigeration or freezing). Therefore, there have been significant challenges associated with the maintenance of activities/functions of the biocompounds during the manufacturing, handling, transportation, and storage. Currently, the most widely adopted method of preserving bioactivities is refrigeration, or also known as the cold chain (*118*). The cold chain is a series of refrigeration based processing of the labile compounds, prolonging the bioactivities of the biocompounds for a slightly extended period of time. However, there are two issues with the cold chain. First of all, the mechanisms by which the biocompounds degrades (related to and categorized by physical and chemical stability) is a complex process that involves parameters more than the temperature itself (*119*). Therefore, while refrigeration does indeed provide a way to

improve the stability of biocompounds, its effectiveness is not always consistent and sometimes can be futile. In addition, the maintenance of a stable, and low temperature environment can be economically inhibiting. The estimated cost for the cold chain used to store and transport vaccine alone is about $200 – 300 million per year (*120*). The inconsistent ineffectiveness and the significant economic burden of the cold chain has stimulated the research on alternative ways to preserve labile biocompounds.

One of many of the investigated methods of improving the stability of the biocompounds is to use a carrier material, which "protects" the biocompounds from potential degradation pathways (*119, 121*). In this context, the silk protein matrix has been reported to effectively stabilize the bioactivity of a wide range of biocompounds ranging from small molecule drugs (e.g. antibodies) , to macromolecules (e.g. enzymes), and even larger species (e.g. virus, bacteriophages, and even cells) (*122-129*).

THE PHYSICAL AND CHEMICAL STABILITY OF THE BIOCOMPOUNDS

The labile biocompounds are subject to a number of different stresses that are associated with their degradation, categorized by physical ones and chemical ones (*130*). The physical stability is typically described by the secondary, tertiary, and quaternary structures of proteins without affecting the covalent bonds. The physical instability can lead to several issues, including denaturation, solvent exposure to labile residues, adsorption to surfaces, self-association, precipitation and aggregation (*131*). The aggregation is particularly problematic for therapeutics because of its potential to induce immunogenicity and compromise efficacy. In general, there are two key factors related to the physical stability of biocompounds, namely, structural stability and solution energetics.

The structural stability refers to the aspect of the biocompounds to remain its native conformation, which is determined by a complex interaction of weak and opposing forces. The maintenance of the native folded structure arises from the natural desire of systems to reside in a lowest energy state (*132*). Therefore, the de-stabilizing factors break this balance by increasing the entropy of the unfolded state. The structural stability is influenced by many inter-atomic forces, including the hydrophobic interactions, ion pairs or salt bridges, electrostatic forces, Van der Waals interactions, and hydrogen boding (*133, 134*). Each of the factors are relatively weak, but together contributes to the instability and aggregation of the protein. On the other hand, solution energetics is a combinatory effect of protein–protein, protein–surface, and protein–solvent interactions (*135, 136*). They are governed by the same weak forces that affect the structural stability of protein. In addition, it has recently been proposed that the net surface charge and surface charge distribution are critical factors that influence the solution energetics.

The chemical stability of the biocompounds is associated with the chemical modification and even damage of the amino acid residues (*137*). Many of the amino acid residues are subject to chemical damage (*138*), which often result in the altered function and physical instability of the protein. Among the many pathways of the chemical damage, deamidation is the most common one, which is non-enzymatic reaction occurring mostly on asparagine residues. The product deamidation results in the introduction of a charged side residue in place of a neutral one, thereby disrupting the local protein structure. Another important pathway of chemical stability is the oxidation. The oxidation affects all residues with aromatic or sulfur containing side chains, and the methionine side groups are susceptible. Similar to deamidation, the oxidation decreases the structural stability and change the propensity of aggregation.

THE STABILIZATION OF BIOCOMPOUNDS IN SILK

Based on the pathways and mechanisms that affect the stability of the biocompounds, there are corresponding strategies to mitigate those stresses. The physical stability is affected by solution pH, ionic strength, and buffer species, where the pH changes the net charge and the charge distribution on the side groups. The native state of the biocompounds can actually be stabilized by sugars (e.g. sucrose, glucose, lactose, and trehalose) (*139, 140*) at high concentrations based on the preferential exclusion mechanism. The sugar molecules are preferentially excluded from the gap where the two-molecule associate is formed. Thus the free energy of the partially associated intermediate is increased, reducing the protein-protein aggregation.

The above mentioned mitigation strategies are all solution based, since the low cost of liquid formulation has driven the development of drug products. However, many of the biocompounds cannot be effectively stored in a solution environment, even at low temperature. In this context, solid state stabilization has gained considerable interests as an alternative way to storing biocompounds. The conventional solid state stabilization involves freezing or lyophilization, which dramatically decrease the molecular mobility, thus reducing the chemical pathway of degradation. However, the freezing and lyophilization may exert some stress on the physical aspect of degradation.

The silk based stabilization of the biocompounds could take in the form of both liquid state and solid state. In the liquid state, the silk protein stabilizes the biocompounds via preferential interactions (*141*). In this mechanism, the molecules are surrounded by a layer of "water shell", with another layer of silk protein on the outside. If the molecules were to unfold, the exposed surface area would increase, which requires a larger volume of exclusion. However, all natural system prefers to stay in the lowest energy, and therefore, the unfolding of the molecules is not favored. In addition, the hydrophobic and

electrostatic interaction between the silk protein and the molecules plays an important role. The shielding effect of the hydrophobic domains of the silk protein can improve the physical stability by mitigating the protein-protein interactions. Meanwhile, the highly charged silk molecules can alter the surface charges of the biocompounds, reducing the protein-protein interaction. In the solid state, there are two major hypotheses that are used to explain the stabilization mechanism of the silk protein. The first is the water replacement hypothesis (*142*), which simply imply that the silk protein take the place of water molecule in the biocompounds in the dried state, and the hydrogen bonding between the silk protein and the biocompounds help to stabilize. The other hypothesis is the vitrification (*143*), which relate the degradation kinetics to the molecular mobility of the molecules in a glassy matrix. Both of which are useful at predicting the stabilization behavior of the biocompounds in the silk matrix.

THE NANOSCALE VISUALIZATION OF THE STABILIZATION OF BACTERIOPHAGE IN THE SILK FILM

In order to visualize the state of the biocompounds in the silk matrix, the appropriate type of sample is needed. In terms of size, the silk matrix interacts with the biocomopounds at the nanoscale, so a smaller type of sample is preferred. However, if the size is too small, the limitation of the current microscopy technique become the bottleneck of the investigation. In this work, we choose the bacteriophage, specifically, M13, as the target to the study the interaction between the silk and the phage. The M13 bacteriophage is a virus that can infect e.coli, and has been widely used in genetic engineering and nanotechnology (*144*). The M-13 phage is composed of a single stranded DNA enclosed by a protein tube made of about 2700 copies of a single protein, called P8.

The protein coat of the M-13 phage is mostly helical in conformation and the size of the phage is about 7nm in diameter and ~900nm in length (*145*). The appropriate size is ideal for the observation of the interaction between silk matrix and the biocompounds using the s-SNOM.

THE CHALLENGES OF OBSERVING THE M13 BACTERIOPHAGE USING SNOM

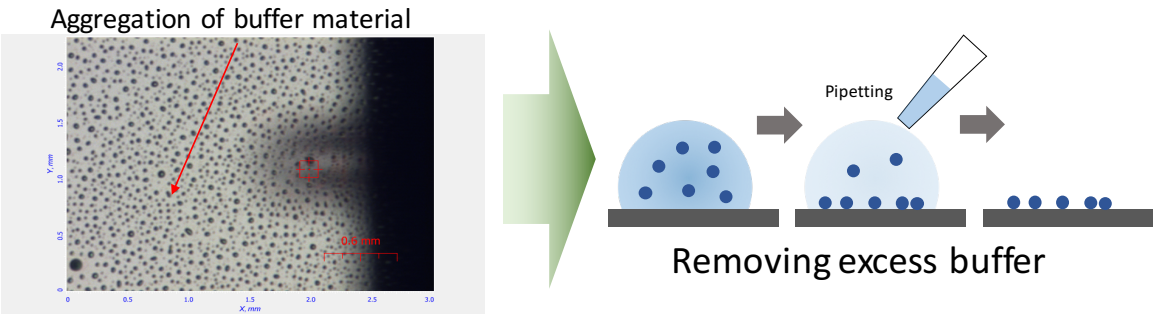

Figure 22: Eliminating the influence of buffer solution for SNOM observation.

One of the greatest challenges of observing live virus and cells using the s-SNOM technique is the elimination of the buffer solution in which the virus and cells live in. Although aqueous phase AFM have been successfully demonstrated in many applications by directly probing the samples in a liquid cell, such operation is difficult to accomplish for s-SNOM in the IR region because of two reasons. First of all, water has very high absorption in the mid-IR region, and the signal strength of the s-SNOM is significantly compromised. Therefore, to obtain a reasonable signal to noise ratio, an exceptionally high laser power is required, which will negatively affect the biocompounds. In addition, since the SNOM operation requires that the AFM to be in the tapping, or semi-contact mode, there is a high frequency excitation at the tip-liquid interface, which induces the formation of surface wrinkles. The wrinkles could interfere and scatter the incident and

reflected signal in random ways that makes the signal extraction much more difficult, Therefore, a solid phase sample is much desired for the observation.

The preparation of the solid phase M13 phage sample involves the drying the of phage and fixing on a flat substrate. The surface smoothness is essential since the M13 phage is very small. The surface roughness should ideally be less than 1nm to have a clear topological definition of the phage. However, the simple drop-casting and drying process of a phage containing buffer does not work because of the residue from the other substance in the buffer solution can either result in large, gel-like aggregations (as shown in Figure 22), or large area crystallization due to the existence of salt. To solve this problem, a three step process is developed. First of all, the phage containing buffer solution is drop-casted on the substrate, which is put on rest for about 30min in a high humidity environment. During this period, the phage tends to precipitate on the substrate surface, and with the appropriate substrate hydrophobicity, some of the phage is fixed on the substrate. The high humidity environment ensures the elimination of the water evaporation during this process. Then the solution is carefully pipetted out either the side of the liquid bubble or the top of it. Since the other content of the buffer solution does not precipitate, the removal of the solution will remove most of the substance that could interfere with the SNOM measurement. The resulting sample will then be completely dried and used for the subsequence investigation.

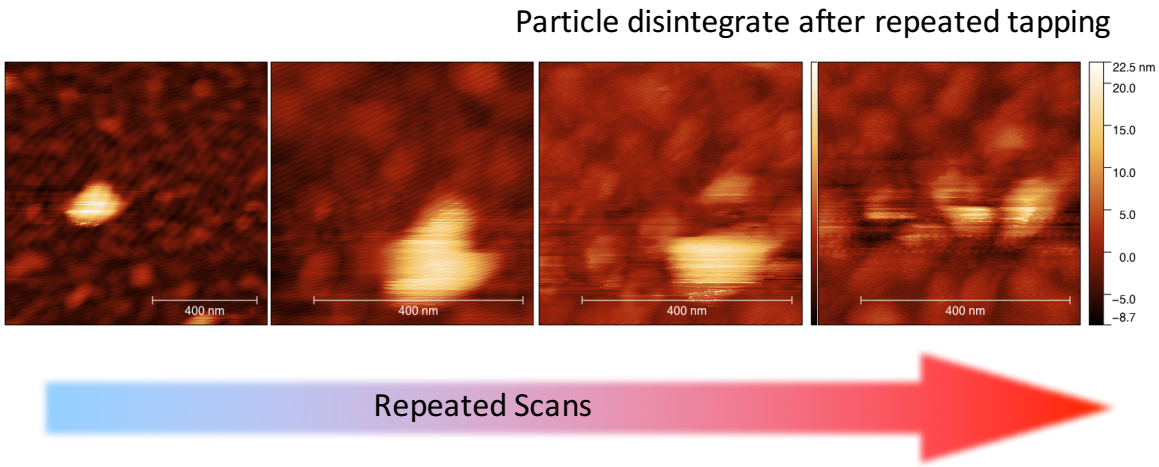

Figure 23: The disintegration of a globular viral particle after repeated AFM scan.

Another challenge of using the AFM based characterization tools on live microorganism is the mechanically induced degradation. Most of the AFM based characterizations of biocompounds operate in tapping mode, which is a much gentler process than the contact mode AFM. With the usage of a softer tip, the damage to the biological sample can be minimized. However, the requirement of the SNOM operation dictates that the mechanical resonance of the AFM tip to be in the range of ~250kHz, which is not considered a very soft tip. Therefore, there is damage associated with the repeated scan on the biological sample. As shown in Figure 23, the globular virus particle disintegrated after several repeated scans. Although the setting of the scan is set to be on the hard side of tapping, softer tapping will still partially damage the sample. Therefore, the AFM tapping set-point needs to be carefully chosen not to disturb the natural state of the biological sample.

THE VISUALIZATION OF M13 PHAGE IN THE SILK MATRIX

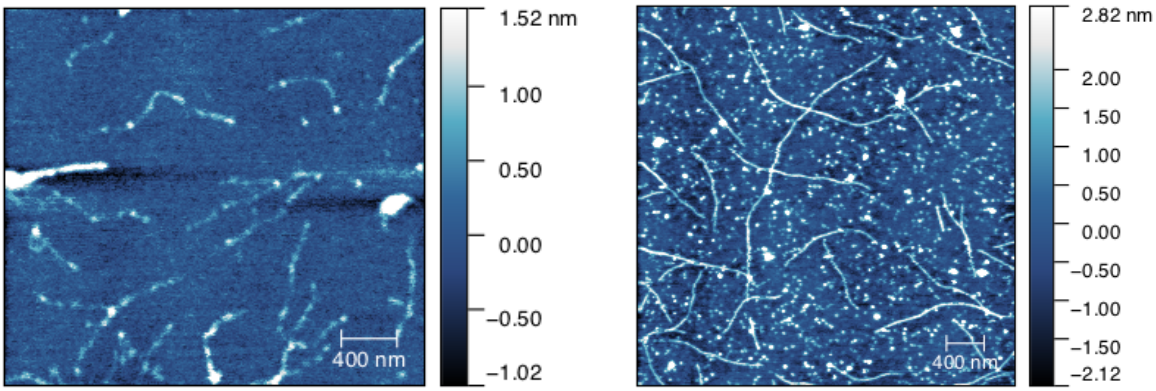

M-13 phage on Gold M-13 phage embedded in silk

Figure 24: The comparison between the M13 phage lying directly on the Si substrate and the M13 phage embedded into a 5nm thick silk film.

After the sample preparation, a preliminary AFM measurement of the topography of the M13 phage is conducted. As shown in the right image of Figure 24, the phage deposited and dried on the Si substrate looks disintegrated. On the other hand, by mixing the phage solution directly with the silk solution and spin coated on the Si with an overall thickness of ~5nm, the morphology of the M13 phage is preserved very well. This is because the silk protein matrix has stabilized both the surface coating protein of the M13 phage as well as the overall phage in bulk. The network of the fibrous silk protein serves as a nano-pockets that contains the M13 phage and prevent them from moving. On the molecular level, the hydrophobic domains of the silk also help stabilize the surface coating protein by shielding it from degradation. This result provides a preliminary evidence of the stabilization of the nanoscale biological sample in the silk matrix.

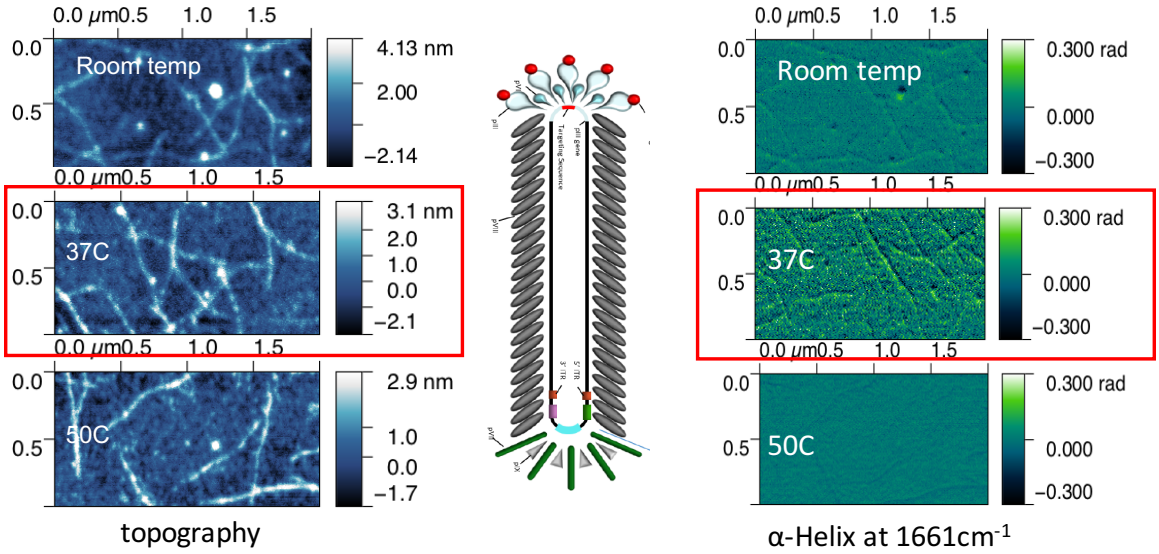

Figure 25: The comparison of the M13 phage stability under different temperature in the silk matrix.

In addition to the morphology, it is possible to evaluate the stability of the M13 phage using the s-SNOM technique. This is because the coating protein of the M13 phage claims a predominant helical structure, which correspond to a specific IR absorption in the amide I band. The structural integrity of the coating protein is highly important for the stability of the M13 phage itself, and therefore can be used as a partial indicator of the phage stability. As shown in Figure 25, the topography and the IR absorption image of the M13 phage embedded in the 5nm silk film measured at different temperature. The contrast in the IR absorption image indicate the stability of the coating protein. The IR image is taken at a wavenumber of 1661cm^{-1}, which is a typical absorption peak of helical protein. As indicated from the IR image, the M13 phage shows the highest contrast at the temperature of 37$^{\circ C}$, which is a physiological temperature for many biological samples. At lower temperature, chemical and biological process are in general very slow because of the retardation of reaction kinetics, and the activity of the biological sample is low. On the other hand, at higher temperature, the chemical stability is

compromised because of the increase rate of chemical reaction that might degrade the biological sample. This experiment demonstrates the applicability of the s-SNOM technique in the study of nanoscale interaction between the silk protein and the M13 phage.

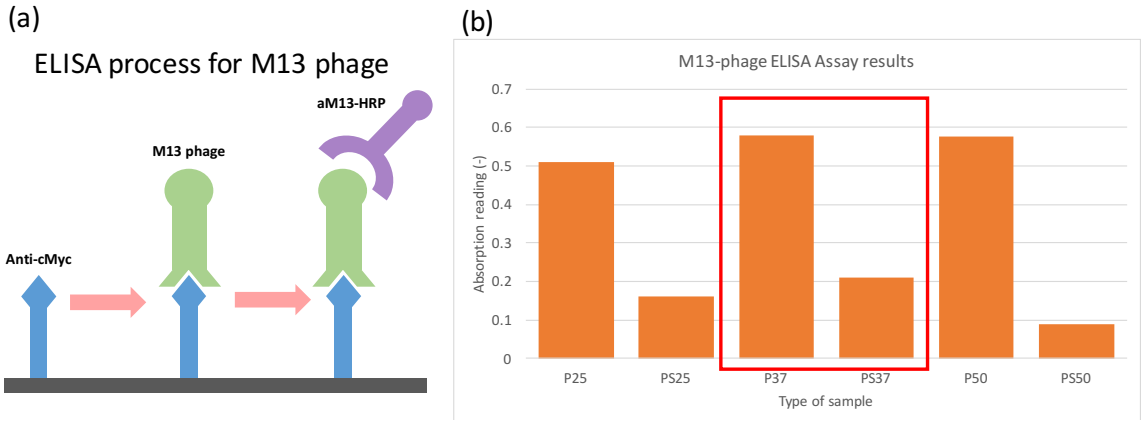

Figure 26: The ELISA test of the M13 phage activity under different temperatures.

Enzyme-linked immunosorbent assay (ELISA) is a plate-based assay technique designed for detecting and quantifying bioactivities of biological samples such as enzymes, proteins, and antibodies. The bioactivity of the M13 phage can be partially indicated by the ELISA technique. As shown in Figure 26A, the ELISA test for the M13 phage involves three steps. Firstly, the anti-cMyc antibody is coated the substrate surface. The anti-cMyc will then bind to the M13 phage when immersed in the M13 phage solution. Next, the HRP-conjugated M13 antibody will bind to the M13 phages that are fixed on the substrate. If the M13 phage is bioactive, the binding will be successful. The addition of the TMB will then create a color reaction whose intensity quantitatively indicate the bioactivity of the M13 phage. As shown in Figure 26b, both the activity of the pure phage (indicated by P) and the phage embedded in the silk solution (indicated by

PS) have the highest value at 37$^{\circ C}$, which agrees well with the s-SNOM measurement. However, the bioactivity of the phage embedded in the silk film is significantly lower than the pure phage. This is due to the smaller number of M13 phage present in the silk film (only a 5nm layer is coated on the substrate) and the possible incomplete release of the M13 phage during the ELISA test.

Chapter 7: The all-water-based silk water lithography for biological applications

ALL WATER BASED SILK PROCESSING

Although the previously reported silk based manufacturing such as EBL, IBL and UV-lithography are largely water based (during the synthesis and development step), the silk protein still need to withstand the bombardment of high energy particles. In this context, a complementary manufacturing process that is non-hazardous, mild, and economically viable is highly desired as an ideal platform for biomedical applications. Among many fabrication techniques, inkjet printing (IJP) has drawn significant attentions owing to the direct patterning mode, economic competitiveness, parallelizability, and ease of use (*56, 146, 147*). The natural matching between the water solubility of the amorphous silk protein and the aqueous printing ink provides an ideal platform for fabricating bio-active structures within a mild manufacturing condition. In this work, the harmonious combination of the IJP manufacturing technique with the silk material (termed silk based water lithography, or silk WL) is presented for scalable and versatile biomanufacturing. Patterns with controllable concave profile on both planar and curved surfaces are successfully demonstrated in both serial and parallelized wafer scale printing process. It is worth noting that compared to the additive nature of conventional ink-jet printing, the silk WL is a naturally dual tone process (that is, both additive and subtractive). The water etching of the silk film features a subtractive mode while the dispensing of functional ink represents the additive side of the manufacturing. Furthermore, the facile inclusion of functional molecules in the water based ink as well as in the silk matrix impart functionality as a new design space to the silk WL platform. Meanwhile, the stabilization capability of the silk protein ensures an optimal operating environment for the doped molecules. This dual mode (i.e. pattering and stabilization) of

manufacturing control exemplifies a generalized lithography process to produce structures with both customizable geometry and functions, which opens up a wide range of opportunities in flexible optics and biomedical applications.

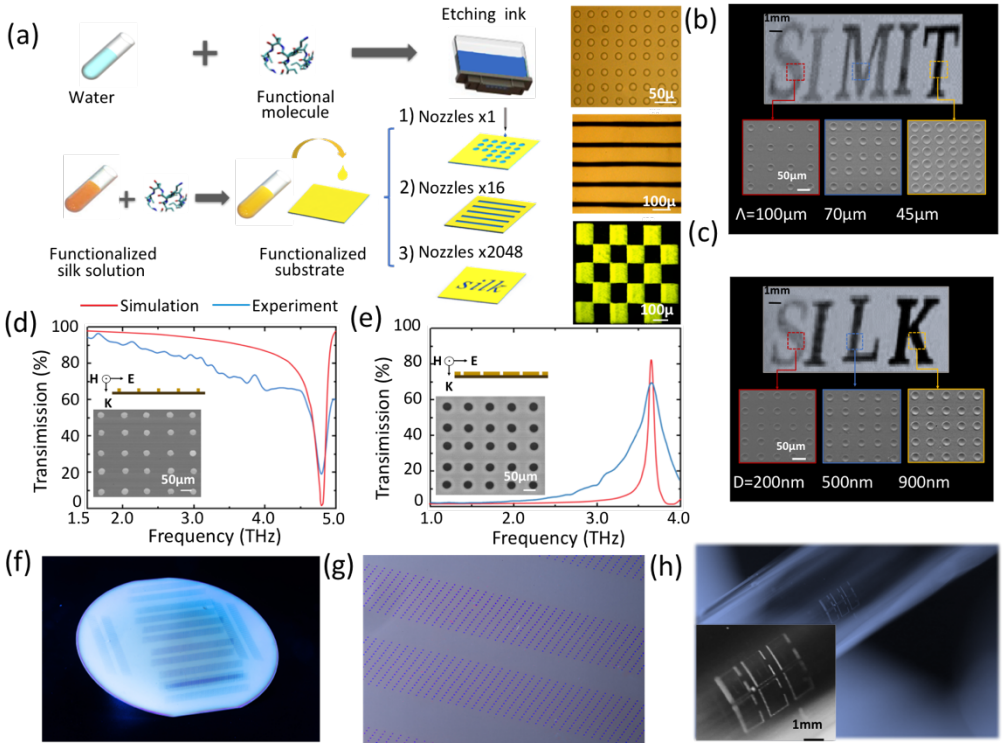

Figure 27: Print-to-pattern on silk substrates. (a) Schematic illustration of silk WL. Both the ink and the silk substrate can be functionalized by the inclusion of molecules. Parallel printing is achieved by using multiple nozzles. Planar patterns including dot matrix, line arrays, and fluorescent checkerboard pattern (by using fluorescein sodium-doped ink) implemented by silk WL. (b, c) Experimental (blue curves) and simulated (red curves) transmission spectra of two types metasurfaces fabricated using silk WL. (d, e) Optical and SEM images of micro-hole arrays with different periodicities (left) and depths (right) generated on silk substrate by silk WL. The micro-pillars are fabricated by liftoff and the micro-holes are fabricated by ion beam etching, where both of the steps are conducted following the WL step. (f, g) With the current setup, 2048 nozzles can print in parallel and wafer scale patterns can be finished within 10 ms (h) Split ring resonator (SRR) array printed on nonplanar substrate using silk WL.

The solubility of the amorphous silk protein in water lays the foundation of the IJP derived silk WL. As shown in Fig. 1a, the ink droplets from the nozzles of the inkjet printers etches down the silk film through dissolution, and create micro-holes (positive pattern) in situ. This process is inherently development-free since the material is directly removed from the printed location. The water based ink used in this process is a natural vehicle for a variety of molecules and particles and therefore adds the corresponding functionalities as a new dimension to the fabricated patterns. Various types of functional molecules, such as fluorescent dyes, growth factor, and therapeutic drugs, can be used in the ink as long as they are soluble in water. Compared with earlier endeavors to integrate silk protein into the IJP platform where the silk solution and other organic solvents (such as methanol) are used as the ink, the silk WL technique eliminates recurring issues of nozzle clogging due to silk gelation as well as bio-incompatibility due to the usage of toxic materials.

The inkjet-printing mode of the WL process naturally ensures its versatility as a generalized lithography platform where not only geometries but also functions are defined in the patterning process. As a proof-of-principle demonstration, dot matrices with an average diameter of 16 μm and center-to-center distance of 30 μm are fabricated (Figure 27A). By regulating the spaces between the individual droplets, smooth lines are successfully fabricated by using a 10 μm droplet spacing. For biologically relevant features, the droplet size is customized to about 5 μm, which can be further reduced by using smaller nozzles. Meanwhile, the inherent advantage of incorporating functional dopants in the aqueous ink has also been tested where a checkerboard pattern is created by printing fluorescein sodium-doped ink. It is worth noting that the silk solution – the resist material in the silk WL process – can also be functionalized by including dopants, which adds another degree of versatility in the

design space of the functional structures. The choice of dopant inclusion in the ink or the silk matrix determines the functional tonality (negative for ink functionalization and positive for silk matrix functionalization) of the printed pattern. As a maskless patterning technique, the regulation of the printing parameters of the silk WL empowers its capability to created grayscale structures. As shown in Figure 27B, the individual letters of the "SIMIT" pattern are composed of two-dimensional dot arrays with different lattice constants (Λ = 100 μm, 70 μm, and 45 μm, respectively), which shows a difference in terms of the shades. From another perspective, grayscale printing can be fulfilled by modulating the etching depth via controlling the number of droplets (Nd) (the depth of the holes are D = 200 nm, 500 nm, and 900 nm, respectively) with the same lattice constant (Λ = 70 μm) as shown in Figure 27C. Such control over both the pattern geometry, periodicity, and function of the silk WL promises a convenient "print-to-pattern" platform for bio-photonics.

In addition to the patterning performance, the compatibility with pattern transferring techniques such as lift-off and ion beam etching is an important benchmark to gauge the applicability of a lithographic process. In this context, metasurfaces consist of micropillars made by liftoff (Figure 27D) and microholes made by ion beam etching (Figure 27E) have been directly fabricated after the silk WL step on freestanding low-loss polyimide substrates. A terahertz time-domain-spectroscopy (THz-TDS) covering the spectral region of 1-5 THz (TAS7500TS, Advantest, Japan) is used to characterize the response of the as-fabricated metasurfaces. The experimentally measured THz transmission spectra (blue curves) shows consistent resonant frequencies with the simulated transmission spectra (red curves), highlighting the quality of the fabricated structures. In addition, parallelized wafer-scale printing is achieved by using multiple printing nozzles which can be controlled and functionalized individually. With the

current setup, 2048 droplets can be dispensed simultaneously and ~10 ms is required for patterning an entire wafer (Figure 27F, G). Another important exemplification of the versatility of the WL process lies in its ability to print on curved surfaces. As shown in Figure 27H, a split ring resonator (SRR) array on the curved surface of a tube has been fabricated using WL process. This non-selectivity of substrate morphology opens up many opportunities for WL in applications that involves non-planar topographies such as tissue scaffold and conformal biomedical devices.

GUIDING AND IMMOBILIZING BIO-COMPOUNDS

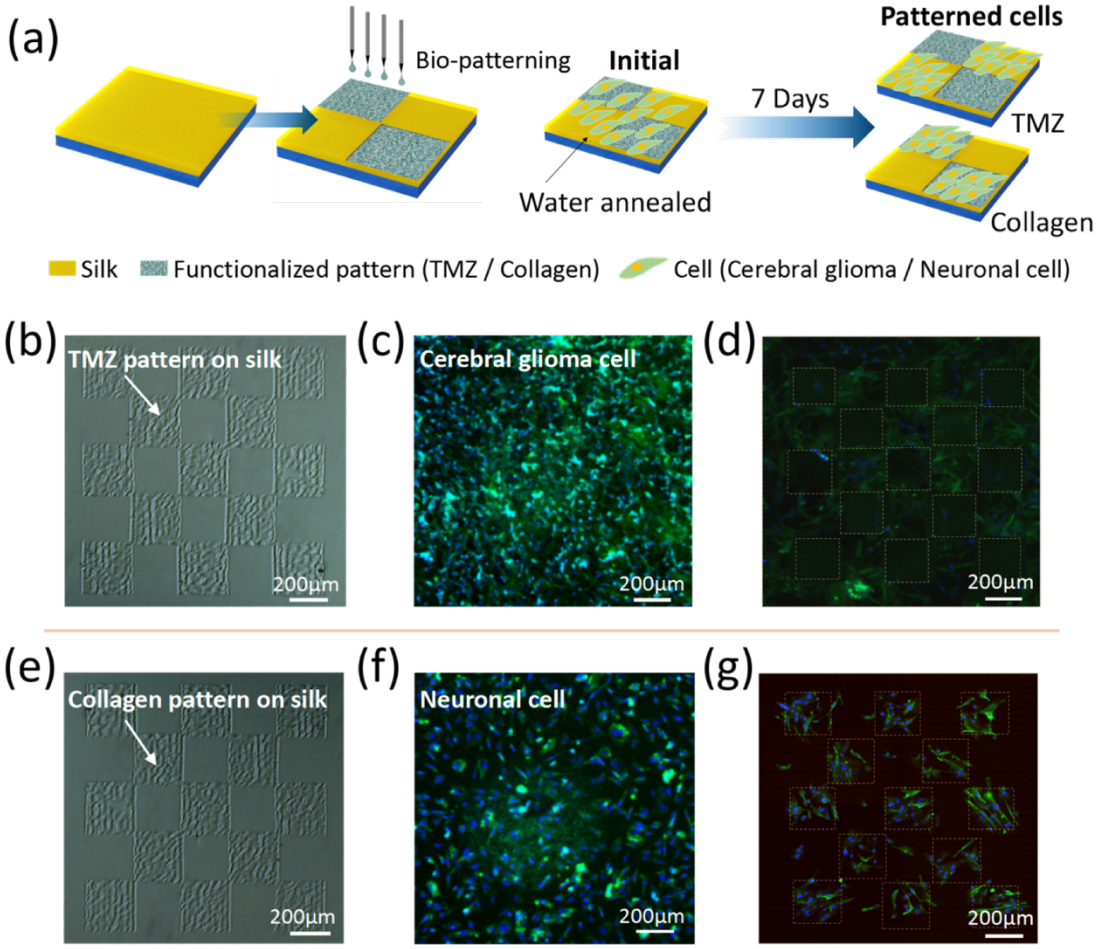

Figure 28: Bioprinting for customizable cell patterning culture based on print-to-pattern WL. (a) Schematic exhibition from customizable drug patterning to cell patterning culture including cerebral glioma cells and neuronal cells on the silk film substrate. (b-d) Cerebral glioma cells cultured on the silk film substrate with drug temozolomide (TMZ). After 7days, the dark-field stereomicroscopic photograph of double immunofluorescence staining with Nestin (green fluorescence) and nuclear staining (blue DAPI staining) of cerebral glioma cells showing patterned cell growth in the shape of checkerboard (the right image, scale bar: 200 μm). (e-g) The neuronal cells patterning growth process on the silk film substrate with rat tail collagen complementary to patterned cerebral glioma (scale bar: 200 μm)..

The power of the silk WL paradigm lies not only in its capability to create controllable geometries, but also the acquirement of functions from dopants that can be embedded into the ink and the silk matrix. Thus the silk WL is an exemplification of a generalized versatile lithography technique, where both shape and functions can be delivered on demand. In addition, the mild fabrication condition (ambient environment) and the usage of bio-friendly materials (only silk and water are involved) of silk WL is inherently compatible with biological applications. The aqueous ink can be functionalized with bio-active components such as collagen (which promotes cell adhesion) and TMZ (which inhibit the growth of cancer cells). As illustrated in the schematic of Figure 28A, the dopants in the ink defines the functionalities of the fabricated patterns to guide cell fates. As a proof-of-concept demonstration, cerebral glioma cells are cultured on a checkerboard-patterned silk substrate using TMZ doped ink (Figure 28B). The glioma cells are the major component of the brain tumor whose inhibition is vital to the alleviation of brain-related disease. As shown in the fluorescence image, the initially casted glioma cells all over the substrate will eventually only survive on the TMZ ink-free area, demonstrating the inhibition capability of the printed TMZ ink (Figure 28C & D). Meanwhile, the promotion of cell growth can be achieved by using the appropriate dopants. As shown in Figure 28E-G, neuronal cells are cultured on silk substrates patterned with collagen doped ink. The fluorescence images show that the cells proliferate and grow in good accordance with the collagen patterns. The silk WL can also be extended to a broad range of biomedical applications including cell-based assays, biosensors, and biochips thanks to its inherent biocompatibility and functional patterning capability.

The silk WL using an IJP framework provides an ideal solution for conveniently dispensing aqueous functional inks to a bio-compatible matrix. Compared to other

conventional fabrication techniques for semiconductor industry, the silk WL is naturally favored for biologically relevant applications. This is partially due to the mild processing conditions for the silk WL where the printing can be conducted in the ambient environment, as opposed to the vacuum requirement for the EBL and IBL. The extensive choice of doping materials (non-toxic and bio- active) for both the ink and the silk matrix contributes to the versatility of this platform to provide functions on the printed structures. The direct material deposition nature of the silk WL also ensures the printed molecules maintain their inherent structures without the influence of high energy particle bombardment (i.e. electrons, ions and photon). Since the water acts as an etchant to the silk film, the development step is achieved simultaneously during the patterning step with a controllable curvature profile. Although the IJP based process suffer from a relatively lower resolution (>5 μm), the feature size is still relevant for biomedical devices. Moreover, with the advancement of electrodynamic jet printing (e-jet printing), submicron-sized patterns can be achieved for applications that requires higher precision. Meanwhile, the parallelization of the printing with multiple nozzles grants the potential for large scale manufacturing.

Despite an IJP process by nature, the silk WL distinguish itself from the conventional IJP, which operates in an additive manner. During the silk WL process, the inks dissolve the silk film and create a hole in the location of landed droplet, featuring a subtractive fabrication mode. This allows a more flexible delivery of materials since both the ink and the silk matrix can contain functional dopants. Thus a dual tone fabrication can be achieved where the fabricated patterns possess a different function from the un-patterned area. The facile incorporation of dopants (such as surfactant) also enables modulation of the hydrophobicity of both the ink and silk matrix, which is crucial for controlling the droplet dynamics during the printing process. In addition, since the silk

protein is a well-known stabilizing agent for a variety of fragile organic and biological materials, the dopants in the ink can maintain their activities in the silk matrix through the dissolution and mixing during the pattern formation. This feature can be multiplexed by the simultaneous printing of multiple types of inks, which grants even more complex functions to the printed structures. The combination of precise placement, ease of control, flexible material choice, mild processing condition and versatile functionalization endows the silk WL with various opportunities in optics, tissue engineering, drug delivery, and implantable devices. This work has been submitted to Advanced Materials.

SUMMARY AND FUTURE DIRECTIONS

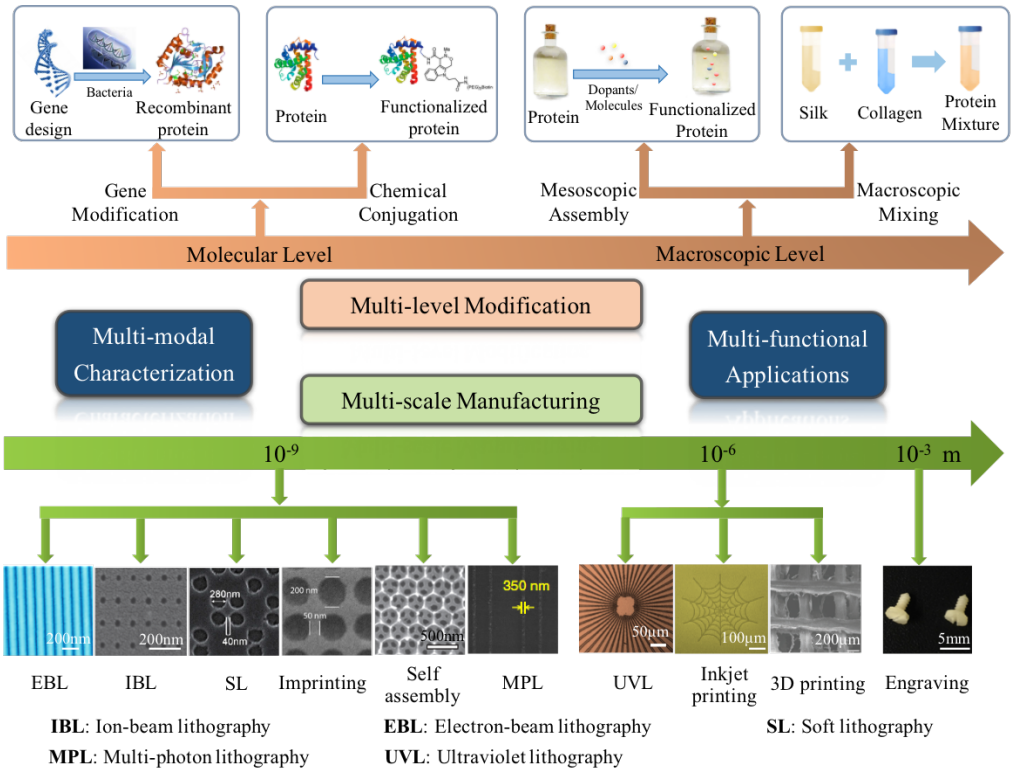

Figure 29: Schematic representation of the strategies used to modify, manufacture and characterize silk materials. (*45, 51, 53, 54, 57, 58, 60, 61, 148*). This work is part of a review paper and has been accepted by Advanced Materials.

After millions of years of evolution, silk fibers have achieved a perfect balance between strength and toughness in a light-weighted and flexible fashion, serving as the critical structural material for the survival of silkworms and spiders. Such mechanical properties have attracted many scientific and commercial efforts to replicate silk fibers for applications beyond their natural function, although challenges still remain to fabricate fibers with comparable mechanical performance. Nevertheless, as a sustainable material, silk - among many other natural biopolymers - holds great promise in a broad

range of scientific, environmental and economic applications that benefit both the people and the planet.

Compared with the long history and wide applications of silk fibroin materials produced by silkworms - because of the cultivation of Bombyx moray silkworms for the industry and being amenable to large-scale manufacturing - the progress on scientific research and commercialization of spider silk relatively fall behind mainly due to difficulties in harvesting large amounts of materials. The territoriality and the cannibalism of the spiders make them difficult to farm and therefore the mass production of spider silk has been impractical. The advancement of biochemical synthesis holds promise on producing increasing volumes of high-quality silk biopolymers with desired mechanical properties and/or biological functionalities after optimizations via a vast amount of explorations.

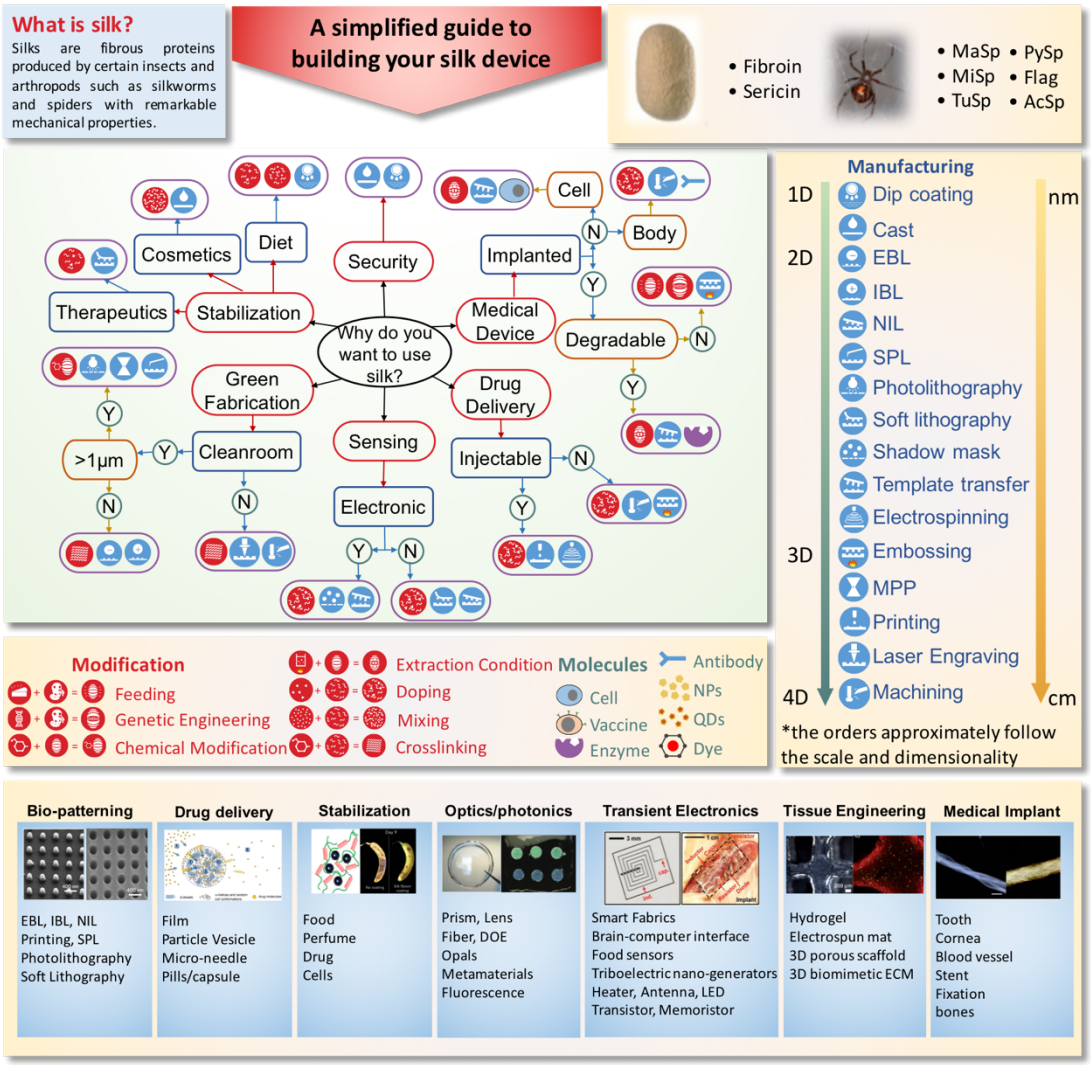

Figure 30: The technological roadmap of "Revolutionary Silk Road". The roadmap serves as a simplified guide that connects the applications of the silk fibroin with the appropriate manufacturing and modification technologies in a systematic manner. The roadmap starts at the center of the figure with an objective of the application, followed by the requirements that needs to be addressed by the manufacturing and modifications of the silk fibroin. The final recommended combinations (the roadmap only listed the most common ones) is summarized in the outmost layer of the figure.[62, 67, 70, 81, 82, 162-165] (*45, 51, 71, 129, 149-153*) Photo credits: (*154*) and spider web (*155*).

Silk was used as a suturing material over a century ago was an early attempt for its entry in biomedical applications. Since then, many research efforts on silk have followed along this direction thanks to its robust mechanical properties, outstanding cytocompatibility, the controllable degradation, and mild aqueous environmental conditions during silk processing. The control of materials properties can be implemented through the control of water content during processing. The modification and functionalization are also achievable at multiple levels ranging from genetic engineering and chemical modification to mesoscale assembly and macroscale mixing. Additionally, silk proteins can be readily formed into a variety of material formats ranging from gels, strands, sponges and blocks, through to foams and films. It offers unlimited opportunities on the creation of multi-functional, hierarchical and heterogeneous structures and devices at multiple scales over orders of magnitudes - ranging from nm to mm and above - with shape and function on demand. We summarize a technological roadmap of "Revolutionary Silk Road" to provide a brief overview of recent developments in silk technology with emphasis on (non-textile) applications including precise bio-patterning, and controlled delivery, bio-optics and bio-photonics, flexible and degradable electronics, tissue engineering and medical implants, enabled by advances in the material modification and structure/device manufacturing (Figure 30). The roadmap serves as a reference that matches applications with the appropriate technology. For example, if a green fabrication process in a cleanroom environment is needed, and required feature size are relatively large, then photolithography, multiphoton lithography, or scanning probe lithography can be applied to the silk protein with the appropriate chemical modification. Similarly, if an implanted solid device is needed, then the silk bulk material doped with the appropriate therapeutic agents can be manufactured through machining. The chart

serves as a simplified guide for connecting the application with the appropriate manufacturing and modification technologies in a systematic manner.

While decent progress has been made on re-empowering silk with more new functionalities while maintaining its advantageous intrinsic properties, the comprehension of certain aspects (such as structure-property relationships and assembly mechanism of natural or engineered silks) of the biological paradigms are still incomplete. Understanding the fundamental biomaterial behavior will indeed continue to move us forward and facilitate bioinspired technology development in many important aspects. For example, silk has been proven as an effective carrier material for enhanced thermos-stability of both antibiotics and vaccines, which could potentially help to save millions of lives each year in developing countries where equipment and procedures used in transport, storage and handling of vaccines - i.e. cold chains - are not readily available. Economically, the revolution of silk could potentially convert the entire silk industry from a currently labor-intensive textile industry with main products on silk yarns, fabrics, garments and carpets into a high-tech and high-value-added one with ground-breaking applications in tissue engineering, regenerative medicine, medical implants, advanced manufacturing and information technology. With the versatile ways of functionalizing, manufacturing, and analyzing this natural material, new properties and applications will be realized with the combinatory research efforts from people in this area.

Reference

1. J. A. Hubbell, Biomaterials in tissue engineering. *Nat. Biotechnol.* **13**, 565-576 (1995).
2. M. Muskovich, C. J. Bettinger, Biomaterials-based electronics: polymers and interfaces for biology and medicine. *Advanced healthcare materials* **1**, 248-266 (2012).
3. C. Vepari, D. L. Kaplan, Silk as a biomaterial. *Prog. Polym. Sci.* **32**, 991-1007 (2007).
4. F. Nudelman, K. Pieterse, A. George, P. H. Bomans, H. Friedrich, L. J. Brylka, P. A. Hilbers, N. A. Sommerdijk, The role of collagen in bone apatite formation in the presence of hydroxyapatite nucleation inhibitors. *Nature materials* **9**, 1004 (2010).
5. C. W. P. Foo, D. L. Kaplan, Genetic engineering of fibrous proteins: spider dragline silk and collagen. *Adv. Drug Del. Rev.* **54**, 1131-1143 (2002).
6. C.-Z. Zhou, F. Confalonieri, N. Medina, Y. Zivanovic, C. Esnault, T. Yang, M. Jacquet, J. Janin, M. Duguet, R. Perasso, Fine organization of Bombyx mori fibroin heavy chain gene. *Nucleic Acids Res.* **28**, 2413-2419 (2000).
7. K. Yamaguchi, Y. Kikuchi, T. Takagi, A. Kikuchi, F. Oyama, K. Shimura, S. Mizuno, Primary structure of the silk fibroin light chain determined by cDNA sequencing and peptide analysis. *J. Mol. Biol.* **210**, 127-139 (1989).
8. S. Inoue, K. Tanaka, F. Arisaka, S. Kimura, K. Ohtomo, S. Mizuno, Silk fibroin of Bombyx mori is secreted, assembling a high molecular mass elementary unit consisting of H-chain, L-chain, and P25, with a 6: 6: 1 molar ratio. *J. Biol. Chem.* **275**, 40517-40528 (2000).
9. E. Bini, D. P. Knight, D. L. Kaplan, Mapping domain structures in silks from insects and spiders related to protein assembly. *J. Mol. Biol.* **335**, 27-40 (2004).
10. C. Z. Zhou, F. Confalonieri, M. Jacquet, R. Perasso, Z. G. Li, J. Janin, Silk fibroin: structural implications of a remarkable amino acid sequence. *Proteins: Structure, Function, and Bioinformatics* **44**, 119-122 (2001).
11. L. P. Gage, R. Manning, Internal structure of the silk fibroin gene of Bombyx mori. I The fibroin gene consists of a homogeneous alternating array of repetitious crystalline and amorphous coding sequences. *J. Biol. Chem.* **255**, 9444-9450 (1980).
12. S. Keten, Z. Xu, B. Ihle, M. J. Buehler, Nanoconfinement controls stiffness, strength and mechanical toughness of β-sheet crystals in silk. *Nature materials* **9**, 359 (2010).
13. C. Jiang, X. Wang, R. Gunawidjaja, Y. H. Lin, M. K. Gupta, D. L. Kaplan, R. R. Naik, V. V. Tsukruk, Mechanical properties of robust ultrathin silk fibroin films. *Adv. Funct. Mater.* **17**, 2229-2237 (2007).
14. M. B. Dickerson, S. P. Fillery, H. Koerner, K. M. Singh, K. Martinick, L. F. Drummy, M. F. Durstock, R. A. Vaia, F. G. Omenetto, D. L. Kaplan, Dielectric

breakdown strength of regenerated silk fibroin films as a function of protein conformation. *Biomacromolecules* **14**, 3509-3514 (2013).
15. J. Pérez-Rigueiro, C. Viney, J. Llorca, M. Elices, Mechanical properties of single-brin silkworm silk. *J. Appl. Polym. Sci.* **75**, 1270-1277 (2000).
16. P. M. Cunniff, S. A. Fossey, M. A. Auerbach, J. W. Song, D. L. Kaplan, W. W. Adams, R. K. Eby, D. Mahoney, D. L. Vezie, Mechanical and thermal properties of dragline silk from the spider Nephila clavipes. *Polym. Adv. Technol.* **5**, 401-410 (1994).
17. G. D. Pins, D. L. Christiansen, R. Patel, F. H. Silver, Self-assembly of collagen fibers. Influence of fibrillar alignment and decorin on mechanical properties. *Biophys. J.* **73**, 2164-2172 (1997).
18. I. Engelberg, J. Kohn, Physico-mechanical properties of degradable polymers used in medical applications: a comparative study. *Biomaterials* **12**, 292-304 (1991).
19. A. Schneider, X. Wang, D. Kaplan, J. Garlick, C. Egles, Biofunctionalized electrospun silk mats as a topical bioactive dressing for accelerated wound healing. *Acta Biomater.* **5**, 2570-2578 (2009).
20. Y. Shen, S. L. Redmond, J. M. Papadimitriou, B. M. Teh, S. Yan, Y. Wang, M. D. Atlas, R. J. Marano, M. Zheng, R. J. Dilley, The biocompatibility of silk fibroin and acellular collagen scaffolds for tissue engineering in the ear. *Biomedical Materials* **9**, 015015 (2014).
21. X. Zhang, M. R. Reagan, D. L. Kaplan, Electrospun silk biomaterial scaffolds for regenerative medicine. *Adv. Drug Del. Rev.* **61**, 988-1006 (2009).
22. E. M. Pritchard, X. Hu, V. Finley, C. K. Kuo, D. L. Kaplan, Effect of silk protein processing on drug delivery from silk films. *Macromol. Biosci.* **13**, 311-320 (2013).
23. G. H. Altman, F. Diaz, C. Jakuba, T. Calabro, R. L. Horan, J. Chen, H. Lu, J. Richmond, D. L. Kaplan, Silk-based biomaterials. *Biomaterials* **24**, 401-416 (2003).
24. L. Cen, W. Liu, L. Cui, W. Zhang, Y. Cao, Collagen tissue engineering: development of novel biomaterials and applications. *Pediatr. Res.* **63**, 492 (2008).
25. P. Hill, H. Brantley, M. Van Dyke, Some properties of keratin biomaterials: kerateines. *Biomaterials* **31**, 585-593 (2010).
26. D. F. Williams, There is no such thing as a biocompatible material. *Biomaterials* **35**, 10009-10014 (2014).
27. D. F. Williams, On the mechanisms of biocompatibility. *Biomaterials* **29**, 2941-2953 (2008).
28. N. Rajan, J. Habermehl, M.-F. Coté, C. J. Doillon, D. Mantovani, Preparation of ready-to-use, storable and reconstituted type I collagen from rat tail tendon for tissue engineering applications. *Nat. Protoc.* **1**, 2753 (2006).
29. H. Tao, D. L. Kaplan, F. G. Omenetto, Silk materials–a road to sustainable high technology. *Adv. Mater.* **24**, 2824-2837 (2012).

30. D. N. Rockwood, R. C. Preda, T. Yücel, X. Wang, M. L. Lovett, D. L. Kaplan, Materials fabrication from Bombyx mori silk fibroin. *Nat. Protoc.* **6**, 1612-1631 (2011).
31. J. Jiang, S. Zhang, N. Qin, Z. Zhou, X. Xia, H. Tao, K. Liu, in *Micro Electro Mechanical Systems (MEMS), 2017 IEEE 30th International Conference on*. (IEEE, 2017), pp. 255-257.
32. E. M. Pritchard, T. Valentin, B. Panilaitis, F. Omenetto, D. L. Kaplan, Antibiotic-Releasing Silk Biomaterials for Infection Prevention and Treatment. *Adv. Funct. Mater.* **23**, 854-861 (2013).
33. W. Wei, Y. Zhang, Y. Zhao, J. Luo, H. Shao, X. Hu, Bio-inspired capillary dry spinning of regenerated silk fibroin aqueous solution. *Materials Science and Engineering: C* **31**, 1602-1608 (2011).
34. L. S. Wray, X. Hu, J. Gallego, I. Georgakoudi, F. G. Omenetto, D. Schmidt, D. L. Kaplan, Effect of processing on silk-based biomaterials: Reproducibility and biocompatibility. *Journal of Biomedical Materials Research Part B: Applied Biomaterials* **99**, 89-101 (2011).
35. L. Eisoldt, A. Smith, T. Scheibel, Decoding the secrets of spider silk. *Mater. Today* **14**, 80-86 (2011).
36. X.-X. Xia, Z.-G. Qian, C. S. Ki, Y. H. Park, D. L. Kaplan, S. Y. Lee, Native-sized recombinant spider silk protein produced in metabolically engineered Escherichia coli results in a strong fiber. *Proceedings of the National Academy of Sciences* **107**, 14059-14063 (2010).
37. F. Teulé, A. R. Cooper, W. A. Furin, D. Bittencourt, E. L. Rech, A. Brooks, R. V. Lewis, A protocol for the production of recombinant spider silk-like proteins for artificial fiber spinning. *Nat. Protoc.* **4**, 341 (2009).
38. A. Lazaris, S. Arcidiacono, Y. Huang, J.-F. Zhou, F. Duguay, N. Chretien, E. A. Welsh, J. W. Soares, C. N. Karatzas, Spider silk fibers spun from soluble recombinant silk produced in mammalian cells. *Science* **295**, 472-476 (2002).
39. O. Tokareva, V. A. Michalczechen-Lacerda, E. L. Rech, D. L. Kaplan, Recombinant DNA production of spider silk proteins. *Microbial biotechnology* **6**, 651-663 (2013).
40. D. W. Kim, O. J. Lee, S.-W. Kim, C. S. Ki, J. R. Chao, H. Yoo, S.-i. Yoon, J. E. Lee, Y. R. Park, H. Kweon, Novel fabrication of fluorescent silk utilized in biotechnological and medical applications. *Biomaterials* **70**, 48-56 (2015).
41. M. Humenik, M. Drechsler, T. Scheibel, Controlled hierarchical assembly of spider silk-DNA chimeras into ribbons and raft-like morphologies. *Nano Lett.* **14**, 3999-4004 (2014).
42. W. Liu, Z. Zhou, S. Zhang, Z. Shi, J. Tabarini, W. Lee, Y. Zhang, S. Gilbert Corder, X. Li, F. Dong, Precise Protein Photolithography (P3): High Performance Biopatterning Using Silk Fibroin Light Chain as the Resist. *Advanced Science* **4**, (2017).
43. C. Vepari, D. Matheson, L. Drummy, R. Naik, D. L. Kaplan, Surface modification of silk fibroin with poly (ethylene glycol) for antiadhesion and

antithrombotic applications. *Journal of biomedical materials research Part A* **93**, 595-606 (2010).
44. K. Cai, K. Yao, S. Lin, Z. Yang, X. Li, H. Xie, T. Qing, L. Gao, Poly (D, L-lactic acid) surfaces modified by silk fibroin: effects on the culture of osteoblast in vitro. *Biomaterials* **23**, 1153-1160 (2002).
45. S. Kim, B. Marelli, M. A. Brenckle, A. N. Mitropoulos, E.-S. Gil, K. Tsioris, H. Tao, D. L. Kaplan, F. G. Omenetto, All-water-based electron-beam lithography using silk as a resist. *Nature nanotechnology* **9**, 306-310 (2014).
46. N. Qin, S. Zhang, J. Jiang, S. G. Corder, Z. Qian, Z. Zhou, W. Lee, K. Liu, X. Wang, X. Li, Nanoscale probing of electron-regulated structural transitions in silk proteins by near-field IR imaging and nano-spectroscopy. *Nature communications* **7**, (2016).
47. H. Perry, A. Gopinath, D. L. Kaplan, L. Dal Negro, F. G. Omenetto, Nano- and Micropatterning of Optically Transparent, Mechanically Robust, Biocompatible Silk Fibroin Films &dagger. *Adv. Mater.* **20**, 3070-3072 (2010).
48. Z. Zhou, Z. Shi, X. Cai, S. Zhang, S. G. Corder, X. Li, Y. Zhang, G. Zhang, L. Chen, M. Liu, The Use of Functionalized Silk Fibroin Films as a Platform for Optical Diffraction-Based Sensing Applications. *Adv. Mater.* **29**, (2017).
49. J. P. Mondia, J. J. Amsden, D. Lin, L. D. Negro, D. L. Kaplan, F. G. Omenetto, Rapid nanoimprinting of doped silk films for enhanced fluorescent emission. *Adv. Mater.* **22**, 4596-4599 (2010).
50. M. A. Brenckle, H. Tao, S. Kim, M. Paquette, D. L. Kaplan, F. G. Omenetto, Protein-Protein Nanoimprinting of Silk Fibroin Films. *Adv. Mater.* **25**, 2409-2414 (2013).
51. S. Kim, A. N. Mitropoulos, J. D. Spitzberg, T. Hu, D. L. Kaplan, F. G. Omenetto, Silk inverse opals. *Nature Photonics* **6**, 818-823 (2012).
52. Y. Wang, D. Aurelio, W. Li, P. Tseng, Z. Zheng, M. Li, D. L. Kaplan, M. Liscidini, F. G. Omenetto, Modulation of Multiscale 3D Lattices through Conformational Control: Painting Silk Inverse Opals with Water and Light. *Adv. Mater.* **29**, (2017).
53. Y.-L. Sun, Q. Li, S.-M. Sun, J.-C. Huang, B.-Y. Zheng, Q.-D. Chen, Z.-Z. Shao, H.-B. Sun, Aqueous multiphoton lithography with multifunctional silk-centred bio-resists. *Nature communications* **6**, (2015).
54. W. Liu, Z. Zhou, S. Zhang, Z. Shi, J. Tabarini, W. Lee, Y. Zhang, S. Gilbert Corder, X. Li, F. Dong, L. Cheng, M. Liu, D. L. Kaplan, F. Omenetto, G. Zhang, Y. Mao, T. H. Tao, Precise Protein Photolithography (P3): High Performance Biopatterning Using Silk Fibroin Light Chain as the Resist. *Advanced Science*, (2017).
55. N. E. Kurland, T. Dey, S. C. Kundu, V. K. Yadavalli, Precise patterning of silk microstructures using photolithography. *Adv. Mater.* **25**, 6207-6212 (2013).
56. H. Tao, B. Marelli, M. Yang, B. An, D. Kaplan, F. Omenetto, in *Solid-State Sensors, Actuators and Microsystems (TRANSDUCERS), 2015 Transducers-2015 18th International Conference on*. (IEEE, 2015), pp. 518-520.

57. H. Tao, B. Marelli, M. Yang, B. An, M. S. Onses, J. A. Rogers, D. L. Kaplan, F. G. Omenetto, Inkjet printing of regenerated silk fibroin: From printable forms to printable functions. *Adv. Mater.* **27**, 4273-4279 (2015).
58. C. Li, B. Hotz, S. Ling, J. Guo, D. S. Haas, B. Marelli, F. Omenetto, S. J. Lin, D. L. Kaplan, Regenerated silk materials for functionalized silk orthopedic devices by mimicking natural processing. *Biomaterials* **110**, 24-33 (2016).
59. D. Lin, H. Tao, J. Trevino, J. P. Mondia, D. L. Kaplan, F. G. Omenetto, L. Dal Negro, Direct transfer of subwavelength plasmonic nanostructures on bioactive silk films. *Adv. Mater.* **24**, 6088-6093 (2012).
60. M. A. Brenckle, H. Tao, S. Kim, M. Paquette, D. L. Kaplan, F. G. Omenetto, Protein-protein nanoimprinting of silk fibroin films. *Adv. Mater.* **25**, 2378-2378 (2013).
61. J. J. Amsden, P. Domachuk, A. Gopinath, R. D. White, L. D. Negro, D. L. Kaplan, F. G. Omenetto, Rapid nanoimprinting of silk fibroin films for biophotonic applications. *Adv. Mater.* **22**, 1746-1749 (2010).
62. G. Ding, Q. Jin, Q. Chen, Z. Hu, J. Liu, The fabrication of ordered bulk heterojunction solar cell by nanoimprinting lithography method using patterned silk fibroin mold at room temperature. *Nanoscale research letters* **10**, 491 (2015).
63. J. Zhong, M. Ma, J. Zhou, D. Wei, Z. Yan, D. He, Tip-induced micropatterning of silk fibroin protein using in situ solution atomic force microscopy. *ACS applied materials & interfaces* **5**, 737-746 (2013).
64. N. Lin, G. W. Toh, Y. Feng, X. Liu, H. Xu, Two-photon fluorescent Bombyx mori silk by molecular recognition functionalization. *Journal of Materials Chemistry B* **2**, 2136-2143 (2014).
65. H. Tao, M. A. Brenckle, M. Yang, J. Zhang, M. Liu, S. M. Siebert, R. D. Averitt, M. S. Mannoor, M. C. McAlpine, J. A. Rogers, Silk-Based Conformal, Adhesive, Edible Food Sensors. *Adv. Mater.* **24**, 1067-1072 (2012).
66. P. Tseng, B. Napier, S. Zhao, A. N. Mitropoulos, M. B. Applegate, B. Marelli, D. L. Kaplan, F. G. Omenetto, Directed assembly of bio-inspired hierarchical materials with controlled nanofibrillar architectures. *Nature Nanotechnology* **12**, 474-480 (2017).
67. A. Elliott, E. Ambrose, Structure of synthetic polypeptides. *Nature* **165**, 921 (1950).
68. S. Krimm, J. Bandekar, in *Adv. Protein Chem.* (Elsevier, 1986), vol. 38, pp. 181-364.
69. J. Bandekar, Amide modes and protein conformation. *Biochimica et Biophysica Acta (BBA)-Protein Structure and Molecular Enzymology* **1120**, 123-143 (1992).
70. T. Miyazawa, T. Shimanouchi, S. i. Mizushima, Characteristic infrared bands of monosubstituted amides. *The Journal of Chemical Physics* **24**, 408-418 (1956).
71. F. G. Omenetto, D. L. Kaplan, A new route for silk. *Nature Photonics* **2**, 641-643 (2008).
72. F. G. Omenetto, D. L. Kaplan, New opportunities for an ancient material. *Science* **329**, 528-531 (2010).

73. Z. Fei, A. Rodin, G. Andreev, W. Bao, A. McLeod, M. Wagner, L. Zhang, Z. Zhao, M. Thiemens, G. Dominguez, Gate-tuning of graphene plasmons revealed by infrared nano-imaging. *Nature* **487**, 82-85 (2012).
74. M. M. Qazilbash, M. Brehm, B.-G. Chae, P.-C. Ho, G. O. Andreev, B.-J. Kim, S. J. Yun, A. Balatsky, M. Maple, F. Keilmann, Mott transition in VO2 revealed by infrared spectroscopy and nano-imaging. *Science* **318**, 1750-1753 (2007).
75. H. A. Bechtel, E. A. Muller, R. L. Olmon, M. C. Martin, M. B. Raschke, Ultrabroadband infrared nanospectroscopic imaging. *Proceedings of the National Academy of Sciences* **111**, 7191-7196 (2014).
76. I. Amenabar, S. Poly, W. Nuansing, E. H. Hubrich, A. A. Govyadinov, F. Huth, R. Krutokhvostov, L. Zhang, M. Knez, J. Heberle, Structural analysis and mapping of individual protein complexes by infrared nanospectroscopy. *Nature communications* **4**, (2013).
77. F. Ruggeri, G. Longo, S. Faggiano, E. Lipiec, A. Pastore, G. Dietler, Infrared nanospectroscopy characterization of oligomeric and fibrillar aggregates during amyloid formation. *Nature communications* **6**, 7831 (2015).
78. M. Paulite, Z. Fakhraai, I. T. Li, N. Gunari, A. E. Tanur, G. C. Walker, Imaging secondary structure of individual amyloid fibrils of a β 2-microglobulin fragment using near-field infrared spectroscopy. *JACS* **133**, 7376-7383 (2011).
79. F. Huth, A. Govyadinov, S. Amarie, W. Nuansing, F. Keilmann, R. Hillenbrand, Nano-FTIR absorption spectroscopy of molecular fingerprints at 20 nm spatial resolution. *Nano Lett*. **12**, 3973-3978 (2012).
80. S. Mastel, A. A. Govyadinov, T. V. de Oliveira, I. Amenabar, R. Hillenbrand, Nanoscale-resolved chemical identification of thin organic films using infrared near-field spectroscopy and standard Fourier transform infrared references. *Appl. Phys. Lett*. **106**, 023113 (2015).
81. N. Ocelic, A. Huber, R. Hillenbrand, Pseudoheterodyne detection for background-free near-field spectroscopy. *Appl. Phys. Lett*. **89**, 101124 (2006).
82. A. A. Govyadinov, I. Amenabar, F. Huth, P. S. Carney, R. Hillenbrand, Quantitative measurement of local infrared absorption and dielectric function with tip-enhanced near-field microscopy. *The journal of physical chemistry letters* **4**, 1526-1531 (2013).
83. N. Ocelic, Technische Universität München, (2007).
84. X. G. Xu, A. E. Tanur, G. C. Walker, Phase controlled homodyne infrared near-field microscopy and spectroscopy reveal inhomogeneity within and among individual boron nitride nanotubes. *The Journal of Physical Chemistry A* **117**, 3348-3354 (2013).
85. X. G. Xu, L. Gilburd, G. C. Walker, Phase stabilized homodyne of infrared scattering type scanning near-field optical microscopy. *Appl. Phys. Lett*. **105**, 263104 (2014).
86. E. Yoxall, M. Schnell, S. Mastel, R. Hillenbrand, Magnitude and phase-resolved infrared vibrational nanospectroscopy with a swept quantum cascade laser. *Opt. Express* **23**, 13358-13369 (2015).

87. A. C. Jones, M. B. Raschke, Thermal infrared near-field spectroscopy. *Nano Lett.* **12**, 1475-1481 (2012).
88. A. Dazzi, C. B. Prater, Q. Hu, D. B. Chase, J. F. Rabolt, C. Marcott, AFM–IR: combining atomic force microscopy and infrared spectroscopy for nanoscale chemical characterization. *Appl. Spectrosc.* **66**, 1365-1384 (2012).
89. T. Hassenkam, M. Andersson, K. Dalby, D. Mackenzie, M. Rosing, Elements of Eoarchean life trapped in mineral inclusions. *Nature* **548**, 78-81 (2017).
90. G. Zandomeneghi, M. R. Krebs, M. G. McCammon, M. Fändrich, FTIR reveals structural differences between native β-sheet proteins and amyloid fibrils. *Protein Sci.* **13**, 3314-3321 (2004).
91. M. Jackson, H. H. Mantsch, The use and misuse of FTIR spectroscopy in the determination of protein structure. *Crit. Rev. Biochem. Mol. Biol.* **30**, 95-120 (1995).
92. M. Calero, M. Gasset, Featuring amyloids with Fourier transform infrared and circular dichroism spectroscopies. *Amyloid Proteins: Methods and Protocols*, 53-68 (2012).
93. X. Hu, D. Kaplan, P. Cebe, Determining beta-sheet crystallinity in fibrous proteins by thermal analysis and infrared spectroscopy. *Macromolecules* **39**, 6161-6170 (2006).
94. R. Pease, Electron beam lithography. *Contemporary Physics* **22**, 265-290 (1981).
95. S. Zhang, N. Qin, T. H. Tao, in *Micro Electro Mechanical Systems (MEMS), 2017 IEEE 30th International Conference on*. (IEEE, 2017), pp. 724-727.
96. K. Tsioris, W. K. Raja, E. M. Pritchard, B. Panilaitis, D. L. Kaplan, F. G. Omenetto, Fabrication of Silk Microneedles for Controlled-Release Drug Delivery. *Adv. Funct. Mater.* **22**, 330-335 (2012).
97. S. Bai, S. Liu, C. Zhang, W. Xu, Q. Lu, H. Han, D. Kaplan, H. Zhu, Controllable transition of silk fibroin nanostructures: an insight into in vitro silk self-assembly process. *Acta Biomater.* **9**, 7806-7813 (2013).
98. Y. Shi, X. Li, G. Ding, Y. Wu, Y. Weng, Z. Hu, Control of β-sheet crystal orientation and elastic modulus in silk protein by nanoconfinement. *Macromolecules* **47**, 7987-7992 (2014).
99. P. Cebe, X. Hu, D. L. Kaplan, E. Zhuravlev, A. Wurm, D. Arbeiter, C. Schick, Beating the heat-fast scanning melts silk beta sheet crystals. *Sci. Rep.* **3**, 1130 (2013).
100. S. Y. Cho, Y. S. Yun, S. Lee, D. Jang, K. Y. Park, J. K. Kim, B. H. Kim, K. Kang, D. L. Kaplan, H. J. Jin, Carbonization of a stable β-sheet-rich silk protein into a pseudographitic pyroprotein. *Nature Communications* **6**, 7145 (2015).
101. Y. S. Yun, K. Y. Park, B. Lee, S. Y. Cho, Y. U. Park, S. J. Hong, B. H. Kim, H. Gwon, H. Kim, S. Lee, Sodium-ion storage in pyroprotein-based carbon nanoplates. *Adv. Mater.* **27**, 6914-6921 (2015).

102. S.-J. Byun, H. Lim, G.-Y. Shin, T.-H. Han, S. H. Oh, J.-H. Ahn, H. C. Choi, T.-W. Lee, Graphenes converted from polymers. *The Journal of Physical Chemistry Letters* **2**, 493-497 (2011).
103. X. Liu, S. Wang, Three-dimensional nano-biointerface as a new platform for guiding cell fate. *Chem. Soc. Rev.* **43**, 2385-2401 (2014).
104. A. Kabashin, P. Evans, S. Pastkovsky, W. Hendren, G. Wurtz, R. Atkinson, R. Pollard, V. Podolskiy, A. Zayats, Plasmonic nanorod metamaterials for biosensing. *Nature materials* **8**, 867-871 (2009).
105. M. Lutolf, J. Hubbell, Synthetic biomaterials as instructive extracellular microenvironments for morphogenesis in tissue engineering. *Nat. Biotechnol.* **23**, 47-55 (2005).
106. J. B. Matson, S. I. Stupp, Self-assembling peptide scaffolds for regenerative medicine. *Chem. Commun.* **48**, 26-33 (2012).
107. Y. Greenzweig, Y. Drezner, S. Tan, R. H. Livengood, A. Raveh, Current density profile characterization and analysis method for focused ion beam. *Microelectron. Eng.* **155**, 19-24 (2016).
108. N. E. Kurland, T. Dey, C. Wang, S. C. Kundu, V. K. Yadavalli, Silk Protein Lithography as a Route to Fabricate Sericin Microarchitectures. *Adv. Mater.* **26**, 4431-4437 (2014).
109. K. Shimura, A. Kikuchi, K. Ohtomo, Y. KATAGATA, A. Hyodo, Studies on silk fibroin of Bombyx mori. I. Fractionation of fibroin prepared from the posterior silk gland. *The Journal of Biochemistry* **80**, 693-702 (1976).
110. K. Tanaka, S. Inoue, S. Mizuno, Hydrophobic interaction of P25, containing Asn-linked oligosaccharide chains, with the HL complex of silk fibroin produced by Bombyx mori. *Insect Biochem. Mol. Biol.* **29**, 269-276 (1999).
111. K. Tanaka, N. Kajiyama, K. Ishikura, S. Waga, A. Kikuchi, K. Ohtomo, T. Takagi, S. Mizuno, Determination of the site of disulfide linkage between heavy and light chains of silk fibroin produced by Bombyx mori. *Biochimica et Biophysica Acta (BBA)-Protein Structure and Molecular Enzymology* **1432**, 92-103 (1999).
112. P. Wadbua, B. Promdonkoy, S. Maensiri, S. Siri, Different properties of electrospun fibrous scaffolds of separated heavy-chain and light-chain fibroins of Bombyx mori. *Int. J. Biol. Macromol.* **46**, 493-501 (2010).
113. T. Witten Jr, L. M. Sander, Diffusion-limited aggregation, a kinetic critical phenomenon. *Phys. Rev. Lett.* **47**, 1400 (1981).
114. G. Reiter, I. Botiz, L. Graveleau, N. Grozev, K. Albrecht, A. Mourran, M. Möller, in *Progress in Understanding of Polymer Crystallization*. (Springer, 2007), pp. 179-200.
115. A. Lomander, W. Hwang, S. Zhang, Hierarchical self-assembly of a coiled-coil peptide into fractal structure. *Nano Lett.* **5**, 1255-1260 (2005).
116. R. Sneer, M. J. Weygand, K. Kjaer, D. A. Tirrell, H. Rapaport, Parallel β-Sheet Assemblies at Interfaces. *Chemphyschem* **5**, 747-750 (2004).

117. M. M. Murr, D. E. Morse, Fractal intermediates in the self-assembly of silicatein filaments. *Proc. Natl. Acad. Sci. U.S.A.* **102**, 11657-11662 (2005).
118. O. S. Kumru, S. B. Joshi, D. E. Smith, C. R. Middaugh, T. Prusik, D. B. Volkin, Vaccine instability in the cold chain: mechanisms, analysis and formulation strategies. *Biologicals* **42**, 237-259 (2014).
119. K. Martinek, A. Klibanov, V. Goldmacher, A. Tchernysheva, V. Mozhaev, I. Berezin, B. Glotov, The principles of enzyme stabilization: II. Increase in the thermostability of enzymes as a result of multipoint noncovalent interaction with a polymeric support. *Biochimica et Biophysica Acta (BBA)-Enzymology* **485**, 13-28 (1977).
120. E. Cheriyan, Monitoring the vaccine cold chain. *Arch. Dis. Child.* **69**, 600-601 (1993).
121. W. J. McAleer, H. Z. Markus, A. A. McLean, E. B. Buynak, M. R. Hilleman, Stability on storage at various temperatures of live measles, mumps and rubella virus vaccines in new stabilizer. *J. Biol. Stand.* **8**, 281-287 (1980).
122. T. D. Sutherland, A. Sriskantha, J. S. Church, T. Strive, H. E. Trueman, T. Kameda, Stabilization of viruses by encapsulation in silk proteins. *ACS applied materials & interfaces* **6**, 18189-18196 (2014).
123. A. B. Li, J. A. Kluge, N. A. Guziewicz, F. G. Omenetto, D. L. Kaplan, Silk-based stabilization of biomacromolecules. *J. Controlled Release* **219**, 416-430 (2015).
124. A. B. Li, J. A. Kluge, M. Zhi, M. T. Cicerone, F. G. Omenetto, D. L. Kaplan, Enhanced Stabilization in Dried Silk Fibroin Matrices. *Biomacromolecules* **18**, 2900-2905 (2017).
125. N. A. Guziewicz, A. J. Massetti, B. J. Perez-Ramirez, D. L. Kaplan, Mechanisms of monoclonal antibody stabilization and release from silk biomaterials. *Biomaterials* **34**, 7766-7775 (2013).
126. L. Zhang, C. Herrera, J. Coburn, N. Olejniczak, P. Ziprin, D. L. Kaplan, P. J. LiWang, Stabilization and sustained release of HIV inhibitors by encapsulation in silk fibroin disks. *ACS Biomaterials Science & Engineering* **3**, 1654-1665 (2017).
127. B. D. Lawrence, M. Cronin-Golomb, I. Georgakoudi, D. L. Kaplan, F. G. Omenetto, Bioactive silk protein biomaterial systems for optical devices. *Biomacromolecules* **9**, 1214-1220 (2008).
128. Q. Lu, X. Wang, X. Hu, P. Cebe, F. Omenetto, D. L. Kaplan, Stabilization and release of enzymes from silk films. *Macromol. Biosci.* **10**, 359-368 (2010).
129. J. Zhang, E. Pritchard, X. Hu, T. Valentin, B. Panilaitis, F. G. Omenetto, D. L. Kaplan, Stabilization of vaccines and antibiotics in silk and eliminating the cold chain. *Proceedings of the National Academy of Sciences* **109**, 11981-11986 (2012).
130. E. M. Pritchard, P. B. Dennis, F. Omenetto, R. R. Naik, D. L. Kaplan, Physical and chemical aspects of stabilization of compounds in silk. *Biopolymers* **97**, 479-498 (2012).
131. W. Jiskoot, T. W. Randolph, D. B. Volkin, C. R. Middaugh, C. Schöneich, G. Winter, W. Friess, D. J. Crommelin, J. F. Carpenter, Protein instability and

immunogenicity: roadblocks to clinical application of injectable protein delivery systems for sustained release. *J. Pharm. Sci.* **101**, 946-954 (2012).
132. P. Privalov, in *Adv. Protein Chem.* (Elsevier, 1982), vol. 35, pp. 1-104.
133. R. Jaenicke, Stability and stabilization of globular proteins in solution. *J. Biotechnol.* **79**, 193-203 (2000).
134. B. Perez-Ramirez, N. Guziewicz, R. Simler, Preformulation research: assessing protein solution behavior during early development. *Formulation and Process Development Strategies for Manufacturing Biopharmaceuticals*, 119-146 (2010).
135. E. Y. Chi, S. Krishnan, T. W. Randolph, J. F. Carpenter, Physical stability of proteins in aqueous solution: mechanism and driving forces in nonnative protein aggregation. *Pharm. Res.* **20**, 1325-1336 (2003).
136. S. N. Timasheff, Control of protein stability and reactions by weakly interacting cosolvents: the simplicity of the complicated. *Adv. Protein Chem* **51**, 355-432 (1998).
137. M. C. Manning, D. K. Chou, B. M. Murphy, R. W. Payne, D. S. Katayama, Stability of protein pharmaceuticals: an update. *Pharm. Res.* **27**, 544-575 (2010).
138. K. Patel, R. T. Borchardt, Chemical pathways of peptide degradation. II. Kinetics of deamidation of an asparaginyl residue in a model hexapeptide. *Pharm. Res.* **7**, 703-711 (1990).
139. T. Arakawa, S. N. Timasheff, Stabilization of protein structure by sugars. *Biochemistry* **21**, 6536-6544 (1982).
140. J. C. Lee, S. N. Timasheff, The stabilization of proteins by sucrose. *J. Biol. Chem.* **256**, 7193-7201 (1981).
141. S. Shimizu, D. J. Smith, Preferential hydration and the exclusion of cosolvents from protein surfaces. *The Journal of chemical physics* **121**, 1148-1154 (2004).
142. J. F. Carpenter, J. H. Crowe, Modes of stabilization of a protein by organic solutes during desiccation. *Cryobiology* **25**, 459-470 (1988).
143. F. Franks, Materials science and the production of shelf stable biologicals. *BioPharm*, 38-42 (1991).
144. G. Vassart, M. Georges, R. Monsieur, H. Brocas, A. S. Lequarre, D. Christophe, A sequence in M13 phage detects hypervariable minisatellites in human and animal DNA. *Science* **235**, 683-684 (1987).
145. D. Marvin, Filamentous phage structure, infection and assembly. *Curr. Opin. Struct. Biol.* **8**, 150-158 (1998).
146. P. Rider, Y. Zhang, C. Tse, Y. Zhang, D. Jayawardane, J. Stringer, J. Callaghan, I. Brook, C. A. Miller, X. Zhao, Biocompatible silk fibroin scaffold prepared by reactive inkjet printing. *Journal of Materials Science* **51**, 8625-8630 (2016).
147. B. J. de Gans, P. C. Duineveld, U. S. Schubert, Inkjet printing of polymers: state of the art and future developments. *Adv. Mater.* **16**, 203-213 (2004).
148. W. Shi, M. Sun, X. Hu, B. Ren, J. Cheng, C. Li, X. Duan, X. Fu, J. Zhang, H. Chen, Structurally and Functionally Optimized Silk-Fibroin–Gelatin Scaffold Using 3D Printing to Repair Cartilage Injury In Vitro and In Vivo. *Adv. Mater.* **29**, (2017).

149. B. Marelli, M. Brenckle, D. L. Kaplan, F. G. Omenetto, Silk fibroin as edible coating for perishable food preservation. *Sci. Rep.* **6**, 25263 (2016).
150. K. Schacht, T. Jüngst, M. Schweinlin, A. Ewald, J. Groll, T. Scheibel, Biofabrication of Cell-Loaded 3D Spider Silk Constructs. *Angew. Chem. Int. Ed.* **54**, 2816-2820 (2015).
151. A. Lammel, M. Schwab, M. Hofer, G. Winter, T. Scheibel, Recombinant spider silk particles as drug delivery vehicles. *Biomaterials* **32**, 2233-2240 (2011).
152. S.-W. Hwang, H. Tao, D.-H. Kim, H. Cheng, J.-K. Song, E. Rill, M. A. Brenckle, B. Panilaitis, S. M. Won, Y.-S. Kim, Y. M. Song, K. J. Yu, A. Ameen, R. Li, Y. Su, M. Yang, D. L. Kaplan, M. R. Zakin, M. J. Slepian, Y. Huang, F. G. Omenetto, J. A. Rogers, A physically transient form of silicon electronics. *Science* **337**, 1640-1644 (2012).
153. C. Fredriksson, R. Feinstein, K. Nordling, G. Kratz, J. Johansson, F. Huss, A. Rising, Tissue response to subcutaneously implanted recombinant spider silk: an in vivo study. *Materials* **2**, 1908-1922 (2009).
154. F. Chen, T. Hesselberg, D. Porter, F. Vollrath, The impact behaviour of silk cocoons. *J. Exp. Biol.* **216**, 2648-2657 (2013).
155. C. C. Xu, I. J. Yen, D. Bowman, C. R. Turner, Spider web DNA: a new spin on noninvasive genetics of predator and prey. *PLoS One* **10**, e0142503 (2015).